JOURNAL OF PETROLOGY | VOLUME 52 | NUMBER 1 | PAGES 175–222 | 2011 | doi:10.1093/petrology/egq077

Silicate Liquid Immiscibility within the Crystal Mush: Late-stage Magmatic Microstructures in the Skaergaard Intrusion, East Greenland

M. B. HOLNESS[1]*, G. STRIPP[1], M. C. S. HUMPHREYS[1]†, I. V. VEKSLER[2,3], T. F. D. NIELSEN[4] AND CHRISTIAN TEGNER[5]

[1]DEPARTMENT OF EARTH SCIENCES, UNIVERSITY OF CAMBRIDGE, DOWNING STREET, CAMBRIDGE CB2 3EQ, UK

[2]TECHNICAL UNIVERSITY BERLIN, ACKERSTRASSE 71–76, 13355 BERLIN, GERMANY

[3]GFZ GERMAN RESEARCH CENTRE FOR GEOSCIENCES, TELEGRAFENBERG, 14473 POTSDAM, GERMANY

[4]GEOLOGICAL SURVEY OF DENMARK AND GREENLAND, ØSTER VOLDGADE 10, DK-1350 COPENHAGEN K, DENMARK

[5]DEPARTMENT OF EARTH SCIENCES, UNIVERSITY OF AARHUS, HØEGH-GULDBERGS GADE 2, DK-8000 AARHUS C, DENMARK

RECEIVED DECEMBER 9, 2009; ACCEPTED NOVEMBER 3, 2010

Late-stage microstructures developed during the last stages of solidification of the Skaergaard intrusion comprise a wide array of reactive and non-reactive intergrowths. Reactive microstructures ascribed to open-system behaviour include serrated grain boundaries between pyroxene and plagioclase primocrysts, fish-hook pyroxenes and mafic symplectites. They form by the addition of Fe and Ca and removal of alkalis and silica. Other microstructures include those formed by (internally generated) redox reactions between olivine, Fe–Ti oxides and pyroxene. Non-reactive microstructures include closely spatially associated granophyric intergrowths and previously undescribed ilmenite-rich intergrowths that are interpreted as a consequence of crystallization of separated conjugate immiscible liquids. The open-system reactive microstructures occur predominantly in the cumulates on the chamber floor, appearing in LZb and disappearing (to be replaced by a granophyre–ilmenite-rich intergrowth association) in the Upper Zone. They are not common in the Marginal Border Series. Their distribution mirrors that of efficient expulsion of trapped liquid and can be attributed to the gravitationally driven loss of a Si-rich immiscible component from the interstitial liquid. The loss of the Si-rich component causes the remaining Fe-rich liquid to react with the primocrysts. Bulk-rock major element data are consistent with little or no preferential loss of the Si-rich liquid from the mush, but the resolution of the available data is not sufficient to assess the effect of this relative movement on the liquid line of descent of the bulk magma. The first appearance of the paired conjugate non-reactive intergrowths in MZ (Marginal Border Series) points to the early onset of immiscibility in the bulk liquid.*

KEY WORDS: *immiscibility; Skaergaard; crystal mush*

INTRODUCTION

Solidification of basic magma involves the development of a crystal mush on the margins of the magma chamber. The chemical evolution of liquid enclosed within this mushy layer is dependent on the extent to which it can exchange chemical components with the bulk liquid outside the mush. Although the liquid line of descent of the bulk magma can be inferred from the observed progression of primocryst assemblages, the chemical evolution of the interstitial liquid and its textural and compositional record have been relatively neglected. The compositional path taken by the interstitial liquid will be critically

*Corresponding author. E-mail: marian@esc.cam.ac.uk

†Present address: Department of Earth sciences, University of Oxford, South Parks Road, Oxford, OX1 3AN. E-mail: madeleine.humphreys@earth.ox.ac.uk

dependent on liquid mobility within the mush. Importantly, the possibility that the interstitial liquid may react with the surrounding solids creates a further mechanism for an evolution divergent from that of the bulk liquid. Gravitationally driven relative movement of liquid and solid within the mush could result in reactions between solid and chemically more- or less-differentiated liquid. The redistribution of cumulus grains, such as the sorting and concentrating of dense particles in magmatic currents, may also affect the chemical evolution of the trapped liquid by altering the modal proportion of the phases with which it is in contact. The magnitude of these effects is expected to vary according to the geometry of the crystallizing assemblage: a slowly cooled mush accumulating at the centre of the chamber floor is more likely both to compact and to undergo sedimentary reworking of the modal assemblage compared with an otherwise similar, but more rapidly cooled, mush zone growing on a vertical chamber wall. The rate of cooling will also control the extent to which diffusive processes can operate during the super-solidus history of the mush.

Decoding the record left in fully solidified plutonic rocks is not straightforward, although much progress has been made since the seminal work of Wager *et al.* (1960). In this contribution we attempt a new approach to interpreting the late-stage solidification history of the mafic cumulates of the Skaergaard intrusion, based on detailed documentation of previously neglected microstructures. We suggest that grain boundary microstructures record a history of reaction with late-stage liquids, and that this history varied significantly within the intrusion. We argue that the root cause of these variations is the extent of liquid migration within the mush, and in particular the relative movement of conjugate immiscible liquids.

GEOLOGICAL BACKGROUND

The textural signatures of late-stage magmatic liquids

Perhaps the most easily understood record of the solidification of late-stage magmatic liquids is that provided by interstitial pockets of intergrown quartz and feldspar, or granophyre, which are understood to form by solidification of highly evolved silicic liquids (Wager & Brown, 1968; McBirney & Nakamura, 1974; McBirney, 1975; Larsen & Brooks, 1994). Granophyre pockets occur in intrusive rocks from granites to gabbros, and are commonly bounded by primocryst grains with euhedral growth facets, suggesting chemical equilibrium with the primocrysts: they represent the last liquids crystallized during solidification along a Bowen-type (i.e. silica-enrichment, Bowen, 1928) liquid line of descent.

However, some microstructures associated with late-stage solidification point to the presence of a reactive liquid that is out of chemical equilibrium with the surrounding grains. For example, in oceanic gabbros, replacive grain-boundary microstructures, including embayed orthopyroxene crystals partially replaced by secondary olivine, and clinopyroxene forming grain boundary stringers and cuspate triple-junction grains, have been interpreted as the result of localized reaction between a late intergranular melt and primocrysts (Seyler *et al.*, 2007). Other evidence of late-stage reaction includes symplectites formed between early formed primocrysts (Carstens, 1957; Haselton & Nash, 1975; Ambler & Ashley, 1977; Turner & Stüwe, 1992; Shaw, 1999; de Haas *et al.*, 2002). Perhaps the best known are the orthopyroxene–magnetite oxy-symplectites that grow in gabbros where olivine and Fe–Ti oxides are in contact, replacing the olivine. There is no consensus as to whether they form by sub-solidus oxidation of olivine according to a reaction of the type

$$\text{olivine} + O_2 = \text{enstatite} + \text{magnetite}$$

(Muir *et al.*, 1957; Goode, 1974; Haselton & Nash, 1975; Johnston & Stout, 1984), possibly involving diffusion of other components in addition to oxygen (Barton & van Gaans, 1988); by the exsolution of minor components from olivine (Moseley, 1984; Ashworth & Chambers, 2000); or whether they form via late-stage magmatic processes whereby early olivine primocrysts react with residual liquid (Carstens, 1957; Ambler & Ashley, 1977; Barton *et al.*, 1991).

Turner & Stüwe (1992) described symplectitic intergrowths of orthopyroxene + anorthite (with local, replacive amphibole) between primocrysts of olivine and labradoritic plagioclase in gabbros from Black Hill in South Australia. The olivine grains are locally mantled by orthopyroxene coronas that are proposed to have formed in the presence of melt via a reaction such as olivine + SiO_2 = orthopyroxene. The symplectites are suggested to have formed in the high-temperature sub-solidus as a result of Na loss in compositional gradients set up during cooling (Turner & Stüwe, 1992). Coronas and symplectites on olivine–plagioclase boundaries were also reported by De Haas *et al.* (2002) but the symplectites in this case comprise orthopyroxene + spinel. De Haas *et al.* (2002) proposed an entirely magmatic origin for these symplectites.

Recent work has highlighted a type of symplectite that grows when water-rich fluids invade a hot solid host-rock. These hydrous partial melting reactions typically involve reaction of olivine and clinopyroxene to form orthopyroxene and amphibole, while primocryst plagioclase becomes strongly enriched in anorthite (Koepke *et al.*, 2005*a*, 2005*b*, 2007). A hydrous silica-rich melt, with composition

similar to that of oceanic plagiogranites, is produced from the reaction

$$\text{ol} + \text{cpx} + \text{plag}_1 + \text{H}_2\text{O} = \text{opx} + \text{plag}_2 + \text{amph} + \text{Si-rich melt}.$$

Clinopyroxene may be produced instead of amphibole if water activity is reduced or if temperatures are higher (>940°C) under water-saturated conditions (Koepke *et al.*, 2005*a*, 2005*b*). Koepke *et al.* (2005*a*, 2005*b*, 2007) suggested that small amounts of felsic material (plagiogranite) forming veins and irregular replacement structures in the oceanic crust may have formed by hydrous partial melting processes.

Other disequilibrium grain boundary microstructures include vermicular intergrowths of clinopyroxene and An-rich plagioclase, associated with acicular apatite grains and reversed rims on plagioclase primocrysts. These are known as fish-hook pyroxenes and have been reported from the Kiglapait intrusion (Morse & Nolan, 1984) and oceanic gabbros (Batiza & Vanko, 1985; Koepke *et al.*, 2005*a*, 2005*b*). They have previously been interpreted as crystallization products of an intercumulus liquid strongly enriched in the augite component (Morse & Nolan, 1984).

Finally, a recent study of clinopyroxene–plagioclase grain boundaries in the Bushveld intrusion described the growth of orthopyroxene lamellae to form protrusions, together with the crystallization of anorthitic plagioclase (Roelofse *et al.*, 2009). These were interpreted as the consequence of reaction with an infiltrating, relatively primitive, liquid into almost completely solidified cumulates (Roelofse *et al.*, 2009).

The Skaergaard intrusion

The Skaergaard intrusion, East Greenland (Fig. 1), formed during a major Eocene magmatic episode associated with early continental break-up during the opening of the North Atlantic (Brooks & Nielsen, 1982; Larsen *et al.*, 1989), filling a box-shaped, fault-bounded chamber (8 km × 11 km × 4 km, Nielsen, 2004) at the contact between underlying Precambrian gneisses and a thick overlying sequence of Eocene plateau lavas.

The intrusion is divided into three main units: the Layered Series (LS), which crystallized from the floor, the Upper Border Series (UBS), which crystallized from the roof, and the Marginal Border Series (MBS), which grew inwards from the walls. These units follow roughly parallel trends of differentiation into the centre of the intrusion, converging at the Sandwich Horizon (SH) (Wager & Deer, 1939). The Layered Series is divided into the lowermost and unexposed Hidden Zone (HZ), Lower Zone (LZ), Middle Zone (MZ) and Upper Zone (UZ), based on the disappearance of primocryst olivine (and its replacement by Ca-poor pyroxene) at the base of the Middle Zone, and its reappearance at the base of the Upper Zone. The Lower Zone is itself subdivided: LZa contains primocrysts of olivine and plagioclase; the base of LZb is marked by the arrival of cumulus augite; and the base of LZc marks the arrival of cumulus Fe–Ti oxides. The Upper Zone is divided into UZa, UZb and UZc by the appearance of abundant coarse, euhedral apatite at the base of UZb and by the mosaic form of ferro-hedenbergite inverted from β-ferrobustamite at the base of UZc. Compaction is thought to have played an important role in the evolution of the Layered Series, increasing in importance through the lower exposed parts of the intrusion. A major increase in the extent of compaction coincides with an increase in melt density accompanying the arrival of Fe–Ti oxides as cumulus phases (Tegner *et al.*, 2009).

The MBS is subdivided in an analogous manner to the Layered Series into LZa*, LZb*, LZc*, MZ*, UZa*, UZb* and UZc* (Hoover, 1989). It grew *in situ* on the steeply dipping or vertical walls with relatively large amounts of trapped liquid (Hoover, 1989). The UBS is divided into zones α, β and γ on the basis of plagioclase compositions (Douglas, 1961), corresponding respectively to the LZ, MZ and UZ. The UBS is richer in silica and incompatible trace elements than the Layered Series (Naslund, 1984; McBirney, 1996*a*).

The compositions of the primocryst minerals change systematically with stratigraphic height in the intrusion. Core compositions of plagioclase feldspar in the Layered Series evolve from An_{68} at the base of the intrusion to An_{25} at the Sandwich Horizon (Maaløe, 1978; McBirney, 1996*a*), whereas olivine evolves from Fo_{74} (in the MBS; Hoover, 1989) to pure fayalite in the Sandwich Horizon. Both Ca-poor and Ca-rich pyroxenes become more Fe-rich with increasing differentiation: from Mg-number 52·7 and Mg-number 68·8 [Mg-number defined as $Mg/(Mg + Fe_{tot})$] respectively to almost pure hedenbergite near the Sandwich Horizon (McBirney, 1996*a*). Ca-poor pyroxene disappears in UZa.

The Skaergaard liquid line of descent

The liquid line of descent of the bulk Skaergaard magma has been contentious for some time. One school of thought, relying on modelling of the chemical evolution of the Layered Series, has the liquid moving towards pronounced iron enrichment at a more or less constant silica content—the Fenner Trend (Fenner, 1929) (Wager & Brown, 1968; Brooks & Nielsen, 1978; Tegner, 1997; McBirney & Naslund, 1990; Morse, 1990; Jang *et al.*, 2001), whereas another, based on bulk liquid experimental constraints and analogies, advocates the Bowen trend towards silica-rich compositions, driven by the crystallization of Fe–Ti oxides (Hunter & Sparks, 1987, 1990; Toplis & Carroll, 1995). A third approach is based on mass balance of the intrusion (Nielsen, 2004) and average compositions. The resulting

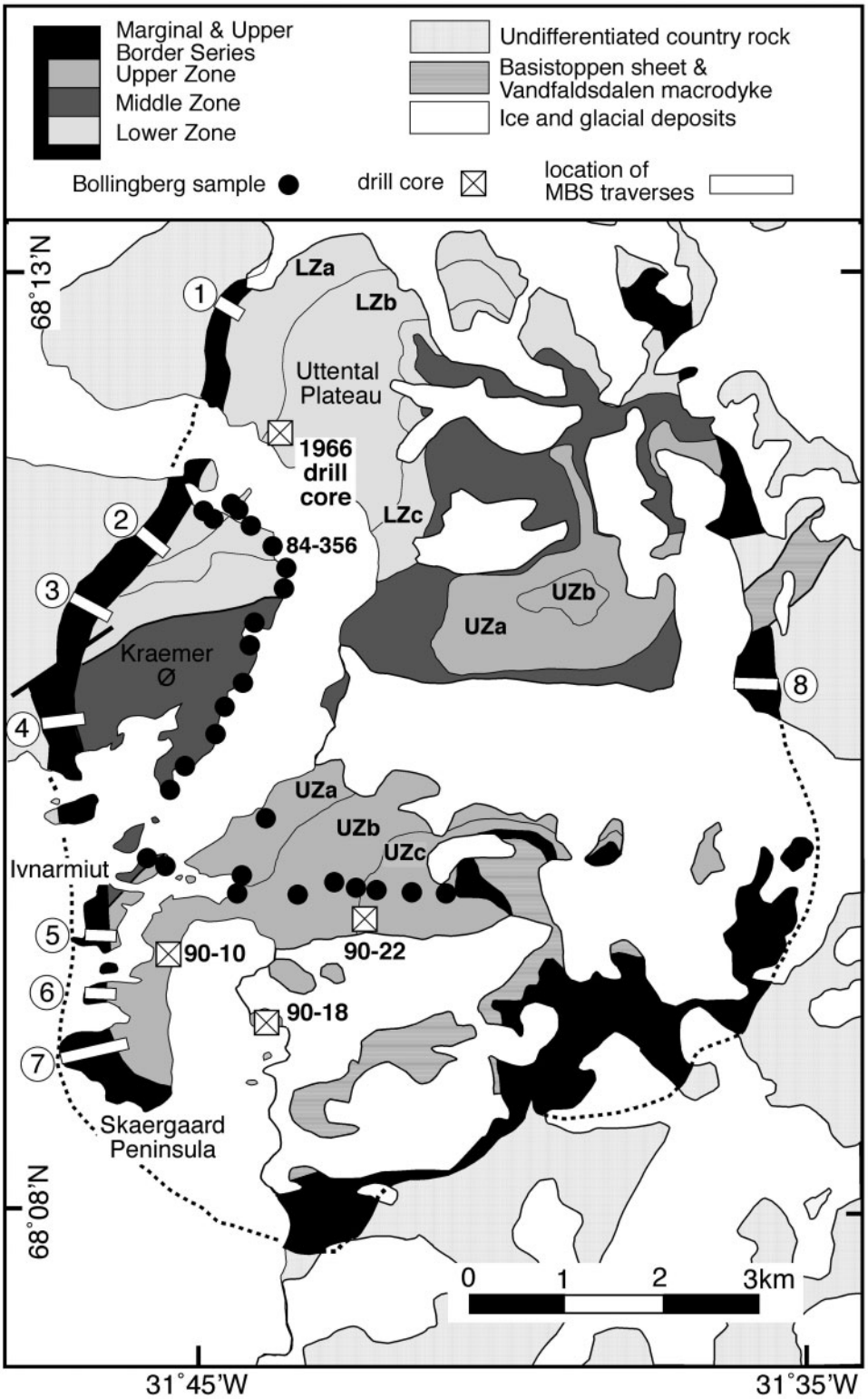

Fig. 1. Simplified geological map of the Skaergaard intrusion, after McBirney (1996*b*). The positions of the samples studied are shown. The numbered Bollingberg (1995) sample refers to that illustrated in Fig. 5b. The eight traverses across the Marginal Border Series are each numbered.

effective liquid line of descent is transitional between the Fenner and Bowen trends and, as expected, results in a residual granophyric melt (Nielsen *et al.*, 2009).

The common occurrence of large-scale, outcrop-sized pods and lenses of melanogranophyre in the lower part of the UBS and the upper part of the Layered Series (McBirney & Nakamura, 1974) has long been cited as evidence for separation of a late-stage Si-rich immiscible liquid from the Fe-rich magma of the UZ (McBirney & Nakamura, 1974; McBirney, 1975; Naslund, 1984; McBirney, 1989, 2002, 2008; Stewart & DePaolo, 1990). The discovery of coexisting silicic and Fe-rich melt inclusions in primocryst apatite from UZ gabbros (Jakobsen *et al.*, 2005) proves that these grains crystallized in an emulsion. Melting experiments on the UZ cumulates also demonstrate liquid immiscibility (McBirney & Nakamura, 1974; McBirney, 1975). However, there is still considerable debate surrounding the timing of the onset of silicate liquid immiscibility in the bulk magma and the effect it had on the liquid line of descent. Controversial recent experiments by Veksler *et al.* (2007, 2008), as well as studies of plagioclase-hosted melt inclusions (Jakobsen *et al.*, 2006), have placed the onset of liquid immiscibility in the bulk magma much earlier, during the MZ or at the transition between the LZ and MZ [although see comments by McBirney (2008), Morse (2008*b*) and Philpotts (2008)].

Recent experimental and modelling studies (Toplis & Carroll, 1995, 1996; Thy *et al.*, 2009) have demonstrated the critical effect of oxygen fugacity (fO_2) on the liquid evolution trend. The bulk liquid for the intrusion probably evolved under conditions closed to oxygen (Toplis & Carroll, 1996), which means that the abundance and modal proportions of ilmenite and magnetite are strongly dependent on the melt fO_2; the crystallization of Fe–Ti oxides in turn determines the chemical evolution of the magma (Toplis & Carroll, 1995, 1996). On the basis of Fe–Ti oxide modes in bulk rocks from Skaergaard, Thy *et al.* (2009) argued that although Fe–Ti oxide saturation led initially to a decrease in fO_2, the fractionation of Fe–Ti oxides did not lead to significant reduction of oxygen fugacity in the bulk magma, which remained within one log unit of the fayalite–magnetite–quartz (FMQ) oxygen buffer. However, modal proportions cannot be used to discriminate conclusively between cumulus and post-cumulus growth of Fe–Ti oxides, because of subsolidus modification of the oxide compositions and proportions. A further complication is provided by textural evidence suggesting that much of the early magnetite in LZc–MZ may be intercumulus in origin (Bollingberg, 1995).

Chemical evolution of the interstitial liquid

There is little published work on the chemical evolution of the late-stage liquid in the Skaergaard gabbros, although the TiO_2 content of plagioclase overgrowths has been shown to reflect the changing composition of the late interstitial liquids (Humphreys, 2009). Olivine rims separating cumulus grains of oxide and pyroxene have been reported from LZc and MZ and ascribed to reaction with late-stage liquids (Wager & Brown, 1968). A plausible reaction is the reverse of that resulting in oxy-symplectites (i.e. enstatite + magnetite = olivine + O_2), triggered by a decrease in fO_2 in the late-stage liquid. The localized development of 'feathery intergrowths of orthopyroxene and spinel' on oxide–plagioclase grain boundaries in LZc and MZ has also been cited as a record of a reactive late-stage liquid (Wager & Brown, 1968), although these are actually formed of olivine (or pyroxene) and plagioclase (see below). Wager & Brown (1968) offered no suggestions as to the nature of this reaction.

Published studies of liquid immiscibility in the Skaergaard chamber concentrate on the chemical evolution of the bulk magma (McBirney & Nakamura, 1974; McBirney, 1975; Jakobsen *et al.*, 2005; Veksler *et al.*, 2007, 2008). However, even in the early history of the intrusion, although the bulk liquid in the chamber will be far from the two-liquid miscibility gap, the interstitial liquid enclosed within the mush on the chamber margins may have already fractionated significantly and split into immiscible conjugate liquids. During the latest stages in the intrusion's history the bulk liquid will already comprise an emulsion of two liquids and therefore even the earliest interstitial liquid will also be unmixed. The amount of liquid remaining in the mush at the moment it intersects the miscibility gap will be extremely small in the earliest-solidified parts of the intrusion and will increase upwards as the liquid composition becomes more evolved at the moment of its entrapment within the mush.

If the interstitial liquid does intersect the miscibility gap and splits into an emulsion, coalescence of single liquid droplets may result in grain-scale melt pockets dominated by either one or the other conjugate. The documented record of liquid immiscibility preserved in the Skaergaard cumulates is primarily that of the Si-rich conjugate liquid (the melanogranophyres): these form at all scales, with the arrival of abundant grain-scale interstitial pockets of granophyre near the top of the Layered Series (McBirney, 1995, 1996*a*). The crystallization of an Fe-rich late-stage liquid in the interstices of the Skaergaard crystal mush has not been documented, despite the expectation that liquid immiscibility in the mush would be recorded by conjugate pairs of late-stage interstitial intergrowths, one Si-rich (the granophyre) and the other Fe-rich.

In this study we present new evidence for the progressive evolution of late-stage interstitial liquids in the Skaergaard intrusion, including the separation and

crystallization of paired conjugate immiscible interstitial liquids. We show that the two liquids develop different distributions in the mushy zone on the walls and floor of the chamber, with variable extents of gravitationally driven separation within the mush. We suggest that the onset of immiscibility in the bulk liquid is signalled by the appearance in MZ* of large quantities of paired conjugate intergrowths.

SAMPLES AND METHODS

Samples studied

Four sample sets from the Layered Series of the Skaergaard intrusion were examined as part of this study (locations shown in Fig. 1). The 349 m long Cambridge 1966 drill core, housed at the University of Cambridge, includes the only available material from HZ. The 1052·47 m long drill core 90-22 comes from the north side of Basisgletcher and traverses the upper MZ to UZb. Drill core 90-10 is a 535·35 m long drill core collared on the western side of the intrusion on the Skaergaard Peninsula and covers a similar stratigraphic range to 90-22. The Bollingberg profile (Bollingberg, 1995) is a suite of 29 surface rocks comprising samples from LZa up to the Sandwich Horizon). Core 90-22 and 90-10 were collected by Platinova Resources Ltd. in 1990, and are, together with the Bollingberg profiles, housed at GEUS, Copenhagen. The MBS is sampled by eight traverses, each of which continue into the adjacent Layered Series. Samples from UBS were collected by Wager and Deer in 1936.

Analytical techniques

Mineral compositions were determined using a Cameca SX-100 electron microprobe at the Department of Earth Sciences, University of Cambridge, using the PAP data reduction method (Pouchou & Pichoir, 1985). Operating conditions were 15 kV accelerating voltage, 10 nA beam current and 1 μm beam diameter for major elements; with a 100 nA beam current for minor and trace elements. Peak counting times were 30 s for major and 20 s for minor elements.

High spatial resolution (<100 nm) element maps were produced using a JEOL JXA-8500F thermal field emission electron microprobe (FE-EMP) at the German Research Centre for Geosciences (GFZ), Potsdam, Germany. The element distributions were obtained in wavelength-dispersive mode with an acceleration voltage of 8 kV, a beam current of 90 A, and a beam scanning mode and dwell time of 800 ms per pixel (256 × 256 pixels). High-precision analysis of sub-micron scale symplectitic intergrowths was also carried out on the FE-EMP. FE-EMP allows a sub-micron scale electron beam at a low accelerating voltage (5–10 kV) and moderate beam current (100 nA) for high-resolution spot analysis. PRZ corrections (modified ZAF) were applied for the analyses. Run conditions for analysis of clino- and orthopyroxene were 8 kV and 10 nA at the smallest possible beam size (~1000 nm). Peak counting times were 50 s for Fe, 40 s for Ca, Cr and K, 30 s for Si, Ti, Mg and Al, and 10 s for Na.

LATE-STAGE MICROSTRUCTURES IN THE SKAERGAARD INTRUSION

Late-stage microstructures can be divided into two broad groups: those that appear to be in chemical equilibrium with the surrounding mineral grains ('non-reactive microstructures'), defined as those associated with primocryst grains with planar growth faces; and those that do not ('reactive microstructures'), defined as those with an obvious replacive texture relative to adjacent primocrysts.

Reactive microstructures

Stepped grain boundaries

The term 'stepped grain boundary' refers to the serrated texture locally present at clinopyroxene–plagioclase grain boundaries (Stripp *et al.*, 2006; Holness *et al.*, 2007*b*; Fig. 2). The inward 'step' is aligned with the ends of coarse Ca-poor pyroxene exsolution lamellae, which may taper towards the margin of the host grain (Fig. 2a). Finer exsolution lamellae are present within the outer parts of the augite (Fig. 2a–c). The widths and depths of the 'steps' vary between 2 and 10 μm on a single crystal. Rounded inclusions of prehnite or amphibole may occur at the end of exsolution lamellae, which may otherwise be marked by a pore (Fig. 2b, c and h). The plagioclase within the steps is An-rich. Small grains of apatite (Fig. 2d and h), ilmenite and magnetite are common on stepped grain boundaries. The Fe–Ti oxide crystals are anhedral to euhedral and can be abundant, forming groups of >50 grains over a few millimetres of grain boundary. Biotite may be present near the oxide grains.

A similar feature is also observed on the boundaries of orthopyroxene grains in contact with plagioclase (Fig. 2f–h). Here the ends of the exsolved Ca-rich lamellae have grown while the Ca-poor host has been resorbed [this is the opposite of the growth of Ca-poor lamellae within Ca-rich hosts as reported by Roelofse *et al.* (2009)].

Stepped boundaries are most prominent on the margins of Ca-rich pyroxenes containing wide and abundant Ca-poor exsolution lamellae. In HZ and LZ, augite has fine (100) and coarse (001) exsolution lamellae of Ca-poor pyroxene. Augite evolves to ferroaugite by UZa, with fine (20–700 nm) (001) exsolution lamellae of ferropigeonite. By the upper parts of UZb, exsolution lamellae are very thin and barely detectable (Brown, 1957; Bown & Gay,

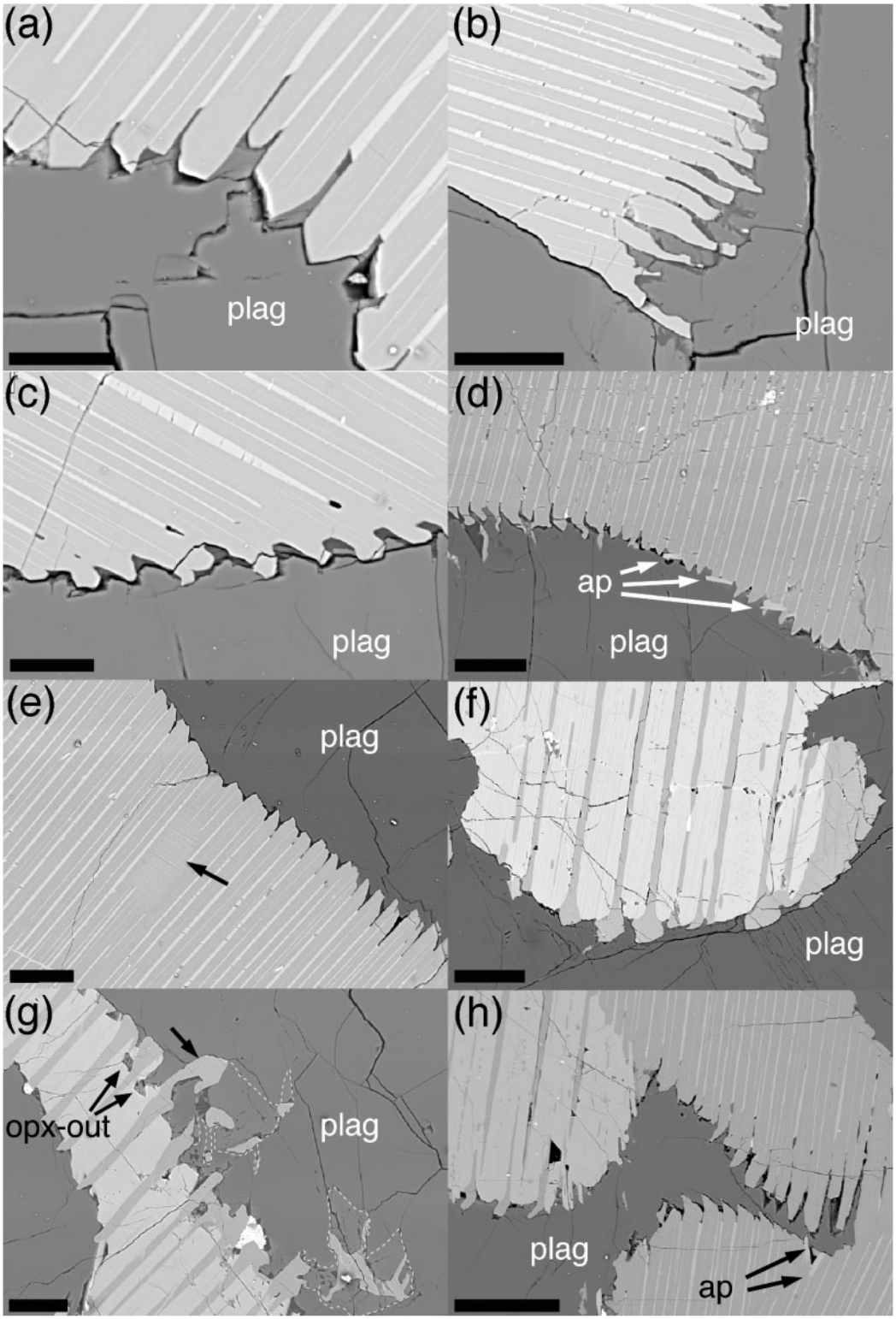

Fig. 2. Back-scattered electron (BSE) images of stepped grain boundaries between pyroxene and plagioclase grains. Abbreviations: plag, plagioclase; opx, orthopyroxene; ap, apatite. All samples are from drill core 90-22. (a) Deep indentations develop on augite–plagioclase grain boundaries at the ends of the coarser Ca-poor exsolution lamellae (palest grey). These lamellae are parallel to the (001) plane of the augite, indicating that they formed before the pigeonite–hypersthene transition. It should be noted that the protruding augite contains finer exsolution

1960; Copley *et al.*, 1974; Copley & Champness, 1975; Champness & Copley, 1976).

Poorly developed, shallow, stepped grain boundaries first appear on clinopyroxene–plagioclase grain boundaries in the Layered Series in the upper parts of LZa (Fig. 3a) and are fully developed in samples above the LZa–LZb boundary. They are seldom ubiquitous on a thin-section scale, but generally become more pronounced and affect more boundaries with stratigraphic height. They are best and most widely developed in MZ, where the steps become elongate and irregular, and are commonly associated with fish-hook pyroxenes (Fig. 2g; see below). The stepped grain boundaries then become shallower and more closely spaced in UZa than in MZ, and the stratigraphic position of their final disappearance depends on position within the intrusion. In the centre of the intrusion (drill core 90-22), they disappear just above the UZa–UZb boundary (Fig. 3a), but nearer the margin of the intrusion (drill core 90-10), this disappearance occurs some 120 m below the MZ–UZ boundary and 30 m below the mineralization in the Triple Group (Fig. 3a).

The UBS contains no stepped grain boundaries. Stepped boundaries occur throughout the MBS although they tend to be less abundant and less well developed than in the Layered Series. All sample traverses from the MBS show the same pattern: stepped grain boundaries appear within HZ* or lower LZa*; their abundance reaches a plateau in the central part of the MBS and then decreases towards the junction of the MBS and the Layered Series (Fig. 3a). This distribution is independent of the modal composition of the MBS; that is, the stepped grain boundaries die out towards the contact with the LS regardless of the stratigraphic zone in which this occurs. Stepped grain boundaries are also locally abundant immediately adjacent to the contact with the country rock.

Fish-hook pyroxenes

Fish-hook pyroxenes comprise irregular filaments of orthopyroxene and/or augite, intergrown with An-rich plagioclase, and acicular apatite needles (Fig. 4). They are found on plagioclase–plagioclase grain boundaries, commonly extending from the corners and edges of stepped pyroxene crystals, with which the pyroxene vermicules are in optical continuity (Fig. 4b–e). They form string-like elongate groups (Fig. 4b) or large clusters that appear to be transitional to replacive symplectites (Fig. 4f, see next section).

The stratigraphic distribution of fish-hook pyroxenes is similar to that of stepped grain boundaries (Fig. 3b), although fish-hook pyroxenes tend to arrive slightly higher in the stratigraphy and disappear at lower levels than the stepped grain boundaries. Fish-hook pyroxenes are relatively uncommon in the MBS and are always formed of orthopyroxene rather than clinopyroxene. No fish-hook pyroxenes were observed in the UBS.

Replacive symplectites

These are the 'feathery intergrowths' of Wager & Brown (1968) and are fine-grained lamellar intergrowths of An-rich plagioclase with olivine ± orthopyroxene ± clinopyroxene (Figs 5 and 6). Lamella width varies from 2 to 50 μm, both within a single symplectitic colony and on the intrusion scale: they are coarsest in the middle of the intrusion and finest where they disappear near the contact.

The symplectitic intergrowth is commonly separated from the phase it is growing away from (or is 'rooted' to) by a thin mono-mineralic rim or substrate, which varies in width from 5 to 30 μm. The mineral forming this symplectite substrate is generally that which is volumetrically dominant in the adjacent symplectite. The most abundant type of replacive symplectite (Type 1) is rooted to oxide and replaces plagioclase (Fig. 5): these symplectites comprise ~50–80 vol. % anorthitic plagioclase intergrown with olivine or, less commonly, orthopyroxene. The mafic phase may change to clinopyroxene at the outer edges of the symplectitic intergrowth (Fig. 5a and e). The irregular shapes of the Fe–Ti oxide roots, especially when compared with the euhedral grains in symplectite-free gabbros, are

lamellae, which indicate that the stepping process occurred before the cessation of pigeonite exsolution. These later lamellae thin towards the boundary, consistent with lower Ca content of the host augite. Scale bar is 20 μm long. Sample from 980·06 m depth in core (MZ). (b) Deep indentations, some of which are irregular in shape or closed off, indicating that the stepping reaction involved growth of augite in addition to dissolution of Ca-poor pyroxene. Scale bar is 30 μm long. Sample from 1026·01 m depth in core (MZ). (c) The coarse Ca-poor exsolution lamellae do not reach the augite–plagioclase grain boundary, and several have pores at their ends. This is due to growth of augite and incomplete overgrowth of the indentations. Scale bar is 20 μm long. Sample from 1026·01 m depth in core (MZ). (d) Apatite (mid-grey euhedral grains) is locally present on stepped grain boundaries. Scale bar is 50 μm long. Sample from 906·16 m depth in core (UZa). (e) A second generation of exsolution lamellae (arrowed) is parallel to the host augite (100) plane. These are formed of hypersthene and again demonstrate that the stepping reaction occurs above the pigeonite–hypersthene transition. Scale bar is 40 μm long. Sample from 906·16 m depth in core (UZa). (f) Host Ca-poor pyroxene (inverted pigeonite) contains exsolution lamellae of augite. The exsolution lamellae protrude into the adjacent plagioclase, indicating growth of augite. Scale bar is 50 μm long. Sample from 1031·11 m depth in core (MZ). (g) Protruding augite exsolution lamellae, with evidence for dissolution of the host inverted pigeonite. The irregular shapes of the augite growths should be noted: these are a poorly developed fish-hook pyroxene (see later text). The arrow points to exsolution lamellae of Ca-poor pyroxene within the out-grown augite, demonstrating that stepping occurred before the pigeonite–hypersthene transition. Areas of An-rich plagioclase are outlined with a dashed white line. Scale bar is 40 μm long. Sample from 1000·08 m depth in core (MZ). (h) Image showing the two types of stepped boundary, each involving growth of augite and dissolution of Ca-poor pyroxene. The porosity developing within the augite at the ends of the Ca-poor lamellae should be noted. Scale bar is 100 μm long. Sample from 1026·01 m depth in core (MZ).

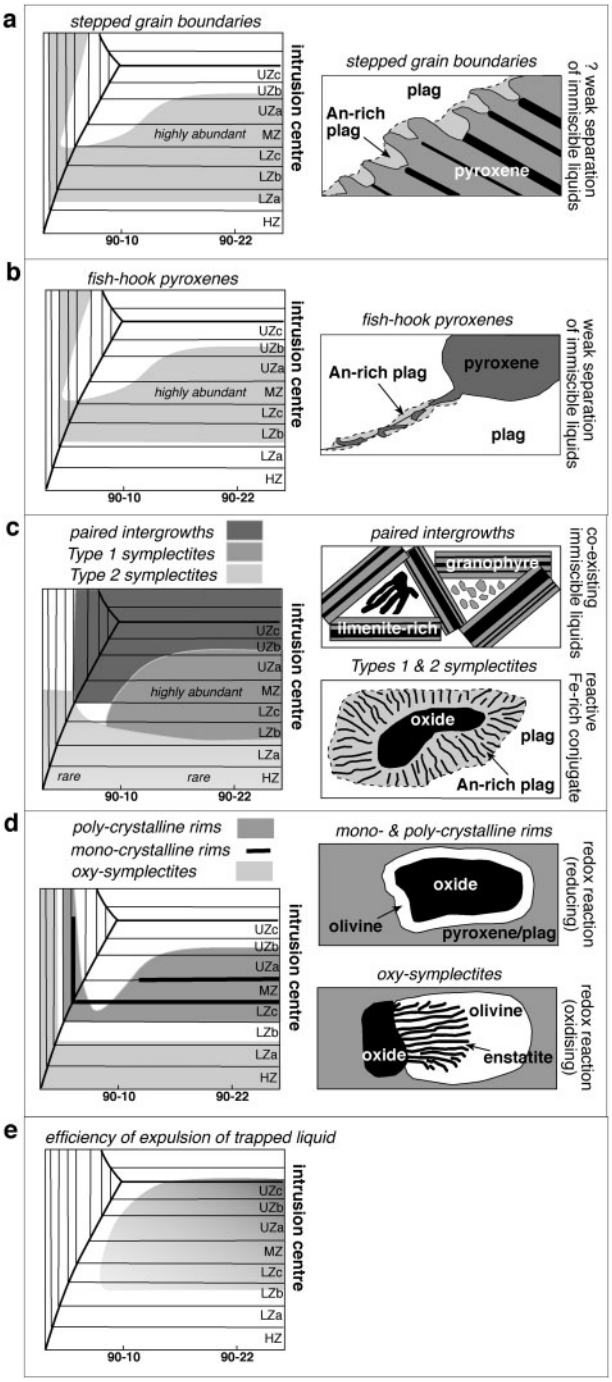

Fig. 3. Schematic depictions of the spatial distribution of the late-stage microstructures discussed in the text, together with sketches of the microstructure in question and a short description of their likely formation mechanisms. In (e) we schematically show a decrease in compaction efficiency towards the intrusion margins, based on Tegner *et al.* (2009), who showed that the amount of trapped liquid decreases at the LZb–LZc boundary in the centre of the intrusion.

suggestive either of partial replacement of the oxide, or of the oxides themselves being interstitial (Fig. 5b and f). Type 2 symplectites comprise orthopyroxene and anorthitic plagioclase and are rooted to olivine (Fig. 6). They commonly have a rim of either amphibole or orthopyroxene.

In the central part of the Layered Series, Type 1 symplectites first appear in LZb, with a significant increase in abundance at the LZb–LZc boundary (Fig. 3c). They remain common throughout LZc and MZ and are most abundant within the Triple Group, reaching 5·5 vol. %. They disappear at the UZa–UZb boundary. Nearer the margins of the intrusion (sampled by drill core 90-10) they disappear ~100 m below the top of MZ. At the margin of the Layered Series with the MBS, Type 1 symplectites are generally rare (being almost absent near the edge of the Layered Series), and are fine-grained. Type 2 symplectites are rare within the LS, but are present in small numbers in the lowest parts (HZ to LZb).

Replacive symplectites are rare in the MBS and are exclusively Type 2 (Fig. 3c). They are most common in the least differentiated parts of the MBS from the lower parts of the intrusion (i.e. Uttental Plateau and Kraemer Island). They are locally abundant directly adjacent to the contact, but generally occur in small numbers, associated with fish-hook Ca-poor pyroxenes. Replacive symplectites are absent in UBS.

Oxy-symplectites

Olivine primocrysts in the lower reaches of the Layered Series and in the outermost MBS are commonly surrounded by orthopyroxene (Figs 6a and 7). Their corroded margins are indicative of a reaction such as olivine + SiO_2 = enstatite. Where olivine grains are in contact with interstitial oxide grains they are partially replaced by oxy-symplectites (Fig. 7, intergrowths of magnetite and enstatite). Oxy-symplectites are present from the lowest levels of the stratigraphy but disappear within the lower parts of LZb and LZb* (Fig. 3d). The orthopyroxene rims and oxy-symplectites are significantly more abundant in the structurally lower parts of the intrusion. No oxy-symplectites were observed in the UBS samples.

Olivine rims

Mono-crystalline (Fig. 8a) and poly-crystalline olivine rims (Figs 8b and 9), 50–200 μm wide, occur around primocrysts from LZc to UZa in the Layered Series. Mono-crystalline olivine rims always occur near primocrysts of olivine with which they are in optical continuity (Fig. 8a), and have variable thickness along their length. They commonly surround Fe–Ti oxide grains, regardless of the adjacent phases, and may extend down oxide–plagioclase, oxide–clinopyroxene, plagioclase–plagioclase and plagioclase–pyroxene grain boundaries. They occur predominantly in upper LZc and lower UZa, and are absent from MZ (Fig. 3d).

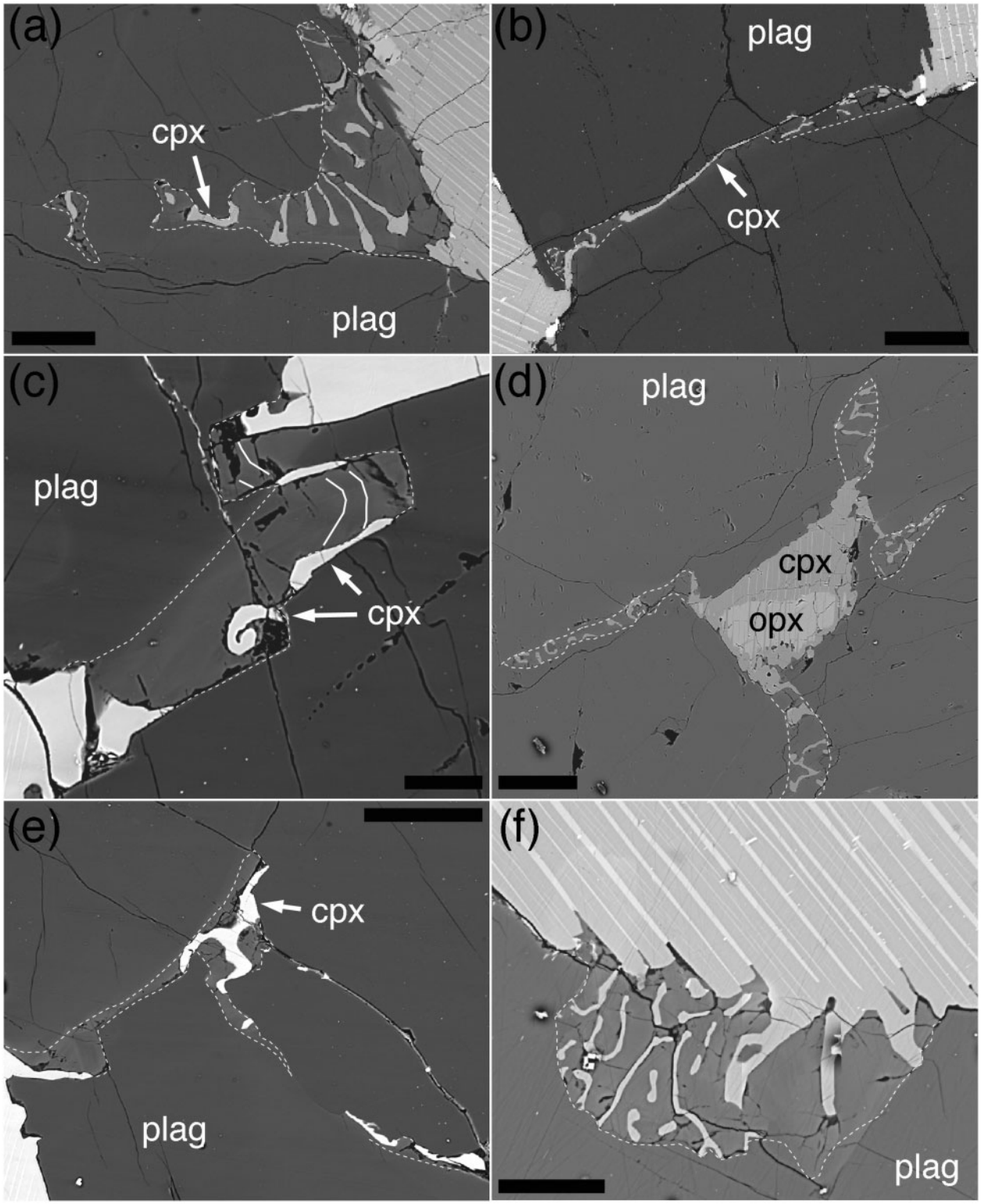

Fig. 4. BSE images of fish-hook pyroxenes in MZ from the 90-22 drill core. Abbreviations: plag, plagioclase; cpx, Ca-rich clinopyroxene; opx, orthopyroxene. Areas of An-rich plagioclase are outlined by a white dashed line. (a) Fish-hook Ca-rich pyroxenes intergrown with An-rich plagioclase extending from a stepped (augite) grain boundary. Scale bar is 100 μm long. Sample from 1017·11 m depth in core. (b) Elongate film of augite and An-rich plagioclase on a plagioclase–plagioclase grain boundary. Scale bar is 100 μm long. Sample from 1035·05 m depth in core. (c) New An-rich plagioclase has compositional zoning (indicated by the continuous white lines) indicating progressive growth. Scale bar is 20 μm long. Sample from 1035·05 m depth in core. (d) Fish-hook pyroxene colonies extending down the four plagioclase–plagioclase grain boundaries adjacent to a pyroxene grain (formed of intergrown Ca-rich and Ca-poor pyroxene). Scale bar is 50 μm long. Sample from 1001·05 m depth in core. (e) Fish-hook pyroxene isolated at a three-grain plagioclase junction. Scale bar is 40 μm long. Sample from 1035·05 m depth in core. (f) Fish-hook pyroxene colonies transitional to replacive symplectites. Scale bar is 30 μm long. Sample from 1017·11 m depth in core.

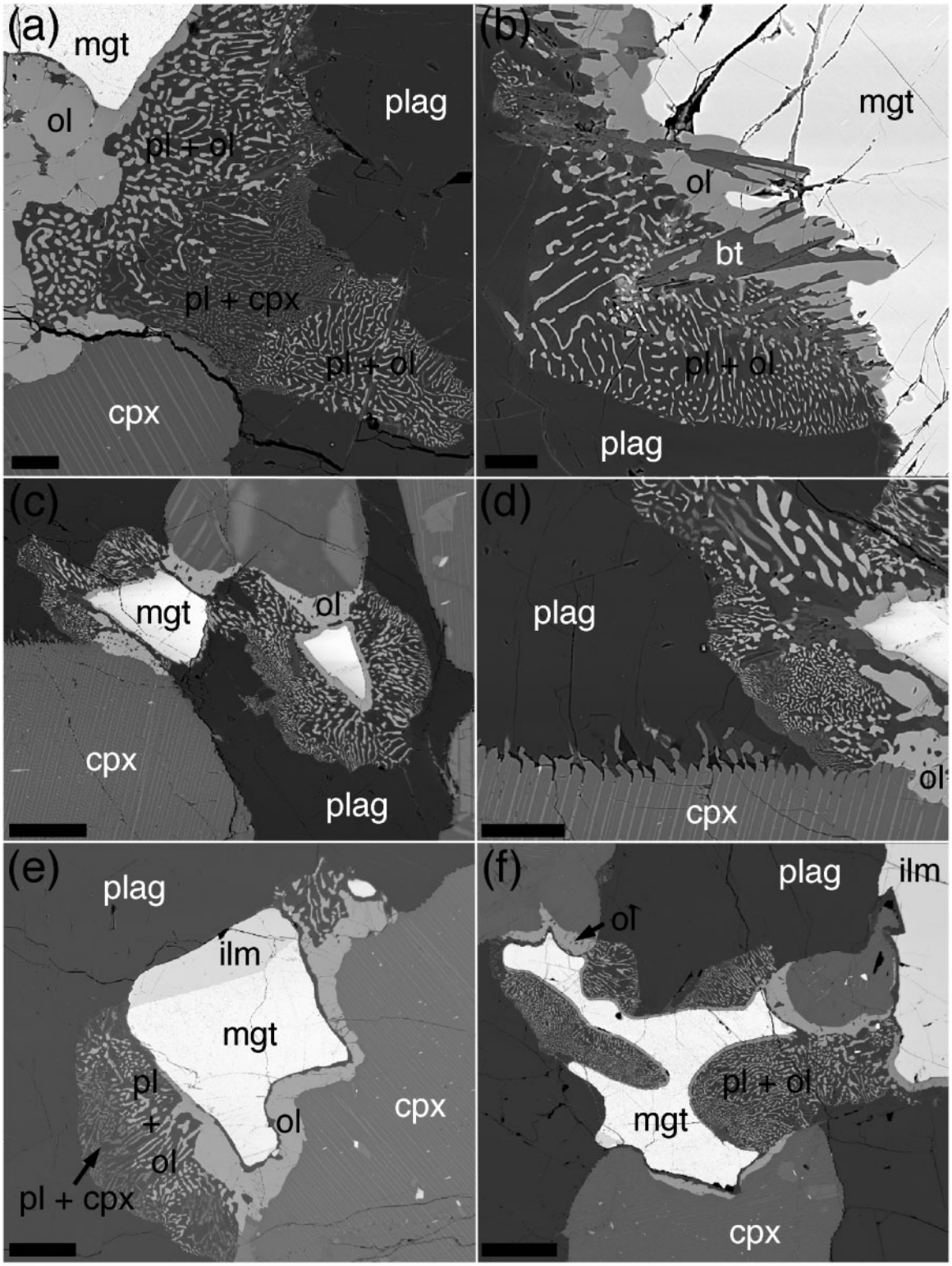

Fig. 5. BSE images of Type 1 replacive symplectites, all [apart from (b)] from drill core 90-22. Abbreviations: plag, plagioclase; cpx, Ca-rich clinopyroxene; ol, olivine; ilm, ilmenite; mgt, magnetite; bt, biotite. (a) Replacive symplectite made of An-rich plagioclase (dark grey) intergrown with olivine (light grey) and augite (mid-grey). The symplectite is rooted to oxide (top-left), with an olivine substrate, and is replacing earlier plagioclase. Scale bar is 50 μm long. Sample from 906·11 m depth in core (UZa). (b) Plagioclase–olivine symplectite with an

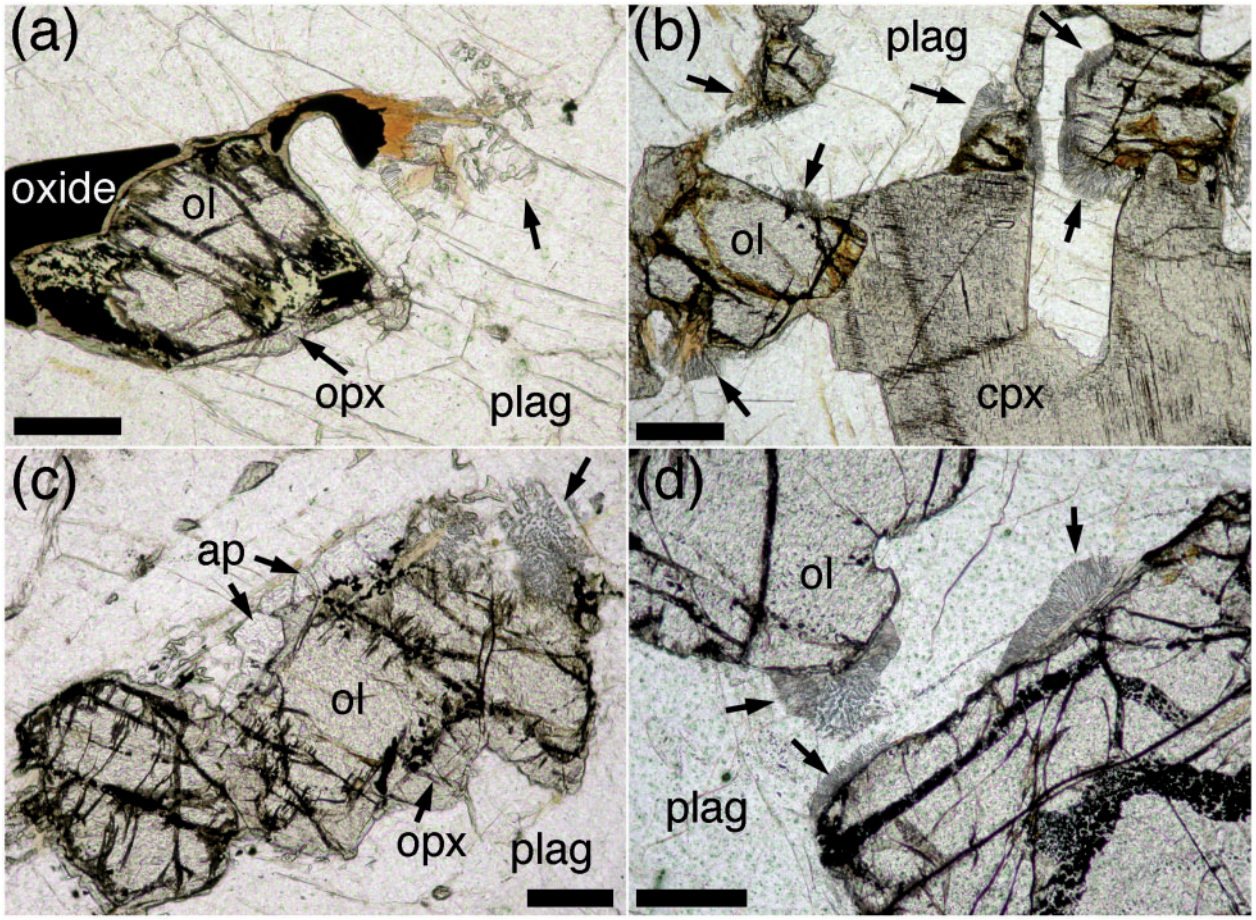

Fig. 6. Optical photomicrographs (plane-polarized light) of Type 2 symplectites (examples are arrowed in each image) from the Marginal Border Series. Abbreviations as in earlier figures. (a) Olivine primocryst with thin rim of orthopyroxene, adjacent to oxide grain. The symplectite colony rooted to the oxide grain comprises plagioclase and Ca-poor pyroxene. Scale bar is 500 μm long. Sample from Traverse 3 in Fig. 1. (b) Primocrysts of olivine and plagioclase, with interstitial augite. Symplectitic colonies are rooted to the olivine grains where in contact with primocryst plagioclase. Scale bar is 100 μm long. Sample from Traverse 1 in Fig. 1. (c) Olivine partially replaced by a symplectitic colony. Scale bar is 500 μm long. Sample from Traverse 3 in Fig. 1. (d) Olivine primocrysts with Type 2 symplectites growing from them, primarily replacing adjacent primocryst plagioclase. Scale bar is 500 μm long. Sample from Traverse 3 in Fig. 1.

Parallel-sided rims of texturally equilibrated poly-crystalline olivine occur between Fe–Ti oxides and pyroxene (Fig. 8b). Where in contact with clinopyroxene they are associated with An-rich plagioclase that may form either small, rounded inclusions within the rim, or a thin skin separating the olivine rim from the oxide (Fig. 9a–e). Small (up to 30 μm diameter), rounded Fe–Ti oxides are locally present in both mono- and poly-crystalline olivine rims (e.g. Fig. 9c and e). Rims are non-ubiquitous on a thin-section scale, with some oxide grains having a rim on one side but not the other. Rim growth locally occurs at the expense of Ca-poor pyroxene, preferentially replacing

olivine–biotite substrate, rooted to an oxide grain. Scale bar is 40 μm long. Sample 84-356 (LZb) from the Bollingberg profile (see Fig. 1 for location). (c) The close spatial association of replacive symplectites with poly-crystalline olivine rims should be noted (see later text). Scale bar is 300 μm long. Sample from 906·16 m depth in core (UZa). (d) Detail of replacive symplectite (with both olivine and clinopyroxene as the mafic phase) adjacent to a stepped augite grain boundary, from (c). The steps are relatively poorly developed where in contact with the symplectite, which grows into the plag-filled steps. The onset of the stepping reaction therefore predated symplectite growth, but continued during symplectite growth. Scale bar is 40 μm long. Sample from 906·16 m depth in core (UZa). (e) Single oxide grain comprising magnetite (bright) and ilmenite (slightly darker). There is no relationship between oxide composition and symplectite development; the grain shapes relate to subsolidus exsolution. The development of a poly-crystalline olivine rim where the oxide is adjacent to the augite primocryst should be noted. Scale bar is 200 μm long. Sample from 1001·05 m depth in core (MZ). (f) Image demonstrating the close spatial relationship of replacive symplectites and poly-crystalline olivine rims. Scale bar is 300 μm long. Sample from 906·16 m depth in core (UZa).

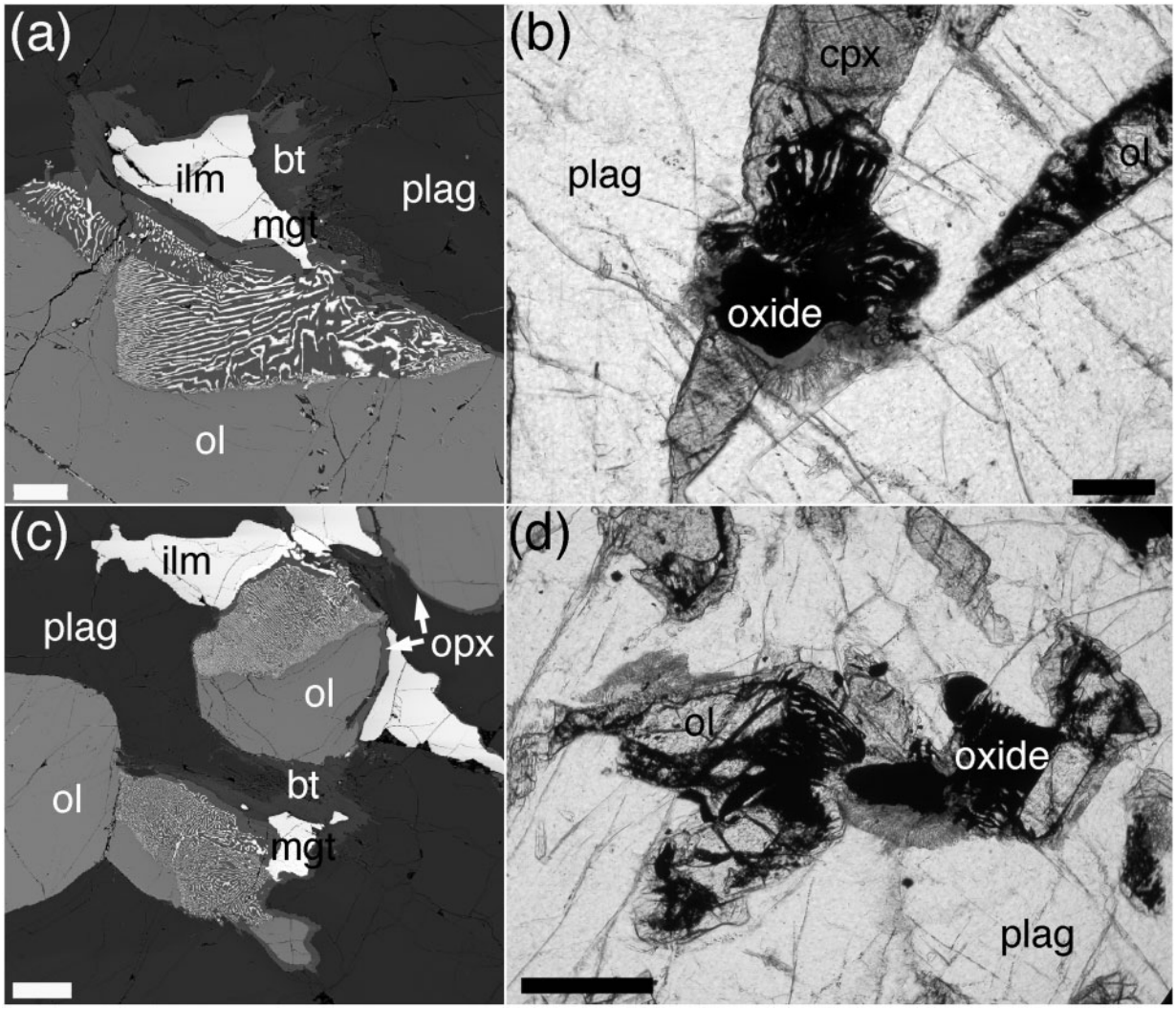

Fig. 7. Abbreviations as in earlier figures. (a) BSE image of an olivine primocryst partially replaced by oxy-symplectite where adjacent to an oxide grain. Scale bar is 100 μm long. Sample 118605, at 35 m depth in the 1966 drill core (LZb). (b) Optical photomicrograph (plane-polarized light) of an olivine primocryst entirely replaced by oxysymplectite. The Type 2 symplectite rooted to the olivine grain, replacing adjacent primocryst plagioclase, should be noted. Scale bar is 100 μm long. Sample from Traverse 2 across the Marginal Border Series (see Fig. 1 for location). (c) BSE image of oxysymplectites. The orthopyroxene rim surrounding the olivine primocryst should be noted. Scale bar is 200 μm long. Sample 118605, at 35 m depth in the 1966 drill core (LZb). (d) Optical photomicrograph (plane-polarized light) of partially replaced olivine primocrysts, with Type 2 symplectites rooted to them. Scale bar is 200 μm long. Sample from Traverse 4 across the Marginal Border Series (see Fig. 1 for location).

the Ca-poor component of pyroxene grains containing exsolution lamellae (Fig. 9e and f).

Poly-crystalline rims appear just below, or at, the arrival of cumulus oxides (i.e. the LZb–LZc or LZb*–LZc* boundary, Fig. 3d). Between the disappearance of the oxy-symplectites and the appearance of the poly-crystalline rims, oxide grains have well-defined boundaries against pyroxene grains, or are partly surrounded by a discontinuous, non-parallel rim of plagioclase. Rarely, in samples in this otherwise rim-free zone, rims locally develop around large (5 mm) isolated oxide grains. In the Layered Series poly-crystalline rims are very common in the MZ and disappear at a similar point to the replacive symplectites. In the MBS, poly-crystalline rims disappear within MZ*.

Non-reactive microstructures

Interstitial granophyre

Interstitial granophyric pockets, 20 μm to 5 mm across, and with sharp, planar-sided boundaries against adjacent primocrysts (usually plagioclase, Fig. 10a, b and d), comprise intergrowths of quartz with plagioclase and/or alkali feldspar. Some granophyric pockets also contain one or

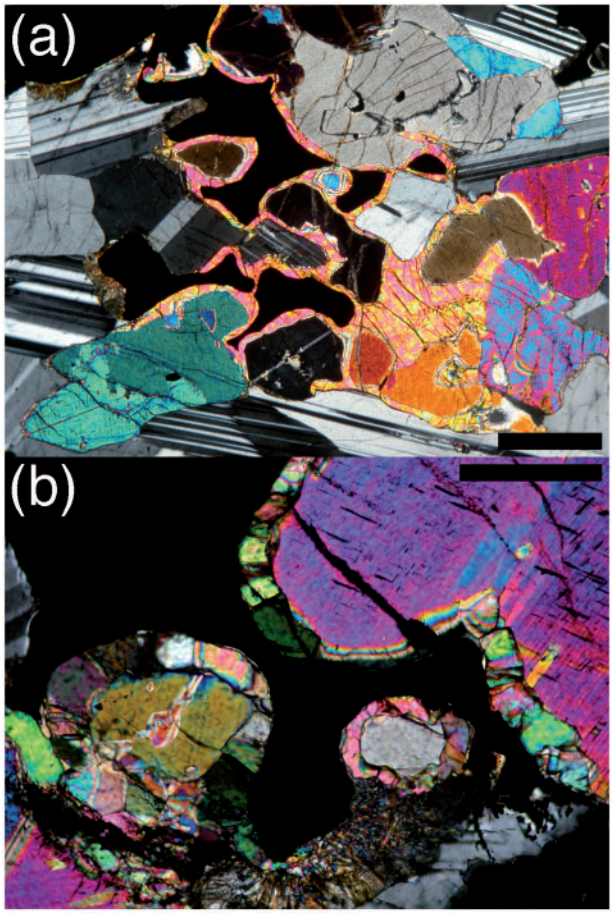

Fig. 8. Optical photomicrographs with crossed polars. (a) Mono-crystalline olivine rims extending from a single olivine primocryst, and growing predominantly along oxide–silicate grain boundaries. Scale bar 300 μm long. Sample from MZ. (b) Poly-crystalline olivine rim separating oxide and augite primocrysts. Scale bar 500 μm long. Sample from 980·06 m depth in drill core 90-22 (MZ).

more of the phases apatite, biotite, amphibole, Fe–Ti oxide and clinopyroxene (Fig. 10c and d).

Interstitial ilmenite-rich intergrowths

These previously undescribed interstitial intergrowths are dominated by large, dendritic ilmenite crystals, intergrown most commonly with granophyre (Fig. 10f), but also with either plagioclase (Fig. 11a) or K-feldspar, biotite (Fig. 11b), orthopyroxene, clinopyroxene (Fig. 11c, d, f and g) or olivine (Fig. 11e). They are commonly spatially associated with compact (primocryst) grains of magnetite (Fig. 12). The size of the intergrowths varies from <50 μm to 5 mm. Generally the ilmenite-rich intergrowths are coarsest and best developed in the more differentiated parts of the MBS and are more fine-grained in the Layered Series. Although the intergrowths may have an irregular outline, adjacent primocrysts typically have euhedral growth faces with no evidence of reaction. Adjacent primocryst phases are commonly mafic (Fig. 11), although some ilmenite-rich intergrowths are partially bounded by plagioclase (e.g. Fig. 10f).

The ilmenite-rich intergrowths are almost universally associated with non-replacive interstitial granophyre, and this coupled association is present in the upper parts of the Layered Series (Fig. 3c). Their first appearance generally coincides with the disappearance of the replacive symplectites, fish-hook pyroxenes and poly-crystalline olivine rims; however, in drill core 90-22 they coexist with replacive symplectites over ~100 m of stratigraphy. The transition from replacive to non-replacive symplectites cuts the concave-upwards stratigraphy of the Layered Series, occurring near the UZa–UZb boundary in the centre of the intrusion, but in the middle of MZ at the outer margin of the Layered Series. This transition to rocks bearing abundant granophyre, and its convex-upwards shape, was noted by McBirney (1996a). The complementarity between the replacive symplectites and the coupled non-replacive association is demonstrated in the meso-scale by thin granophyre veins in the Triple Group that have ilmenite-rich symplectites at their margins (Fig. 10e), whereas replacive symplectites are present several millimetres away.

In the MBS, the paired association is first seen in MZ*, and marks the disappearance of the poly-crystalline olivine rims. Non-replacive symplectites are present in UBSα, the least differentiated unit of UBS.

Evolved interstitial pockets

Samples from the lower parts of the stratigraphy (HZ to LZb) contain rare, small, isolated, planar-sided poly-crystalline pockets containing a combination of quartz, albite, K-feldspar, pyroxenes, apatite, rutile, zircon and Fe–Ti oxides. The pockets are typically very fine-grained and often preferentially weathered. Their bulk composition varies widely according to the assemblage present. They occur in slightly greater abundance in the outermost parts of the MBS on the Skaergaard Peninsula. The significance of these pockets is discussed by Humphreys (2011).

MINERAL CHEMISTRY

The compositions of the most common microstructures were analysed in samples throughout drill core 90-22 (MZ to UZb) and from the Lower Zone in the Bollingberg sequence, along with cumulus minerals from the same zones for comparison, where possible.

Plagioclase

The full dataset of plagioclase compositions can be found in Supplementary Dataset 1 (available at http://www

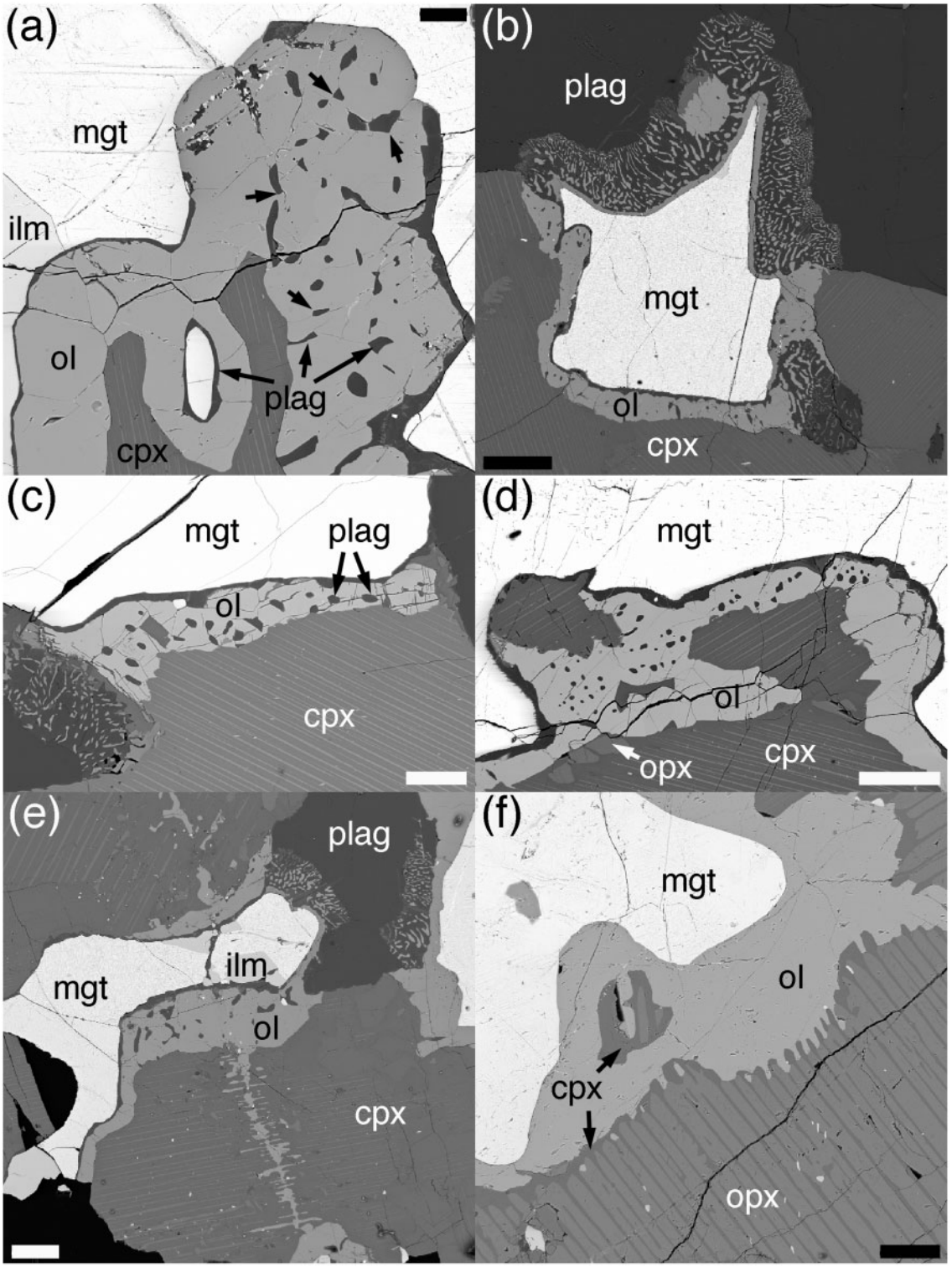

Fig. 9. BSE images of olivine rims. All samples from drill core 90-22; abbreviations as in earlier figures. (a) Poly-crystalline rim separating oxide and augite primocrysts. The texturally equilibrated grains of plagioclase on the three-grain junctions in the olivine should be noted (examples of high olivine–olivine–plagioclase dihedral angles are arrowed). A thin substrate of plagioclase separates the olivine and the oxide. Scale bar is 50 μm long. Sample from 1023·09 m depth in core (MZ). (b) A plagioclase-bearing poly-crystalline rim encircles an oxide primocryst where adjacent to augite. Replacive plag–augite symplectites are rooted to the oxide grain where it is adjacent to primocrystic plagioclase. Scale bar is 200 μm long. Sample from 906·16 m depth in core (UZa). (c) Small oxide grain within a plagioclase-bearing poly-crystalline rim. Scale bar is 50 μm long. Sample from 1000·08 m depth in core (MZ). (d) The oxide grain is adjacent to augite along its length although the poly-crystalline rim only locally contains plagioclase. Scale bar is 100 μm long. Sample from 1000·08 m depth in core (MZ). (e) Growth of olivine within the adjacent augite grain, presumably along a fracture. It should be noted how the replacement of the pyroxene is best developed along the Ca-poor exsolution lamellae. Scale bar is 100 μm long. Sample from 1005·07 m depth in core (MZ). (f) Preferential replacement by a mono-crystalline olivine rim of the Ca-poor pyroxene host (mid-grey), leaving behind the Ca-rich pyroxene exsolution lamellae (dark grey). Scale bar is 100 μm long. Sample from 909·05 m depth in core (UZa).

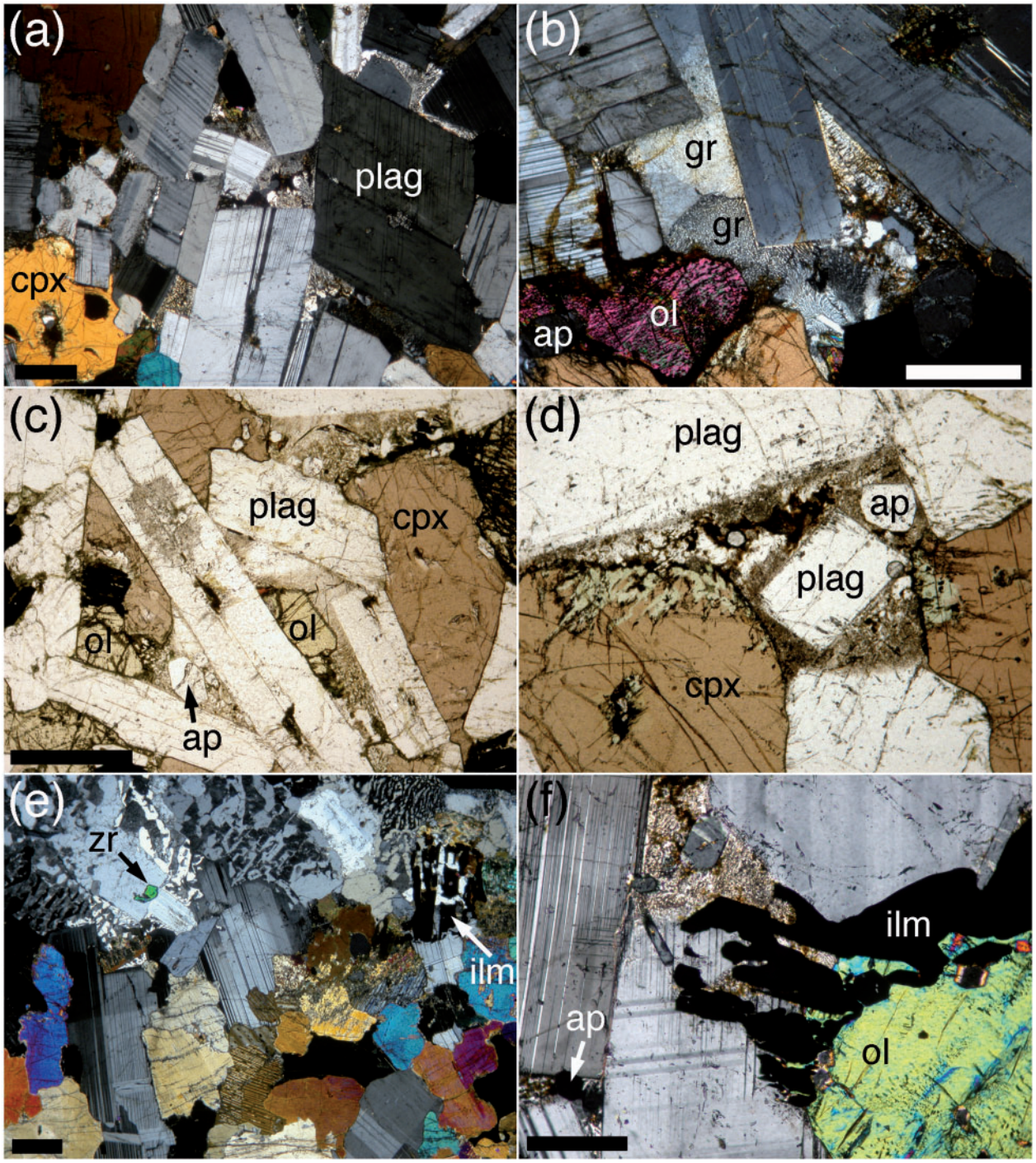

Fig. 10. Optical photomicrographs of non-replacive microstructures. All samples from drill core 90-22: abbreviations as in earlier figures (ap, apatite; zr, zircon; gr, granophyre). (a) Granophyric intergrowths filling planar-sided pockets between plagioclase primocrysts. Crossed polars. Scale bar is 500 μm long. Sample from 87·7 m depth in core (UZb). (b) The well-developed crystal faces on the bounding plagioclase grains should be noted. Crossed polars. Scale bar is 500 μm long. (c) Interstitial pocket between planar-sided plagioclase grains filled with a combination of interstitial augite, euhedral interstitial apatite, granophyre and a patch of ilmenite-rich intergrowth. Plane-polarized light. Scale bar is 500 μm long. Sample from 107 m depth in core (UZb). (d) Granophyre-filled pocket, also containing oxides and biotite. The compositional change of the augite adjacent to the pocket should be noted; this is perhaps due to alteration by fluids released from the silicic liquid as it solidified. Plane-polarized light. Scale bar is 300 μm long. Sample from 67·7 m depth in core (UZb). (e) The top of the image shows the edge of a granophyre-filled vein, with an ilmenite-rich intergrowth on the vein wall; away from the vein non-reactive microstructures are absent. Crossed polars. Scale bar is 400 μm long. Sample from 995·09 m depth in core (MZ). (f) Interstitial pocket filled at the plagioclase-bounded end by granophyre, and at the olivine-bounded end by an ilmenite-rich intergrowth. Crossed polars. Scale bar is 400 μm long. Sample from 87·7 m depth in core (UZb).

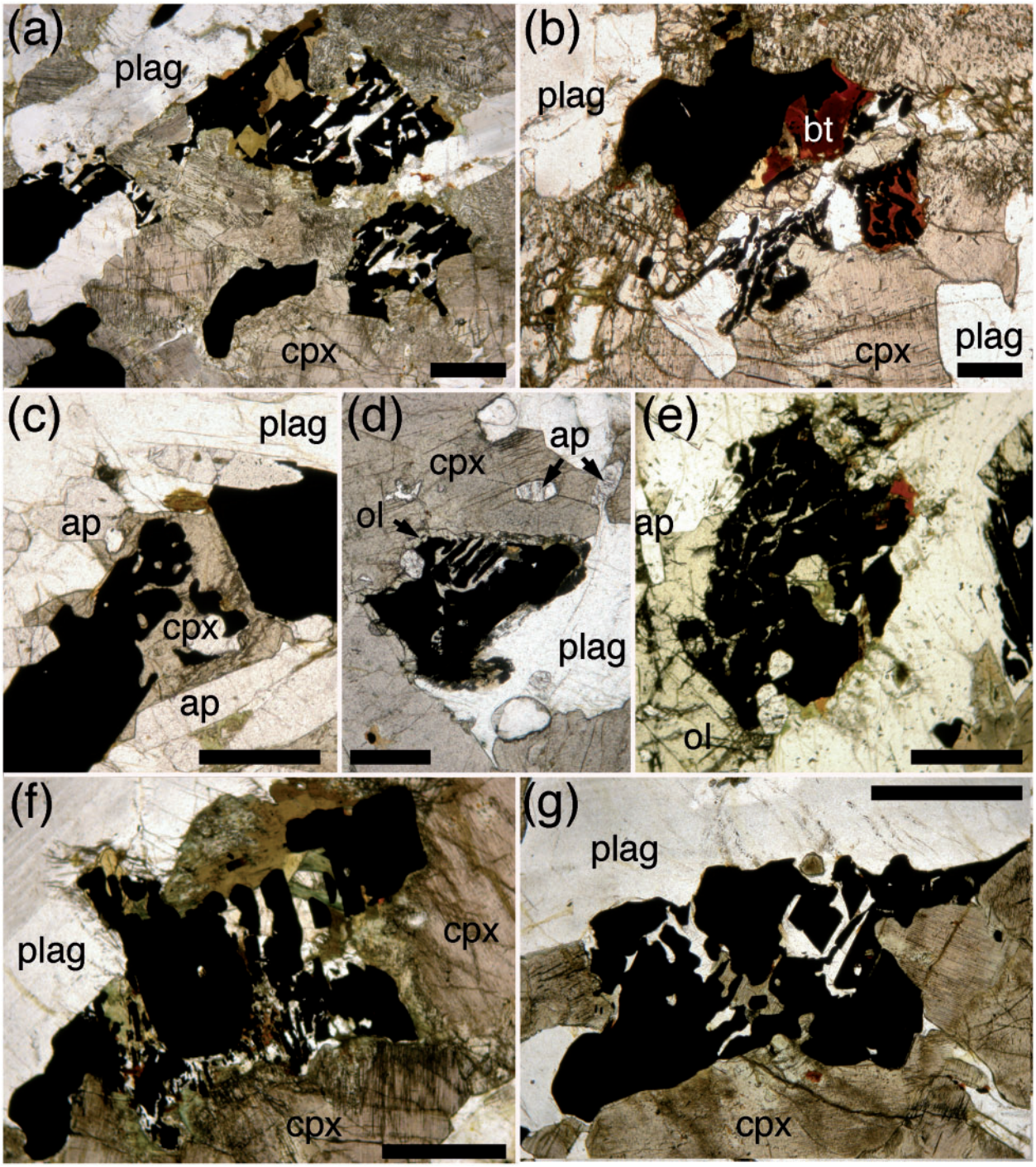

Fig. 11. Optical photomicrographs (plane-polarized light) of ilmenite-rich intergrowths. All samples from drill core 90-22: abbreviations as in earlier figures. (a) Ilmenite intergrown with plagioclase and amphibole. Scale bar is 400 μm long. Sample from 993·28 m depth in core (MZ). (b) Ilmenite intergrown with biotite. Scale bar is 500 μm long. Sample from 1015 m depth in core (MZ). (c) Ilmenite intergrown with augite. Scale bar is 500 μm long. (d) Ilmenite intergrown with augite and partially surrounded by an olivine rim. Scale bar is 500 μm long. Sample from 474·96 m depth in core (UZb). (e) Ilmenite intergrown with fayalitic olivine. Scale bar is 500 μm long. Sample from 310 m depth in core (UZb). (f, g) It should be noted how the ilmenite-rich intergrowths are predominantly associated with the mafic primocrysts. Scale bar is 500 μm long. Sample from 990·50 m depth in core (MZ).

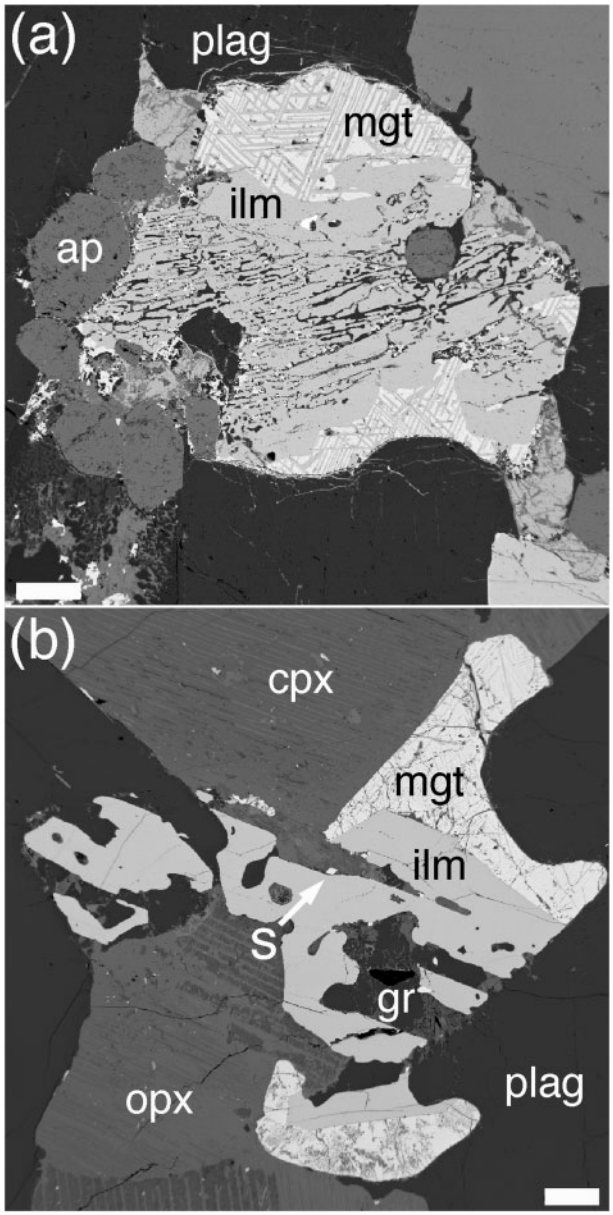

Fig. 12. BSE images of ilmenite-rich intergrowths adjacent to magnetite grains. Both samples from drill core 90-22: abbreviations as in earlier figures (gr, granophyre; s, sulphide). The prominent exsolution lamellae of ilmenite in the magnetite should be noted, as should the granophyre intergrown with the ilmenite in (b). The scale bars in both images are 200 μm long.

.petrology.oxfordjournals.org), with selected analyses presented in Table 1. The plagioclase of the replacive symplectites is distinct from that of associated primocrysts, with sharp compositional boundaries between the two. The symplectite plagioclase is typically more anorthitic ($An_{49–93}$), richer in Fe (0·2–1·8 wt % FeO) and poorer in TiO_2 (Fig. 13). The Mg and Ti contents of the high-Fe plagioclase are not elevated, so we do not consider these analyses to be affected by contamination or secondary fluorescence. The composition of plagioclase lamellae changes smoothly along their growth direction, becoming less An-rich and less Fe-rich (Fig. 14). An abrupt decrease in anorthite content may occur, corresponding to a change in the intergrown mafic mineral from olivine to clinopyroxene (e.g. Fig. 14e). Reversed rims (up to 3% An), 2–20 μm thick, on plagioclase primocrysts are common in samples containing replacive symplectites. Plagioclase in Types 1 and 2 symplectites are similar, with moderate bulk X_{An} and FeO contents. Plagioclase associated with poly-crystalline olivine rims is significantly more Fe-rich than that of the replacive symplectites.

The average composition of symplectite plagioclase varies with stratigraphic position in the intrusion, with the compositional range increasing upwards: a restricted range ($An_{63–66}$) occurs at the LZa–LZb boundary, whereas a range of $An_{55–90}$ occurs in LZc. The concentrations and variability of FeO in symplectitic plagioclase also increase upwards, from ~0·4 wt % at the LZa–LZb boundary to ~0·2–1·2 wt % in MZ. This is in contrast with the primocryst plagioclase, which shows decreasing FeO until UZ, after which FeO increases to ~0·5 wt % (e.g. Tegner, 1997; Humphreys, 2009; Tegner & Cawthorn, 2010).

Plagioclase in the stepped grain boundaries and intergrown with fish-hook pyroxene is also substantially more anorthitic than coexisting primocryst plagioclase, with relatively high FeO and low TiO_2 (Fig. 13). Both microstructures may also show prominent internal zoning (Fig. 14).

Feldspar in UZb granophyre is either $Ab_{99–65}$ or $Or_{67–98}$ (e.g. Fig. 13), and the plagioclase has lower FeO_{tot} wt % and TiO_2 wt % than corresponding primocrysts. Primocryst grains have strongly zoned margins adjacent to the granophyre pockets that are consistent with normal fractionation trends (see Humphreys, 2011).

Olivine

The complete set of analyses for olivine is presented in the Supplementary Dataset 2, with selected analyses in Table 2. Because primocryst olivine is, in general, absent in MZ, the composition of olivine in replacive symplectites could only be compared with that of primocrysts in samples from LZc and UZa. At any stratigraphic position, the replacive symplectite substrate has the most Fo-rich olivine, typically 4–5 mol % more Fo-rich than the primocrysts (Fig. 15). As with the plagioclase, replacive symplectite olivine is zoned along the length of the lamellae. Initial compositions are slightly more Fo-rich than nearby primocryst olivine, whereas the final composition at the end of the symplectite is up to 10 mol % more fayalitic (Fig. 16). Replacive symplectite olivine contains lower concentrations of Mn and P than primocrysts.

Table 1: Representative analyses of plagioclase from 1000·08 m depth in core 90-22 (MZ)

Texture:	Stepped grain boundary							
SiO_2	55·01	56·15	56·51	56·33	54·15	56·16	55·41	52·42
TiO_2	0·02	0·06	0·07	0·07	0·03	0·04	0·05	0·02
Al_2O_3	27·65	26·91	26·90	26·96	28·64	27·14	28·46	28·63
FeO	0·26	0·37	0·38	0·36	0·84	0·39	0·41	0·53
MgO	0·02	0·02	0·01	0·02	0·73	0·05	0·01	0·77
CaO	10·26	9·37	9·32	9·33	11·18	9·88	10·80	11·83
Na_2O	5·48	6·17	6·26	6·36	4·89	5·81	5·21	4·10
K_2O	0·30	0·24	0·18	0·21	0·18	0·27	0·24	0·22
Total	99·09	99·34	99·71	99·74	100·64	99·74	100·59	98·53
Si	2·505	2·546	2·552	2·545	2·439	2·536	2·486	2·412
Ti	0·001	0·002	0·002	0·002	0·001	0·001	0·002	0·001
Al	1·484	1·438	1·431	1·436	1·521	1·444	1·505	1·552
Fe	0·010	0·014	0·014	0·014	0·032	0·015	0·015	0·021
Mg	0·002	0·001	0·001	0·001	0·049	0·003	0·001	0·053
Ca	0·500	0·455	0·451	0·452	0·539	0·478	0·519	0·583
Na	0·484	0·542	0·548	0·557	0·427	0·509	0·453	0·366
K	0·017	0·014	0·010	0·012	0·010	0·016	0·014	0·013
Sum	5·003	5·012	5·009	5·019	5·018	5·003	4·994	5·000
X_{An}	50·0	45·0	44·7	44·3	55·2	47·7	52·7	60·6
Texture:	Fish-hook pyroxene							
SiO_2	49·51	50·47	50·02	51·83	49·54	48·94	52·10	51·00
TiO_2	0·01	0·01	0·00	0·01	0·01	0·01	0·01	0·01
Al_2O_3	32·62	31·70	32·12	30·92	32·39	32·99	30·55	31·39
FeO	0·22	0·24	0·18	0·29	0·28	0·32	0·26	0·32
MgO	0·00	0·01	0·01	0·01	0·01	0·01	0·01	0·01
CaO	15·26	14·45	14·86	13·44	15·10	15·52	13·24	14·26
Na_2O	2·75	3·20	3·02	3·83	2·88	2·52	3·89	3·34
K_2O	0·09	0·12	0·07	0·12	0·07	0·07	0·14	0·11
Total	100·57	100·28	100·37	100·52	100·37	100·45	100·30	100·58
Si	2·251	2·296	2·275	2·345	2·257	2·230	2·361	2·313
Ti	0·000	0·000	0·000	0·000	0·000	0·000	0·000	0·000
Al	1·748	1·700	1·722	1·649	1·739	1·771	1·632	1·678
Fe	0·008	0·009	0·007	0·011	0·011	0·012	0·010	0·012
Mg	0·000	0·001	0·001	0·001	0·001	0·001	0·001	0·001
Ca	0·743	0·704	0·724	0·652	0·737	0·757	0·643	0·693
Na	0·243	0·282	0·266	0·336	0·254	0·222	0·342	0·293
K	0·005	0·007	0·004	0·007	0·004	0·004	0·008	0·006
Sum	4·999	4·999	4·999	5·001	5·003	4·998	4·997	4·997
X_{An}	75·0	70·9	72·8	65·5	74·0	77·0	64·8	69·8
Texture:	Symplectite							
SiO_2	50·63	46·57	48·00	49·33	53·37	45·37	50·46	52·76
TiO_2	0·011	0·002	0·008	0·008	0·007	0·005	0·005	0·010
Al_2O_3	30·61	33·53	32·68	31·73	28·57	34·07	30·76	29·44
FeO	0·32	0·51	0·46	0·44	0·34	0·42	0·33	0·35
MgO	0·01	0·02	0·02	0·02	0·02	0·00	0·01	0·02
CaO	13·86	17·03	15·98	15·24	11·82	18·05	14·23	12·51
Na_2O	3·48	1·63	2·25	2·85	4·76	1·13	3·41	4·54
K_2O	0·11	0·03	0·04	0·05	0·12	0·01	0·10	0·16
Total	99·03	99·39	99·51	99·75	99·08	99·17	99·39	99·89
Si	2·328	2·153	2·209	2·261	2·438	2·110	2·314	2·398

(continued)

Table 1: Continued

Texture:	Symplectite							
Ti	0·000	0·000	0·000	0·000	0·000	0·000	0·000	0·000
Al	1·659	1·827	1·773	1·714	1·538	1·867	1·663	1·577
Fe	0·012	0·001	0·001	0·001	0·001	0·000	0·000	0·001
Mg	0·001	0·035	0·031	0·030	0·023	0·029	0·022	0·024
Ca	0·683	0·844	0·788	0·748	0·578	0·899	0·699	0·609
Na	0·310	0·146	0·201	0·253	0·422	0·102	0·303	0·400
K	0·006	0·002	0·002	0·003	0·007	0·001	0·006	0·009
Sum	5·000	5·007	5·006	5·010	5·007	5·008	5·009	5·018
X_{An}	68·3	85·1	79·5	74·5	57·4	89·8	69·4	59·8
Texture:	Granophyre							
SiO_2	59·90	60·08	58·87	61·28	59·65	59·17	59·31	59·19
TiO_2	0·05	0·06	0·05	0·04	0·04	0·06	0·05	0·06
Al_2O_3	24·32	24·06	24·80	23·65	24·68	24·84	24·87	24·72
FeO	0·34	0·42	0·29	0·33	0·38	0·47	0·44	0·40
MgO	0·00	0·01	0·00	0·00	0·01	0·01	0·01	0·01
CaO	6·89	6·45	7·35	5·92	7·30	7·60	7·37	7·16
Na_2O	7·60	8·10	7·31	8·01	7·36	7·28	7·47	7·41
K_2O	0·47	0·46	0·52	0·69	0·56	0·39	0·38	0·51
Total	99·67	99·72	99·28	99·99	100·05	99·90	100·00	99·55
Si	2·689	2·697	2·658	2·735	2·671	2·656	2·659	2·665
Ti	0·002	0·002	0·002	0·001	0·001	0·002	0·002	0·002
Al	1·287	1·273	1·319	1·244	1·303	1·314	1·314	1·311
Fe	0·013	0·016	0·011	0·012	0·014	0·018	0·016	0·015
Mg	0·000	0·000	0·000	0·000	0·000	0·001	0·001	0·001
Ca	0·331	0·310	0·355	0·283	0·350	0·365	0·354	0·345
Na	0·661	0·705	0·640	0·693	0·639	0·634	0·650	0·647
K	0·027	0·026	0·030	0·039	0·032	0·023	0·022	0·029
Sum	5·010	5·030	5·016	5·008	5·012	5·013	5·018	5·015
X_{An}	32·5	29·8	34·7	27·9	34·3	35·8	34·5	33·8
Texture:	Primocryst							
SiO_2	55·66	56·46	56·72	56·26	56·33	55·83		
TiO_2	0·10	0·07	0·09	0·09	0·11	0·10		
Al_2O_3	26·88	26·69	26·58	26·90	26·84	26·64		
FeO	0·30	0·25	0·24	0·23	0·26	0·29		
MgO	0·03	0·02	0·02	0·02	0·02	0·04		
CaO	9·65	9·29	9·33	9·66	9·53	9·66		
Na_2O	5·68	6·03	5·96	5·86	5·98	5·84		
K_2O	0·31	0·34	0·28	0·27	0·26	0·29		
Total	98·60	99·17	99·24	99·28	99·33	98·69		
Si	2·540	2·560	2·567	2·548	2·550	2·546		
Ti	0·003	0·002	0·003	0·003	0·004	0·003		
Al	1·446	1·426	1·418	1·436	1·432	1·432		
Fe	0·012	0·010	0·009	0·009	0·010	0·011		
Mg	0·002	0·002	0·001	0·001	0·002	0·002		
Ca	0·472	0·451	0·452	0·469	0·462	0·472		
Na	0·502	0·530	0·523	0·514	0·525	0·517		
K	0·018	0·020	0·016	0·016	0·015	0·017		
Sum	4·994	5·000	4·990	4·996	5·000	5·001		
X_{An}	47·6	45·1	45·6	46·9	46·1	47·0		

Plagioclase from non-reactive symplectites comes from 210·9 m in drill core 90-22 (UZb).

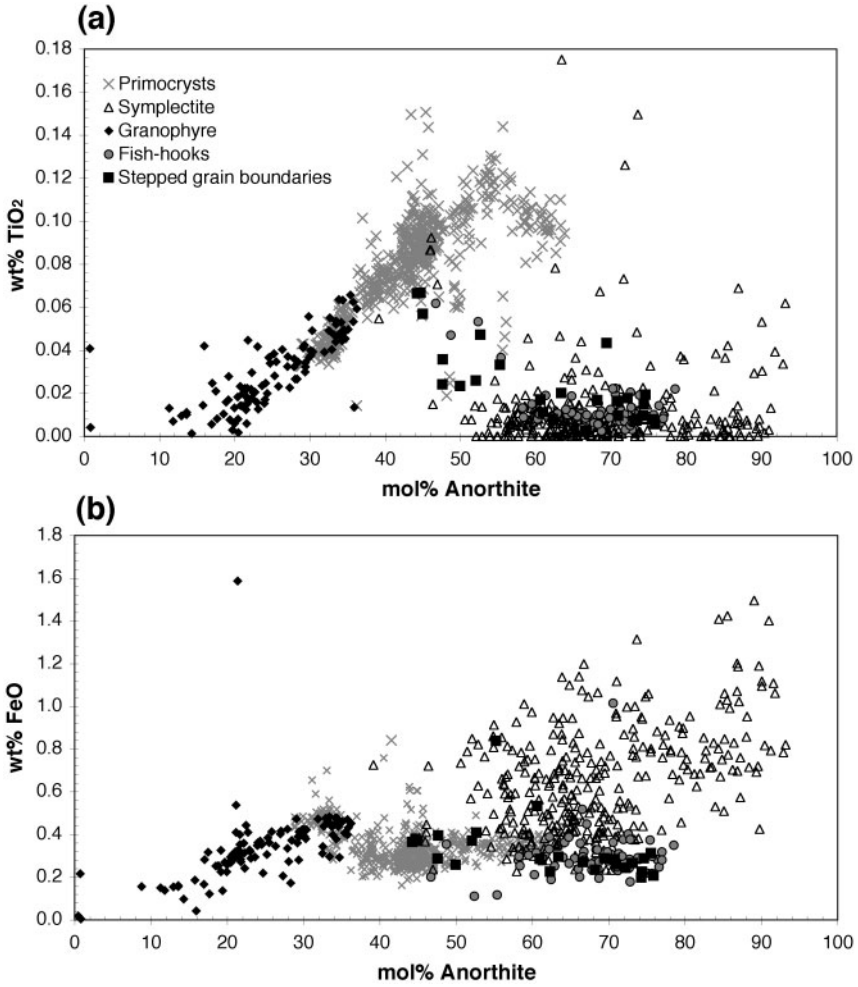

Fig. 13. Variation of Ti content (a) and Fe content (b) in plagioclase as a function of An content. Distinction is made between the different types of plagioclase. Representative analyses can be found in Table 1 (for a full dataset see Supplementary Dataset 1).

Poly- and mono-crystalline olivine and the symplectite substrate have similar compositions that are generally Fo-rich compared with both primocryst and symplectitic olivine (Fig. 15). However, in both LZc and UZa mono-crystalline olivine has a higher P content than poly-crystalline rims, symplectites and the symplectite substrate. Olivine intergrown with non-replacive ilmenite-rich symplectites is typically 2–3 mol % more Fo-rich, with higher TiO_2 concentrations than primocrysts (Fig. 15): this last may be the result of diffusive exchange with the nearby ilmenite.

Clinopyroxene

Clinopyroxene in stepped grain boundaries, fish-hooks and reactive symplectites has lower minor element concentrations (Ti, Al, Mn and Na) and slightly higher CaO contents than primocryst clinopyroxene (Fig. 17 for Ti and Al; see Supplementary Dataset 3 and Table 3 for Mn and Na), although there is no difference in Mg-number. The Ti, Al, Mn and Na contents are highest for stepped grain boundaries, and lowest for symplectitic clinopyroxene (Fig. 17 for Ti and Al; see Supplementary Dataset 3 for Mn and Na).

Orthopyroxene

The complete dataset for orthopyroxene analyses is presented in Supplementary Dataset 4, with selected analyses in Table 4. Orthopyroxene in the Type 2 symplectite substrate has higher Mg-number (54–58 in MZ) than primocryst, fish-hook or symplectitic orthopyroxene, which all have similar compositions (Mg-number 49–56) (Fig. 18). Like symplectitic olivine and plagioclase, symplectitic orthopyroxene composition changes along the length of the symplectite (typically from Mg-number ~59 to 50). Fish-hook and Type 2 symplectite orthopyroxene also have less TiO_2 than primocrysts (Fig. 18). Minor element concentrations are similar to those of the primocrysts.

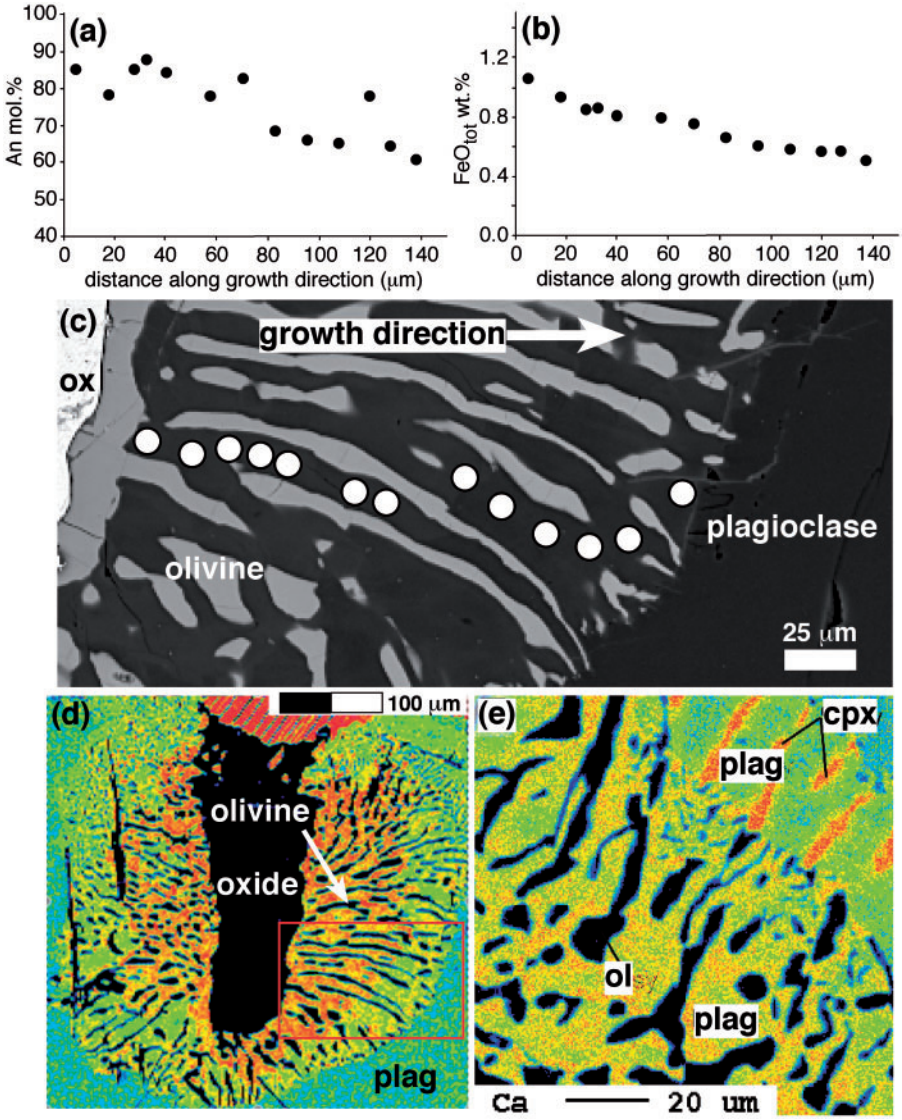

Fig. 14. Compositional variations in symplectites: sample from 1026 m depth in drill core 90-22 (MZ). (a) The variation of anorthite content of plagioclase with distance from the symplectite substrate. (b) The variation of Fe content of plagioclase with distance from the symplectite substrate. (c) Location of the analyses. (d) Smaller-scale element map (Ca) of the same symplectite, with red box outlining the area depicted in (c). The reduction in Ca content of the symplectite plagioclase with growth direction should be noted. (e) Close-up element map (Ca) of a symplectite with an inner olivine–plagioclase zone and an outer augite–plagioclase zone. The step-change in plagioclase composition accompanying the change in mafic phase should be noted.

Apatite

Compared with primocryst apatite from UZb, apatite associated with symplectites is considerably enriched in Cl (~0·4 wt % compared with ~0·05 wt %) (Supplementary Dataset 5, and Table 5). The same relationship was observed between primocryst and grain boundary apatites from Skaergaard (Brown & Peckett, 1977). McBirney & Sonnenthal (1990) found similar compositions in late-stage metasomatic features such as dendritic anorthosites and associated pegmatites.

Fe–Ti oxides

Compositional data for the Fe–Ti oxides are presented in Supplementary Dataset 6, with selected analyses in Table 6. The ilmenite in the ilmenite-rich intergrowths has the same composition as that of the ilmenite primocrysts, except for slightly higher Ca contents. Stepped grain boundary magnetite is FeO-poor, TiO_2-rich, MnO-rich, MgO-poor and Al_2O_3-poor relative to primocrysts. Grain boundary ilmenite is FeO-, Al_2O_3- and MnO-rich and TiO_2- and MgO-poor compared with primocrysts. The

Table 2: Representative analyses of olivine from LZc (sample 359, Bollingberg profile)

	Intergrown with ilmenite							
SiO_2	32·09	31·52	30·53	31·10	30·90	30·58	30·90	31·17
TiO_2	0·40	0·53	0·57	0·10	0·07	0·59	0·46	0·19
Al_2O_3	0·01	0·01	0·01	0·01	0·01	0·00	0·01	0·01
Fe_2O_3	0·00	0·00	0·22	0·18	0·13	0·21	0·00	0·00
FeO	58·98	59·06	59·39	60·81	60·13	59·81	60·29	59·33
MnO	0·85	0·86	0·86	0·85	0·87	0·85	0·84	0·85
MgO	7·91	7·91	7·77	7·24	7·27	7·62	7·60	8·10
CaO	0·03	0·03	0·03	0·05	0·05	0·03	0·04	0·03
Total	100·27	99·93	99·36	100·32	99·42	99·68	100·08	99·69
Si	1·013	1·002	0·983	0·995	0·997	0·983	0·989	0·997
Ti	0·009	0·013	0·014	0·002	0·002	0·014	0·011	0·005
Al	0·000	0·000	0·000	0·000	0·000	0·000	0·000	0·000
Fe^{3+}	0·000	0·000	0·003	0·002	0·002	0·003	0·000	0·000
Fe^{2+}	1·558	1·571	1·600	1·628	1·622	1·608	1·613	1·587
Mn	0·023	0·023	0·023	0·023	0·024	0·023	0·023	0·023
Mg	0·372	0·375	0·373	0·345	0·349	0·365	0·362	0·386
Ca	0·001	0·001	0·001	0·002	0·002	0·001	0·001	0·001
Total	2·977	2·985	2·997	2·998	2·998	2·997	3·000	2·998
Mol % Fo	19·3	19·3	18·9	17·5	17·7	18·5	18·3	19·6
	Mono-crystalline rim							
SiO_2	35·85	36·10	35·64	35·88	36·07	35·94	35·56	36·02
TiO_2	0·00	0·05	0·15	0·21	0·26	0·06	0·07	0·26
Al_2O_3	0·00	0·00	0·00	0·01	0·03	0·00	0·00	0·04
Fe_2O_3	0·00	0·00	0·55	0·27	0·00	0·00	0·38	0·00
FeO	37·63	36·82	35·57	34·96	35·45	37·28	35·81	35·06
MnO	0·38	0·49	0·37	0·37	0·41	0·42	0·47	0·34
MgO	26·15	27·21	27·88	28·53	28·34	26·67	27·48	28·05
CaO	0·07	0·06	0·04	0·03	0·09	0·06	0·06	0·11
Total	100·17	100·74	100·25	100·28	100·75	100·45	99·84	99·92
Si	1·006	1·002	0·992	0·993	0·996	1·003	0·995	1·001
Ti	0·000	0·001	0·003	0·004	0·005	0·001	0·001	0·005
Al	0·000	0·000	0·000	0·000	0·001	0·000	0·000	0·001
Fe^{3+}	0·000	0·000	0·006	0·003	0·000	0·000	0·004	0·000
Fe^{2+}	0·883	0·855	0·828	0·809	0·818	0·870	0·838	0·814
Mn	0·009	0·012	0·009	0·009	0·010	0·010	0·011	0·008
Mg	1·093	1·125	1·155	1·176	1·165	1·109	1·145	1·160
Ca	0·002	0·002	0·001	0·001	0·003	0·002	0·002	0·003
Total	2·994	2·997	2·994	2·996	2·998	2·995	2·996	2·993
Mol % Fo	55·3	56·8	58·1	59·2	58·7	56·0	57·6	58·8

(continued)

Table 2: Continued

	Poly-crystalline rim							
SiO_2	36·06	36·19	36·05	36·03	36·15	35·53	35·73	35·73
TiO_2	0·44	0·29	0·15	0·25	0·47	0·10	0·35	0·29
Al_2O_3	0·01	0·00	0·00	0·02	0·00	0·01	0·00	0·01
Fe_2O_3	0·00	0·00	0·00	0·00	0·00	0·00	0·00	0·00
FeO	34·80	34·72	35·81	35·67	34·14	37·64	37·03	36·57
MnO	0·40	0·33	0·50	0·49	0·30	0·46	0·45	0·36
MgO	28·37	28·74	27·22	27·69	28·96	26·23	26·43	26·56
CaO	0·09	0·11	0·09	0·06	0·03	0·11	0·13	0·18
Total	100·21	100·39	99·85	100·22	100·12	100·13	100·15	99·73
Si	0·998	0·998	1·006	1·001	0·997	0·999	1·001	1·003
Ti	0·009	0·006	0·003	0·005	0·010	0·002	0·007	0·006
Al	0·000	0·000	0·000	0·001	0·000	0·000	0·000	0·000
Fe^{3+}	0·000	0·000	0·000	0·000	0·000	0·000	0·000	0·000
Fe^{2+}	0·805	0·801	0·836	0·828	0·788	0·885	0·867	0·858
Mn	0·009	0·008	0·012	0·012	0·007	0·011	0·011	0·009
Mg	1·169	1·180	1·131	1·145	1·190	1·098	1·102	1·110
Ca	0·003	0·003	0·003	0·002	0·001	0·003	0·004	0·005
Total	2·993	2·996	2·991	2·994	2·993	2·999	2·992	2·991
Mol % Fo	59·2	59·6	57·5	58·0	60·2	55·4	56·0	56·4
	Symplectite substrate							
SiO_2	36·14	35·77	35·43	35·59	35·72	35·66	35·43	35·55
TiO_2	0·58	0·15	0·08	0·13	0·08	0·04	0·02	0·01
Al_2O_3	0·02	0·01	0·00	0·00	0·01	0·02	0·08	0·12
Fe_2O_3	0·00	0·97	1·10	0·68	0·00	0·00	0·00	0·00
FeO	36·57	34·51	35·68	35·27	36·21	38·35	38·45	39·77
MnO	0·39	0·36	0·53	0·49	0·47	0·47	0·49	0·48
MgO	26·52	28·76	27·47	27·87	27·05	25·86	25·44	23·95
CaO	0·11	0·08	0·10	0·06	0·09	0·22	0·34	0·34
Total	100·35	100·64	100·46	100·16	99·68	100·66	100·28	100·25
Si	1·006	0·987	0·987	0·991	1·002	1·000	0·999	1·008
Ti	0·012	0·003	0·002	0·003	0·002	0·001	0·000	0·000
Al	0·001	0·000	0·000	0·000	0·000	0·001	0·003	0·004
Fe^{3+}	0·000	0·010	0·012	0·007	0·000	0·000	0·000	0·000
Fe^{2+}	0·851	0·796	0·832	0·821	0·849	0·899	0·907	0·943
Mn	0·009	0·008	0·013	0·012	0·011	0·011	0·012	0·012
Mg	1·099	1·182	1·140	1·156	1·130	1·080	1·068	1·012
Ca	0·003	0·002	0·003	0·002	0·003	0·007	0·010	0·010
Total	2·982	2·990	2·988	2·992	2·996	2·999	2·999	2·989
Mol % Fo	56·4	59·4	57·5	58·3	57·1	54·6	54·1	51·8

(continued)

Table 2: Continued

	Symplectite							
SiO_2	35·23	35·24	35·33	35·57	35·53	35·37	35·19	35·51
TiO_2	0·02	0·01	0·01	0·02	0·01	0·01	0·00	0·04
Al_2O_3	0·07	0·04	0·08	0·05	0·04	0·09	0·07	0·04
Fe_2O_3	0·25	0·16	0·00	0·17	0·00	0·00	0·00	0·00
FeO	38·72	39·62	40·98	37·75	38·35	39·05	40·99	39·87
MnO	0·45	0·49	0·50	0·45	0·47	0·46	0·47	0·46
MgO	25·17	24·64	22·66	26·23	25·10	24·50	22·97	24·39
CaO	0·29	0·29	0·27	0·21	0·22	0·26	0·25	0·24
Total	100·22	100·50	99·86	100·47	99·74	99·77	99·95	100·55
Si	0·996	0·998	1·013	0·997	1·006	1·005	1·008	1·004
Ti	0·000	0·000	0·000	0·000	0·000	0·000	0·000	0·001
Al	0·002	0·001	0·003	0·002	0·001	0·003	0·002	0·001
Fe^{3+}	0·003	0·002	0·000	0·002	0·000	0·000	0·000	0·000
Fe^{2+}	0·916	0·938	0·982	0·885	0·908	0·928	0·982	0·943
Mn	0·011	0·012	0·012	0·011	0·011	0·011	0·011	0·011
Mg	1·060	1·039	0·967	1·095	1·059	1·037	0·980	1·027
Ca	0·009	0·009	0·008	0·006	0·007	0·008	0·008	0·007
Total	2·997	2·998	2·986	2·998	2·993	2·993	2·991	2·994
Mol % Fo	53·6	52·5	49·6	55·3	53·8	52·8	50·0	52·1
	Primocryst							
SiO_2	35·16	35·01	34·67	34·70	34·67	34·50	35·26	35·52
TiO_2	0·03	0·02	0·05	0·03	0·04	0·03	0·02	0·01
Al_2O_3	0·01	0·01	0·01	0·01	0·01	0·00	0·03	0·00
Fe_2O_3	0·54	0·69	1·52	1·51	1·37	1·76	0·43	0·00
FeO	38·20	37·73	37·93	38·05	37·82	37·60	38·37	38·38
MnO	0·51	0·50	0·52	0·53	0·51	0·54	0·51	0·53
MgO	25·58	25·65	25·26	25·23	25·33	25·25	25·52	25·66
CaO	0·07	0·07	0·13	0·09	0·11	0·12	0·09	0·07
Total	100·09	99·69	100·10	100·16	99·88	99·81	100·24	100·19
Si	0·994	0·993	0·983	0·984	0·984	0·981	0·995	1·001
Ti	0·001	0·000	0·001	0·001	0·001	0·001	0·000	0·000
Al	0·000	0·000	0·000	0·000	0·000	0·000	0·001	0·000
Fe^{3+}	0·006	0·007	0·016	0·016	0·015	0·019	0·005	0·000
Fe^{2+}	0·903	0·894	0·899	0·902	0·898	0·894	0·906	0·905
Mn	0·012	0·012	0·012	0·013	0·012	0·013	0·012	0·013
Mg	1·077	1·083	1·067	1·065	1·071	1·069	1·073	1·077
Ca	0·002	0·002	0·004	0·003	0·003	0·004	0·003	0·002
Total	2·994	2·992	2·983	2·983	2·985	2·981	2·995	2·998
Mol % Fo	54·2	54·6	53·8	53·7	54·0	53·9	54·1	54·4

Olivine from ilmenite-rich intergrowths comes from UZb (310·2 m depth in drill core 90-22).

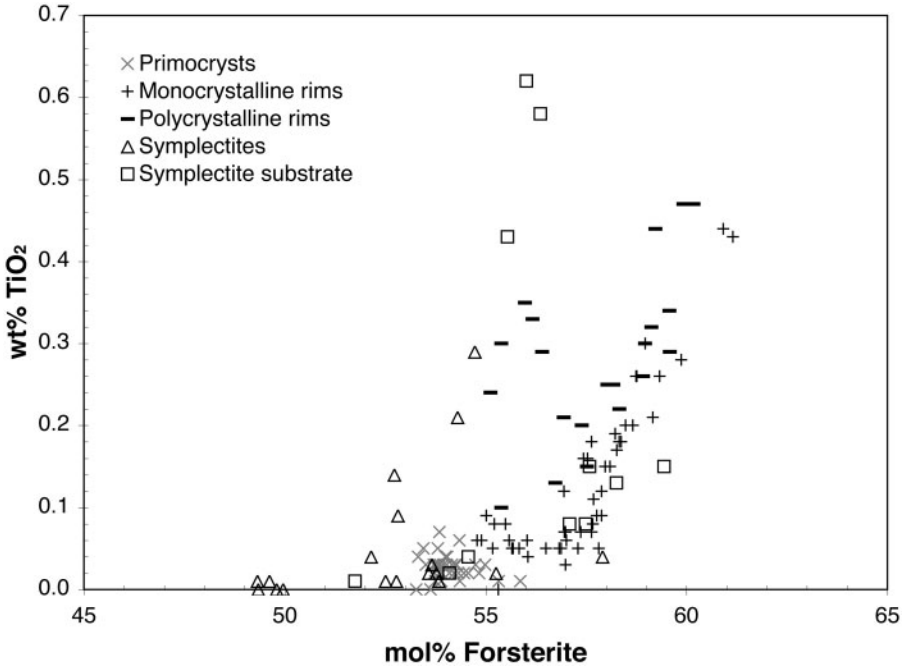

Fig. 15. Compositional variation of olivine in the late-stage microstructures compared with that of the cumulus grains in LZc. Representative analyses can be found in Table 2 (for a full dataset of analyses see the Supplementary Dataset 2).

significance of these differences is unclear because, in common with larger Fe–Ti oxide grains (e.g. Jang *et al.*, 2001), the grain-boundary oxide compositions have probably changed in the subsolidus.

Primary and replacive biotite

In the MBS, HZ, LZa and LZc, interstitial amphibole and F-rich biotite fill planar-sided pockets at inter-phase grain boundaries, and surround pyroxene and Fe–Ti oxide primocrysts. From LZc upwards, primary amphibole and biotite are rare, but replacive biotite is common. Replacive biotite in reactive symplectites was analysed in five samples from the Triple Group (selective analyses are presented in Table 7, with the complete dataset in Supplementary Dataset 7): this is rich in Fe and Al, and poor in Ti, Si and Mg, compared with primary interstitial biotite from LZa. It also contains 1·2–1·3 wt % F, higher than the concentrations in the LZ interstitial biotite (0·3–1·0 wt %).

GEOTHERMOMETRY

The re-equilibration and apparent reaction in the gabbros complicates attempts to constrain the temperature at which the microstructures formed. However, minimum estimates from stepped boundaries and Type 1 replacive symplectites both suggest that they grew while residual melt was still present.

Stepped boundaries

It has been suggested that stepped grain boundaries formed via dissolution of Ca-poor exsolution lamellae that retain a metastable pigeonite structure (Stripp *et al.*, 2006; Holness *et al.*, 2007*b*). If this were correct then they must have formed below the pigeonite–hypersthene transition in these rocks (900–1000°C, Holness *et al.*, 2007*b*). However, there are two lines of evidence to demonstrate that this suggestion is not correct. First, the apparent dissolution of the Ca-poor host containing Ca-rich exsolution lamellae with bulbous outgrowths (Fig. 2f–h) cannot have been a consequence of reaction of metastable pigeonite, as the orthopyroxene host grains have completely inverted from their original monoclinic form. The microstructures on Skaergaard pyroxene–plagioclase grain boundaries must therefore result from a reaction consuming Ca-poor pyroxene and producing Ca-rich pyroxene and anorthite. Second, the presence of exsolution lamellae of Ca-poor pyroxene within the lobate stepped regions, with an orientation indicative of their formation above the pigeonite–hypersthene transition (Fig. 2g) demonstrates that the stepping reaction forming the lobes on Ca-rich pyroxene–plagioclase boundaries must have occurred at a temperature higher than that of the pigeonite–hypersthene transition.

Type 1 replacive symplectites

Temperature constraints were placed on the Type 1 replacive symplectite reaction from the compositions of

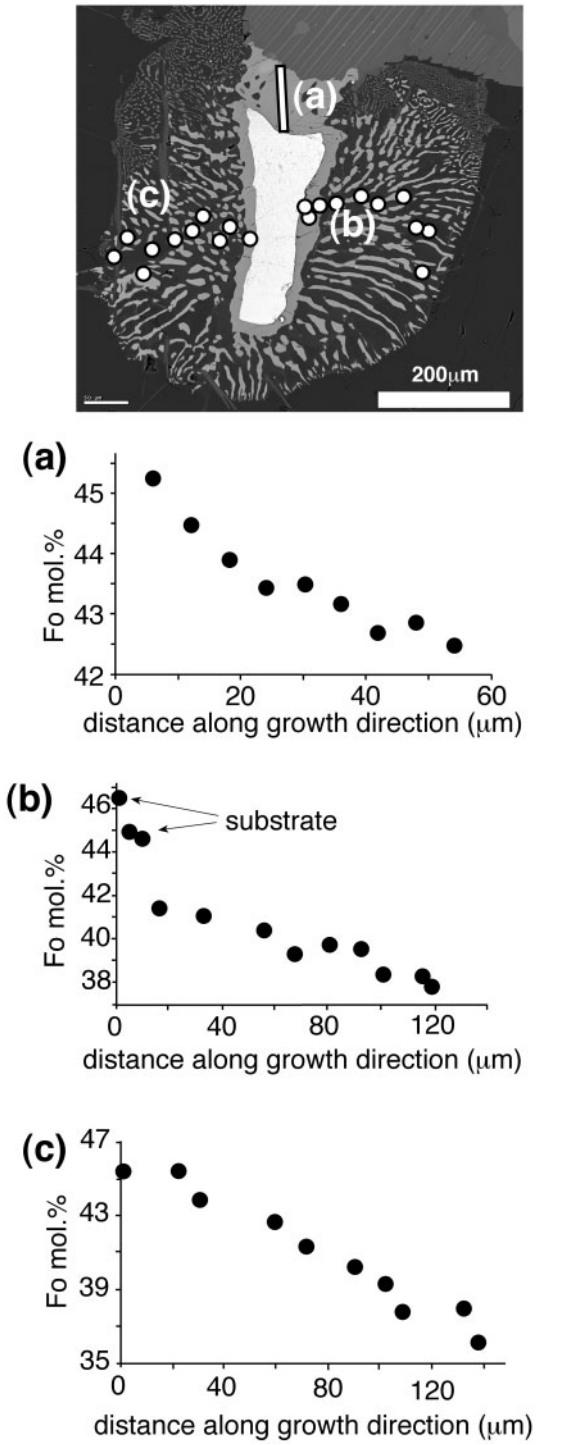

Fig. 16. Variation of olivine composition with position in a Type 1 symplectite (from 1026 m depth in drill core 90-22, MZ). The positions of the three traverses (a), (b) and (c) are shown in the BSE image at the top of the figure.

coexisting mineral phases, using QUILF (Andersen *et al.*, 1993) assuming pressures of $2{\cdot}3 \pm 0{\cdot}8$ kbar (Larsen & Tegner, 2006). Coexisting two-pyroxene and olivine–clinopyroxene vermicule pairs from the symplectitic intergrowths in a sample from drill core 90-22 at the level of the Triple Group yielded temperatures of 824°C and 873°C respectively. These are likely to be minimum values owing to resetting of Mg and Fe ratios by diffusion.

The estimated minimum temperatures for the symplectite reaction are lower than the lower-bound liquidus temperature estimated for the bulk magma at UZc times (980–950°C at 600 ± 100 bars (Lindsley *et al.*, 1969; Morse, 2008*a*) but higher than the granitic eutectic minimum (680–660°C, Larsen & Tegner, 2006), as well as the temperatures for the main pulse of meteoric–hydrothermal activity (500–750°C) (Manning & Bird, 1986), and the temperature of transgressive granophyre formation ($\sim 550 \pm 50$°C, Hirshmann, 1992). The estimated minimum temperature range is similar to that of pegmatitic granophyre formation, which was placed at 790°C in LZa, 824°C in LZb and 829°C in LZc by Larsen & Tegner (2006), at 655–770°C by Bird *et al.* (1991), and at 766–1006°C for gabbro pegmatite formation (Larsen & Brooks, 1994). Temperatures of replacive symplectite formation are also similar to zircon saturation temperatures for late differentiates of the Skaergaard magma placed at 787–806°C by Watson & Harrison (2005).

MASS BALANCE

Qualitative constraints can be placed on the reactions involved in the late-stage reactive microstructures, using average mineral compositions and volumetric proportions, and assuming that the irregular 2D shapes of the microstructures are representative of their 3D volumes. The evidence presented in Fig. 2 is consistent with stepped grain boundary formation by the replacement of plagioclase primocrysts and Ca-poor pyroxene by Ca-rich pyroxene and anorthite, although the exact proportions involved in the reaction depend on the position of the original grain boundary. However, in general the reaction necessitates addition of Ca, and removal of Al, Si and Na. If the small Fe–Ti oxide and apatite grains commonly present on stepped grain boundaries are also considered, the reaction requires greater amounts of Ca and also Fe, Ti, P and H_2O.

A similar result is obtained for the fish-hook pyroxene reaction. If we assume that the An-rich plagioclase and vermicular clinopyroxene replaced primocryst plagioclase, fish-hook formation involved the loss of Si, Al and Na, and the gain of Mg, Ca and Fe. The stepped grain boundaries and fish-hook pyroxenes are therefore likely to have formed by reaction with a late-stage hydrous, P-, Fe- and Ti-bearing liquid. The high Cl content of the apatite is consistent with a highly evolved liquid. The non-ubiquity of

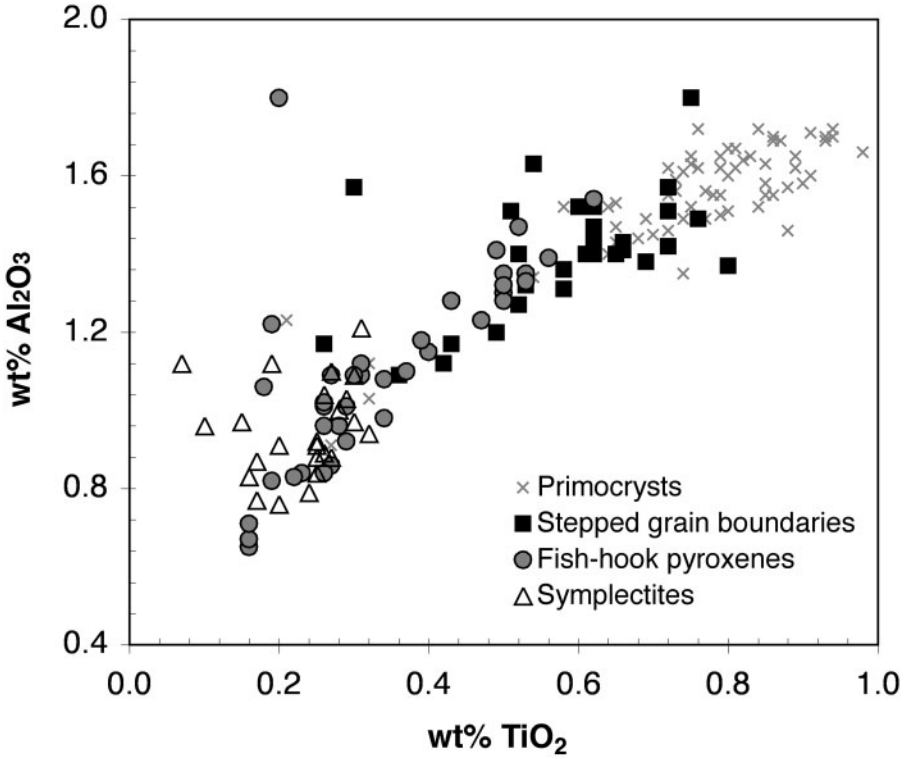

Fig. 17. Variation of augite composition in the late-stage microstructures, compared with that in cumulus augite for MZ. The smoothly changing composition from cumulus, through stepped grain boundaries and fish-hooks to symplectites, should be noted. Representative analyses can be found in Table 3 (for a full dataset of analyses see the Supplementary Dataset 3).

the steps on a grain-scale suggests that this liquid was not present on all grain boundaries.

For the Type 1 symplectites the exact reaction depends on the extent to which the oxide has been replaced by the symplectite: this is difficult to determine on textural grounds. Assuming constant compositions of symplectite phases, Type 1 symplectites require addition of Fe and Mg and the removal of Si, Na and Al, with little change in K, Mn and Ca. The mobility of Ti depends on assumptions about whether the Fe–Ti oxide root takes part in the reaction: if not then Ti is unchanged; otherwise it is removed. These conclusions are consistent with formation by interaction with a similar liquid to that responsible for the stepped grain boundaries and the fish-hook pyroxenes.

INTERPRETATION OF LATE-STAGE MICROSTRUCTURES

In the following discussion we demonstrate that the late-stage microstructures represent the solidified remnants of highly evolved interstitial silicate liquids that have undergone immiscibility. We argue that the differences between the sequence of late-stage microstructures in the Layered Series and the Marginal Border Series are caused by the different orientations of their solidification front relative to gravity and to differences in their cooling rate. Gravitationally driven liquid migration parallel to the solidification front in the vertical MBS did not result in discernible geochemical effects, but fluid migration in the horizontal Layered Series caused abundant reaction in the later stages of solidification. The prime cause of this late-stage reactivity of the interstitial liquid is the separation of the two conjugate liquids after the onset of immiscibility, with the preferential removal of the Si-rich conjugate leaving behind a reactive Fe-rich liquid.

Marginal Border Series

The late-stage microstructures in the upper parts of the MBS (i.e. the Skaergaard Peninsula) form a progression from a zone with partial replacement of olivine by either oxy-symplectites or orthopyroxene, through a zone with no apparent late-stage reactions but small interstitial pockets of evolved minerals, to a zone in which evidence of reaction occurs locally on grain boundaries between oxide and pyroxene grains. This reaction ceases on the arrival of the paired association of interstitial granophyre and ilmenite-rich intergrowths within MZ*. With the exception of the ilmenite-rich intergrowths, all these microstructures have been described and studied in other intrusions,

Table 3: Representative analyses of clinopyroxene from 1000·08 m depth in drill core 90-22 (MZ)

	Stepped grain boundary							
SiO_2	51·16	51·40	51·10	50·90	51·68	51·96	51·34	51·52
TiO_2	0·66	0·49	0·80	0·72	0·42	0·36	0·58	0·69
Al_2O_3	1·41	1·20	1·37	1·51	1·12	1·09	1·36	1·38
Fe_2O_3	0·13	0·83	0·48	0·41	0·65	0·00	0·37	0·15
FeO	12·73	12·26	12·50	12·55	10·96	12·56	12·97	12·30
MnO	0·33	0·33	0·34	0·32	0·28	0·31	0·31	0·33
MgO	11·87	12·11	12·05	12·14	12·51	12·19	11·77	12·01
CaO	20·71	20·86	20·61	20·22	21·57	20·77	20·71	21·18
Na_2O	0·22	0·21	0·23	0·23	0·21	0·20	0·24	0·22
Total	99·22	99·69	99·48	99·00	99·40	99·44	99·65	99·78
Si	1·96	1·96	1·95	1·95	1·96	1·98	1·96	1·96
Ti	0·02	0·01	0·02	0·02	0·01	0·01	0·02	0·02
Al	0·06	0·05	0·06	0·07	0·05	0·05	0·06	0·06
Fe^{3+}	0·00	0·02	0·01	0·01	0·02	0·00	0·01	0·00
Fe^{2+}	0·41	0·39	0·40	0·40	0·35	0·40	0·41	0·39
Mn	0·01	0·01	0·01	0·01	0·01	0·01	0·01	0·01
Mg	0·68	0·69	0·69	0·69	0·71	0·69	0·67	0·68
Ca	0·85	0·85	0·84	0·83	0·88	0·85	0·85	0·86
Na	0·02	0·02	0·02	0·02	0·02	0·02	0·02	0·02
Sum	4·00	4·00	4·00	4·00	4·00	4·00	4·00	4·00
Mg no.	61·8	63·1	62·6	62·7	66·5	62·8	61·2	62·9
	Symplectite							
SiO_2	52·26	52·39	52·15	52·32	52·29	52·52	52·71	52·99
TiO_2	0·25	0·20	0·27	0·30	0·29	0·25	0·25	0·19
Al_2O_3	0·84	0·76	0·88	0·97	1·03	0·88	0·91	1·12
Fe_2O_3	0·00	0·00	0·00	0·00	0·00	0·00	0·00	0·00
FeO	11·71	11·56	12·64	12·62	12·35	12·27	12·21	10·02
MnO	0·28	0·29	0·26	0·29	0·30	0·26	0·27	0·22
MgO	12·23	12·65	11·98	12·05	12·12	12·38	12·30	13·46
CaO	21·33	21·15	21·15	20·76	20·72	20·95	20·81	21·69
Na_2O	0·20	0·16	0·19	0·18	0·17	0·17	0·17	0·15
Total	99·10	99·16	99·52	99·49	99·27	99·68	99·63	99·84
Si	1·99	1·99	1·98	1·99	1·99	1·99	1·99	1·98
Ti	0·01	0·01	0·01	0·01	0·01	0·01	0·01	0·01
Al	0·04	0·03	0·04	0·04	0·05	0·04	0·04	0·05
Fe^{3+}	0·00	0·00	0·00	0·00	0·00	0·00	0·00	0·00
Fe^{2+}	0·37	0·37	0·40	0·40	0·39	0·39	0·39	0·31
Mn	0·01	0·01	0·01	0·01	0·01	0·01	0·01	0·01
Mg	0·69	0·72	0·68	0·68	0·69	0·70	0·69	0·75
Ca	0·87	0·86	0·86	0·85	0·84	0·85	0·84	0·87
Na	0·02	0·01	0·01	0·01	0·01	0·01	0·01	0·01
Sum	3·99	3·99	4·00	3·99	3·99	3·99	3·99	3·99
Mg no.	64·5	65·6	62·4	62·5	63·0	63·8	63·7	70·1

(continued)

Table 3: Continued

	Fish-hook pyroxene							
SiO_2	51·87	51·87	51·74	52·44	51·94	51·15	51·93	51·79
TiO_2	0·26	0·29	0·29	0·19	0·26	0·26	0·16	0·22
Al_2O_3	0·96	0·92	1·01	0·82	0·96	0·84	0·67	0·83
Fe_2O_3	0·50	0·83	0·54	0·00	0·47	0·56	0·34	0·08
FeO	11·56	12·18	11·48	11·47	11·31	12·66	12·09	12·16
MnO	0·26	0·26	0·32	0·28	0·27	0·30	0·27	0·25
MgO	12·58	12·11	12·74	12·89	12·54	11·46	11·83	11·96
CaO	21·12	21·27	20·85	21·25	21·52	21·28	21·80	21·45
Na_2O	0·20	0·21	0·19	0·16	0·18	0·16	0·18	0·19
Total	99·31	99·94	99·16	99·50	99·45	98·67	99·27	98·93
Si	1·97	1·97	1·97	1·98	1·97	1·97	1·98	1·98
Ti	0·01	0·01	0·01	0·01	0·01	0·01	0·01	0·01
Al	0·04	0·04	0·05	0·04	0·04	0·04	0·03	0·04
Fe^{3+}	0·01	0·02	0·02	0·00	0·01	0·02	0·01	0·00
Fe^{2+}	0·37	0·39	0·37	0·36	0·36	0·41	0·39	0·39
Mn	0·01	0·01	0·01	0·01	0·01	0·01	0·01	0·01
Mg	0·71	0·69	0·72	0·73	0·71	0·66	0·67	0·68
Ca	0·86	0·86	0·85	0·86	0·88	0·88	0·89	0·88
Na	0·02	0·02	0·01	0·01	0·01	0·01	0·01	0·01
Sum	4·00	4·00	4·00	4·00	4·00	4·00	4·00	4·00
Mg no.	65·5	63·5	65·8	66·2	65·8	61·2	63·0	63·2
	Primocryst							
SiO_2	50·77	50·84	50·55	50·61	50·41	50·61	50·79	50·17
TiO_2	0·68	0·64	0·65	0·80	0·78	0·86	0·91	0·94
Al_2O_3	1·44	1·40	1·43	1·51	1·55	1·69	1·60	1·70
Fe_2O_3	1·09	0·78	1·62	1·46	1·52	1·61	1·44	1·53
FeO	11·89	13·30	11·16	12·40	11·96	13·14	11·64	11·45
MnO	0·31	0·38	0·35	0·35	0·34	0·32	0·37	0·31
MgO	12·16	12·20	12·20	12·27	12·03	12·36	12·11	12·05
CaO	20·66	19·50	20·95	19·99	20·46	19·28	20·88	20·72
Na_2O	0·21	0·20	0·20	0·21	0·22	0·23	0·26	0·22
Total	99·21	99·24	99·11	99·60	99·27	100·10	100·00	99·09
Si	1·94	1·95	1·93	1·93	1·93	1·92	1·93	1·92
Ti	0·02	0·02	0·02	0·02	0·02	0·03	0·03	0·03
Al	0·07	0·06	0·06	0·07	0·07	0·08	0·07	0·08
Fe^{3+}	0·03	0·02	0·05	0·04	0·04	0·05	0·04	0·04
Fe^{2+}	0·38	0·43	0·36	0·40	0·38	0·42	0·37	0·37
Mn	0·01	0·01	0·01	0·01	0·01	0·01	0·01	0·01
Mg	0·69	0·70	0·70	0·70	0·69	0·70	0·69	0·69
Ca	0·85	0·80	0·86	0·82	0·84	0·79	0·85	0·85
Na	0·02	0·02	0·02	0·02	0·02	0·02	0·02	0·02
Sum	4·00	4·00	4·00	4·00	4·00	4·00	4·00	4·00
Mg no.	64·0	61·4	65·4	63·2	63·5	62·1	64·3	64·6

Table 4: Representative analyses of orthopyroxene from 1000·08 m depth in drill core 90-22 (MZ)

	Fish-hook pyroxene		Ilmenite intergrowths					
SiO_2	51·15	51·86	49·34	50·19	50·57	50·72	50·06	50·12
TiO_2	0·15	0·12	0·36	0·29	0·73	0·54	0·18	0·65
Al_2O_3	0·49	0·42	0·25	0·35	0·32	0·31	0·37	0·28
Fe_2O_3	0·17	0·71	0·00	0·00	0·00	0·00	0·00	0·00
FeO	29·59	27·32	33·96	33·83	34·77	34·55	33·42	34·37
MnO	0·64	0·59	0·62	0·63	0·62	0·65	0·60	0·61
MgO	16·71	18·55	12·89	12·71	12·64	12·69	13·26	12·50
CaO	0·90	0·86	1·05	1·19	1·17	0·95	1·14	1·08
Total	99·80	100·43	98·50	99·21	100·90	100·46	99·08	99·64
Si	1·98	1·98	1·99	2·00	1·99	2·00	2·00	1·99
Ti	0·00	0·00	0·01	0·01	0·02	0·02	0·01	0·02
Al	0·02	0·02	0·01	0·02	0·02	0·01	0·02	0·01
Fe^{3+}	0·01	0·02	0·00	0·00	0·00	0·00	0·00	0·00
Fe^{2+}	0·96	0·87	1·14	1·13	1·14	1·14	1·11	1·14
Mn	0·02	0·02	0·02	0·02	0·02	0·02	0·02	0·02
Mg	0·97	1·05	0·77	0·76	0·74	0·75	0·79	0·74
Ca	0·04	0·04	0·05	0·05	0·05	0·04	0·05	0·05
Sum	4·00	4·00	4·00	3·98	3·99	3·98	3·99	3·98
Mg-no.	50·0	54·2	40·4	40·1	39·3	39·5	41·4	39·3
	Symplectite							
SiO_2	51·48	51·33	51·83	51·41	51·18	51·78	51·44	51·41
TiO_2	0·14	0·16	0·13	0·17	0·15	0·12	0·14	0·17
Al_2O_3	0·71	0·56	0·46	0·58	0·46	0·57	0·59	0·58
Fe_2O_3	0·05	1·33	0·79	0·05	0·17	0·00	0·64	0·05
FeO	26·75	26·98	26·91	27·03	28·06	26·56	26·22	27·03
MnO	0·55	0·56	0·59	0·54	0·59	0·56	0·58	0·54
MgO	18·60	18·36	18·86	18·31	17·55	18·60	18·84	18·31
CaO	0·86	0·85	0·65	0·94	1·02	0·86	0·94	0·94
Total	99·14	100·13	100·22	99·03	99·18	99·05	99·39	99·03
Si	1·98	1·97	1·98	1·98	1·98	1·99	1·97	1·98
Ti	0·00	0·01	0·00	0·01	0·00	0·00	0·00	0·01
Al	0·03	0·03	0·02	0·03	0·02	0·03	0·03	0·03
Fe^{3+}	0·00	0·04	0·02	0·00	0·01	0·00	0·02	0·00
Fe^{2+}	0·86	0·86	0·86	0·87	0·91	0·85	0·84	0·87
Mn	0·02	0·02	0·02	0·02	0·02	0·02	0·02	0·02
Mg	1·07	1·05	1·07	1·05	1·01	1·07	1·08	1·05
Ca	0·04	0·04	0·03	0·04	0·04	0·04	0·04	0·04
Sum	4·00	4·00	4·00	4·00	4·00	3·99	4·00	4·00
Mg-no.	55·3	53·7	54·9	54·7	52·6	55·5	55·6	54·7

(continued)

Table 4: Representative analyses of orthopyroxene from 1000·08 m depth in drill core 90-22 (MZ)

	Symplectite substrate							
SiO_2	52·04	51·79	51·72	51·94	52·13	51·71	51·51	51·42
TiO_2	0·19	0·25	0·20	0·21	0·14	0·26	0·20	0·21
Al_2O_3	0·57	0·63	0·64	0·67	0·52	0·68	0·60	0·56
Fe_2O_3	0·00	0·00	0·68	0·48	0·00	0·00	1·44	0·66
FeO	25·86	26·14	25·90	25·80	25·86	25·61	25·93	26·96
MnO	0·56	0·55	0·53	0·53	0·55	0·56	0·57	0·60
MgO	19·26	18·56	19·18	19·36	19·53	19·09	18·91	18·33
CaO	1·00	1·20	0·99	1·03	0·88	1·21	1·05	1·03
Total	99·48	99·12	99·84	100·02	99·61	99·12	100·21	99·77
Si	1·99	1·99	1·97	1·97	1·99	1·98	1·96	1·97
Ti	0·01	0·01	0·01	0·01	0·00	0·01	0·01	0·01
Al	0·03	0·03	0·03	0·03	0·02	0·03	0·03	0·03
Fe^{3+}	0·00	0·00	0·02	0·01	0·00	0·00	0·04	0·02
Fe^{2+}	0·83	0·84	0·83	0·82	0·82	0·82	0·83	0·87
Mn	0·02	0·02	0·02	0·02	0·02	0·02	0·02	0·02
Mg	1·10	1·06	1·09	1·10	1·11	1·09	1·07	1·05
Ca	0·04	0·05	0·04	0·04	0·04	0·05	0·04	0·04
Sum	4·00	3·99	4·00	4·00	4·00	4·00	4·00	4·00
Mg-no.	57·0	55·8	56·3	56·8	57·3	57·0	55·3	54·2
	Primocryst							
SiO_2	51·03	52·04	51·44	51·88	52·35	51·47	51·58	51·98
TiO_2	0·31	0·19	0·22	0·21	0·27	0·15	0·27	0·21
Al_2O_3	0·52	0·57	0·58	0·46	0·65	0·37	0·66	0·65
Fe_2O_3	0·58	0·00	0·25	0·00	0·00	0·00	0·00	0·00
FeO	28·26	28·38	27·68	28·68	25·61	30·77	27·98	25·25
MnO	0·68	0·65	0·64	0·64	0·63	0·73	0·63	0·58
MgO	16·78	17·51	16·96	16·92	16·09	15·95	16·66	16·96
CaO	1·80	1·17	2·33	1·41	3·10	1·01	2·51	3·12
Total	99·96	100·51	100·10	100·20	98·70	100·45	100·29	98·75
Si	1·97	1·99	1·98	1·99	2·02	1·99	1·98	2·00
Ti	0·01	0·01	0·01	0·01	0·01	0·00	0·01	0·01
Al	0·02	0·03	0·03	0·02	0·03	0·02	0·03	0·03
Fe^{3+}	0·02	0·00	0·01	0·00	0·00	0·00	0·00	0·00
Fe^{2+}	0·91	0·91	0·89	0·92	0·83	1·00	0·90	0·81
Mn	0·02	0·02	0·02	0·02	0·02	0·02	0·02	0·02
Mg	0·97	1·00	0·97	0·97	0·93	0·92	0·95	0·97
Ca	0·08	0·05	0·10	0·06	0·13	0·04	0·10	0·13
Sum	4·00	4·00	4·00	3·99	3·96	4·00	4·00	3·98
Mg-no.	50·9	52·4	52·0	51·2	52·8	48·0	51·5	54·5

Analyses of orthopyroxene in ilmenite-rich intergrowths are from 1015·06 m depth (MZ).

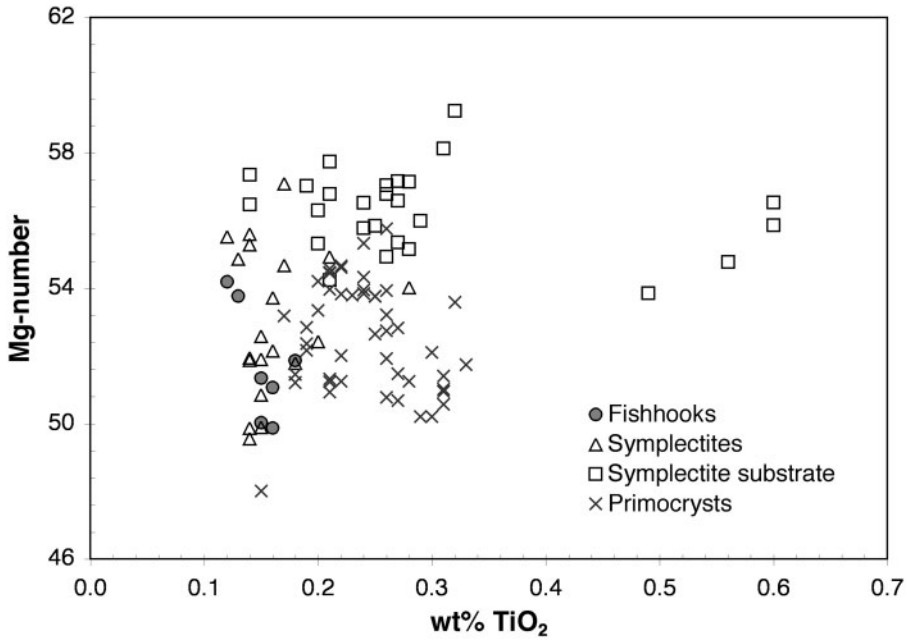

Fig. 18. Variation of orthopyroxene composition in the late-stage microstructures compared with cumulus for MZ. Representative analyses can be found in Table 4 (for a full dataset of analyses see the Supplementary Dataset 4).

Table 5: Representative analyses of cumulus apatite (from 461·8 m depth in drill core 90-22, UZb), and grain boundary apatite (from 907 m depth in drill core 90-22, UZa)

	Primocryst							
P_2O_5	42·17	42·30	41·75	41·74	40·29	41·79	41·12	40·48
FeO	0·20	0·25	0·26	0·16	0·35	0·21	0·32	0·31
MnO	0·07	0·03	0·04	0·03	0·07	0·05	0·07	0·04
MgO	0·06	0·08	0·09	0·04	0·14	0·05	0·08	0·06
CaO	54·66	54·79	54·49	55·03	54·40	54·77	54·23	54·37
F	2·44	2·59	2·63	2·79	2·83	2·93	3·17	3·26
Cl	0·05	0·06	0·06	0·05	0·06	0·06	0·07	0·06
Total	99·72	100·12	99·36	99·87	98·18	99·89	99·10	98·62
	Grain boundary apatite							
P_2O_5	41·77	42·53	41·48	43·26	41·92	41·76	41·64	42·58
FeO	0·24	0·27	0·20	0·20	0·31	0·15	0·16	0·31
MnO	0·03	0·05	0·07	0·04	0·02		0·03	0·04
MgO	0·00	0·00	0·00	0·00	0·00	0·00	0·00	0·01
CaO	54·57	55·13	54·36	54·41	54·49	54·70	54·80	54·83
F	3·04	2·52	2·91	2·27	2·44	2·58	2·75	1·89
Cl	0·43	0·40	0·42	0·43	0·46	0·42	0·44	0·29
Total	100·13	100·91	99·47	100·62	99·66	99·65	99·87	99·99

Table 6: Representative compositions of Fe–Ti oxides from 1000·08 m depth in drill core 90-22 (MZ, cumulus and grain boundary oxides) and 40·9 m depth in drill core 90-22 (UZb, cumulus and ilmenite-rich intergrowths)

	Primocryst from sample 1000.08									
SiO_2	0·08	0·06	0·04	0·07	0·08	0·07	0·08	0·11	0·10	0·11
TiO_2	50·78	50·68	51·42	50·49	51·09	51·12	6·91	9·42	9·80	9·10
Al_2O_3	0·00	0·00	0·00	0·01	0·00	0·00	3·04	2·80	3·90	3·60
FeO	46·11	45·59	45·26	45·60	45·46	45·75	83·61	82·01	80·43	80·38
MnO	0·47	0·49	0·55	0·48	0·52	0·49	0·19	0·19	0·25	0·36
MgO	1·85	1·90	1·51	1·87	1·85	1·80	0·61	0·53	0·73	0·60
Total	99·31	98·74	98·82	98·53	99·02	99·26	94·49	95·09	95·26	94·20
Si	0·003	0·002	0·002	0·003	0·003	0·003	0·004	0·005	0·005	0·006
Ti	1·433	1·438	1·464	1·435	1·446	1·444	0·260	0·354	0·366	0·344
Al	0·000	0·000	0·000	0·000	0·000	0·000	0·179	0·165	0·228	0·213
Fe^{3+}	0·129	0·120	0·070	0·124	0·102	0·106	1·958	1·782	1·697	1·755
Fe^{2+}	1·317	1·317	1·362	1·317	1·329	1·330	1·544	1·645	1·640	1·623
Mn	0·015	0·016	0·018	0·015	0·017	0·016	0·008	0·008	0·011	0·015
Mg	0·103	0·107	0·085	0·105	0·104	0·101	0·046	0·039	0·054	0·045
Mol % Usp							0·219	0·297	0·320	0·298
Mol % Ilm	0·955	0·958	0·976	0·957	0·965	0·963				

	Grain-boundary oxide from sample 1000.08							
SiO_2	0·05	0·09	0·07	0·08	0·08	0·07	0·11	0·08
TiO_2	50·26	50·00	50·13	25·72	14·56	19·28	15·55	14·57
Al_2O_3	0·00	0·03	0·00	0·72	0·52	1·53	0·99	0·95
FeO	46·76	45·58	46·37	67·41	78·32	72·36	76·77	78·43
MnO	0·82	0·76	0·61	0·38	0·35	0·41	0·41	0·38
MgO	0·25	0·79	0·18	0·23	0·16	0·38	0·28	0·27
Total	98·45	97·61	97·61	94·77	94·21	94·29	94·28	94·88
Si	0·002	0·003	0·003	0·003	0·003	0·003	0·004	0·003
Ti	1·454	1·453	1·463	0·751	0·423	0·559	0·450	0·419
Al	0·000	0·001	0·000	0·033	0·024	0·070	0·045	0·043
Fe^{3+}	0·089	0·086	0·069	1·459	2·124	1·807	2·046	2·113
Fe^{2+}	1·415	1·386	1·435	0·728	0·405	0·527	0·425	0·394
Mn	0·027	0·025	0·020	0·012	0·011	0·013	0·013	0·012
Mg	0·014	0·045	0·010	0·013	0·009	0·022	0·016	0·015
Mol % Usp				0·775	0·431	0·596	0·468	0·434
Mol % Ilm	0·970	0·970	0·977					

	Ilmenite intergrowths from sample 40.9							
SiO_2	0·03	0·04	0·03	0·02	0·05	0·05	0·05	0·08
TiO_2	52·27	51·75	52·18	51·76	52·15	52·02	51·72	51·59
Al_2O_3	0·00	0·00	0·00	0·00	0·00	0·00	0·00	0·00
Fe_2O_3	0·64	2·26	1·27	1·19	1·03	0·82	1·39	1·42
FeO	45·74	45·40	45·69	45·29	45·45	45·47	45·02	44·78
MnO	1·23	1·16	1·21	1·22	1·39	1·31	1·43	1·53
MgO	0·01	0·00	0·00	0·00	0·00	0·01	0·00	0·00

(continued)

Table 6: Continued

	Ilmenite intergrowths from sample 40.9							
CaO	0·03	0·01	0·03	0·03	0·08	0·02	0·08	0·12
Total	99·88	100·39	100·30	99·40	100·04	99·63	99·56	99·40
Si	0·001	0·001	0·001	0·001	0·001	0·001	0·001	0·002
Ti	0·999	0·999	0·999	1·000	0·999	0·999	0·999	0·998
Al	0·000	0·000	0·000	0·000	0·000	0·000	0·000	0·000
Fe^{3+}	0·000	0·000	0·000	0·000	0·000	0·000	0·000	0·000
Fe^{2+}	0·972	0·975	0·973	0·973	0·968	0·971	0·967	0·964
Mn	0·026	0·025	0·026	0·027	0·030	0·028	0·031	0·033
Mg	0·000	0·000	0·000	0·000	0·000	0·000	0·000	0·000
Ca	0·001	0·000	0·001	0·001	0·002	0·001	0·002	0·003
Mol % Ilm	1·000	1·000	1·000	1·000	1·000	1·000	1·000	1·000
	Primocryst from sample 40.9							
SiO_2	0·04	0·05	0·02	0·02	0·04	0·03	0·04	0·05
TiO_2	51·83	51·53	51·86	52·05	51·80	52·06	52·35	52·09
Al_2O_3	0·00	0·00	0·00	0·00	0·00	0·00	0·00	0·00
Fe_2O_3	1·41	1·91	1·91	1·16	1·73	0·92	0·57	0·62
FeO	45·25	44·96	45·30	45·44	45·37	45·50	45·88	45·74
MnO	1·32	1·36	1·26	1·31	1·16	1·24	1·14	1·05
MgO	0·03	0·02	0·03	0·03	0·03	0·04	0·03	0·04
CaO	0·01	0·02	0·02	0·01	0·02	0·02	0·03	0·02
Total	99·75	99·66	100·21	99·91	99·98	99·72	100·00	99·55
Si	0·001	0·001	0·001	0·001	0·001	0·001	0·001	0·001
Ti	0·999	0·999	1·000	1·000	0·999	0·999	0·999	0·999
Al	0·000	0·000	0·000	0·000	0·000	0·000	0·000	0·000
Fe^{3+}	0·000	0·000	0·000	0·000	0·000	0·000	0·000	0·000
Fe^{2+}	0·970	0·969	0·971	0·970	0·973	0·971	0·974	0·975
Mn	0·029	0·030	0·027	0·028	0·025	0·027	0·024	0·023
Mg	0·001	0·001	0·001	0·001	0·001	0·002	0·001	0·002
Ca	0·000	0·001	0·001	0·000	0·001	0·001	0·001	0·001
Mol % Ilm	1·000	1·000	1·000	1·000	1·000	1·000	1·000	1·000

End-member proportions calculated using Stormer (1983).

although their detailed spatial distribution within a single intrusion has not previously been documented.

The paired non-reactive microstructures (granophyre and the ilmenite-rich intergrowths, Figs 10–12) indicate crystallization of late-stage, multiply saturated liquids in chemical equilibrium with their bounding primocryst phases. Their contrasting compositions suggest a pair of immiscible liquids, one Si-rich and the other rich in Fe and Ti. This interpretation is consistent with that of McBirney & Nakamura (1974), Larsen & Brooks (1994) and Jakobsen *et al.* (2005), who all ascribed the interstitial granophyre to the silicic component of a conjugate pair of immiscible liquids. Where we depart from these researchers is in identifying the ilmenite-rich intergrowths as the other liquid of this conjugate pair.

Microstructures previously attributed to the presence of an Fe-rich conjugate include the development of lobate crystal faces on pyroxene crystals growing in a Si-dominated liquid containing droplets of the minor Fe-rich phase (Philpotts & Doyle, 1983), and aggregates of pyroxene, magnetite, ilmenite and apatite, which are thought to be the result of crystallization of droplets of Fe-rich liquid (Philpotts, 1981). We speculate that the granophyric pockets containing apatite ± magnetite and/or biotite, and the evolved interstitial pockets, represent the crystallization products of incompletely separated

Table 7: Representative analyses of interstitial biotite (from sample 118601, 1966 drill core, LZb), and symplectite biotite (from 1000·08 m depth, drill core 90-22, MZ)

	Interstitial biotite							
SiO_2	38·54	39·01	38·50	38·81	38·66	38·50	38·53	38·63
TiO_2	3·93	4·44	4·82	3·66	4·23	4·66	5·04	4·49
Al_2O_3	14·85	14·50	14·63	14·82	14·78	14·56	14·44	14·63
Fe_2O_3	0·27	0·00	0·00	1·31	0·00	0·00	0·00	0·00
FeO	7·47	8·71	9·50	7·02	8·17	8·41	8·50	9·44
MnO	0·04	0·02	0·06	0·03	0·03	0·04	0·04	0·03
MgO	20·07	19·32	18·37	20·14	19·78	19·32	19·09	18·87
CaO	0·04	0·03	0·07	0·12	0·04	0·05	0·03	0·09
Na_2O	0·46	0·50	0·40	0·43	0·45	0·43	0·39	0·40
K_2O	9·17	9·09	8·92	8·89	9·22	9·14	9·11	9·05
F	1·04	0·95	0·90	1·01	1·02	0·99	0·95	0·96
Total	95·88	96·57	96·17	96·24	96·38	96·10	96·12	96·59
	Symplectite biotite							
SiO_2	38·88	38·46	39·02	39·30	39·01	37·97	38·31	38·13
TiO_2	2·22	2·67	2·64	2·64	2·33	2·67	2·66	2·59
Al_2O_3	15·65	15·82	15·76	15·37	15·56	15·67	15·61	15·65
Fe_2O_3	1·54	1·68	1·74	1·67	1·54	1·55	1·58	1·67
FeO	7·83	8·54	8·86	8·50	7·86	7·89	8·05	8·51
MnO	0·02	0·05	0·03	0·02	0·02	0·04	0·04	0·05
MgO	20·37	18·77	18·59	19·26	19·61	20·57	19·55	18·97
CaO	0·18	0·08	0·10	0·06	0·05	0·14	0·11	0·23
Na_2O	0·11	0·08	0·11	0·09	0·22	0·03	0·05	0·06
K_2O	8·40	8·96	8·87	9·39	8·76	9·03	9·45	8·69
F	1·09	1·11	1·15	1·07	1·18	1·12	1·19	1·20
Total	96·29	96·22	96·87	97·37	96·14	96·68	96·60	95·75

immiscible liquids, perhaps as a result of limited time for droplet coarsening.

The oxy-symplectites replacing olivine where in contact with interstitial Fe–Ti oxides (Fig. 7) have been described by Barton & van Gaans (1988) from the Hidra and Lyngal intrusions, where olivine is also replaced by orthopyroxene. In common with these workers we suggest that the oxy-symplectites can be attributed to an increase in fO_2 of residual liquids during the last stages of solidification. A decrease in fO_2 would trigger the reverse reaction, creating poly-crystalline olivine rims according to a reaction of the type

$$2Fe_3O_4 + 3(Fe,Mg)_2Si_2O_6 = 6(Fe,Mg)_2SiO_4 + O_2$$

or more generally

$$\text{magnetite} + \text{pyroxene} \pm Al_2O_3 = \text{olivine} \pm \text{anorthite} \pm CaO + O_2.$$

Ca must be released by reaction between augite and magnetite, because the volumetric proportion of anorthite in the poly-crystalline rims is insufficient to account for all the Ca in the augite. It is not clear what happens to this calcium.

We find compelling the clear spatial distinction between the oxy-symplectites, which are found only in the most primitive parts of the intrusion, and the evidence for the reverse reaction, which is separated from the oxy-symplectite zone by an intermediate zone with no evidence for late-stage reactions. Exceptions to this general rule are provided by isolated examples of olivine rims surrounding large interstitial oxide grains within the intermediate, otherwise reaction-free, zone. We suggest that this spatial control is due to an underlying control on the changes of oxygen fugacity with differentiation.

This interpretation is supported by the calculations of Thy *et al.* (2009) that show fO_2 as a function of temperature within the bulk liquid using a range of assumed magnetite:ilmenite ratios. Regardless of the ratio of oxide phases, the calculated fO_2 increases through LZa and remains constant until the onset of liquid saturation in oxides, whereupon it decreases to below FMQ. Crystallization of Fe–Ti oxides triggers a reduction in fO_2, which results in destabilization of magnetite and pyroxene to form olivine and ilmenite. Broadly, these changes correspond to the spatial distribution of late-stage reactions involving oxides in LZa* through to MZ*, with the onset of rim growth coinciding with the arrival of cumulus oxides at the LZb*–LZc* boundary. The exceptions to this rule (the olivine rims surrounding large isolated oxide grains in the otherwise reaction-free zone) suggest that overgrowth of the oxide grains during late-stage solidification was sufficient to locally drive down fO_2 in the remaining interstitial liquid and trigger olivine rim growth.

Although it is possible that the abrupt appearance of poly-crystalline rims at the LZb*–LZc* boundary is due to the abundance of reactive oxide surfaces and a step-wise increase in reaction rates, it is also possible that the composition (and hence fO_2) of the interstitial liquid in the MBS may have been closely tracking that of the bulk magma for much of its solidification history; in such a case then mush permeability was high. A high permeability would lead to open communication with the bulk magma such that the interstitial liquid would not be able to evolve to saturation in oxides (and hence onto a path of decreasing fO_2 with increasing crystallization) until the bulk liquid itself became saturated in oxides. Observations of continuous films of glass on grain boundaries led Holness *et al.* (2007*a*) to suggest pervasive melt interconnectivity in low-porosity solidifying gabbros. That liquid films were present on oxide boundaries in the Skaergaard MBS is evident from the common (non-reactive) mono-crystalline rims of plagioclase in the zone separating the oxy-symplectite and poly-crystalline rim zones.

The mono-crystalline olivine rims probably are at least partly related to the poly-crystalline rims. Mono-crystalline olivine rims have higher P concentrations than all other Skaergaard olivine (Table 2 and Supplementary Dataset 2), suggesting that they crystallized from a relatively P-rich (i.e. late) liquid. They are most common in LZc and UZa; that is, just before, and just after, the olivine primocryst-free MZ (Fig. 3d). Their optical continuity with adjacent olivine primocrysts suggests nucleation difficulties in the late melt-filled space: they are probably analogous to the clinopyroxene rims in the allivalites from the Rum Layered Series (Holness, 2005, 2007), and to the plagioclase rims common in the MBS and parts of the Layered Series in which oxides were not involved in reaction. However, it is likely that the presence of a pre-existing olivine grain would promote overgrowth of that grain were the magnetite–pyroxene reaction to occur: mono-crystalline rims are probably a combination of pseudomorphs of a liquid-filled grain boundary film and a reaction product.

We argue below that the horizontally accumulating Layered Series underwent significant redistribution of interstitial liquid, with a consequently strongly modified set of late-stage processes. In the vertically oriented MBS, gravitationally driven migration of the interstitial liquid can have fewer geochemical consequences and, at the moment of entrapment within the outermost region of the solidification front, the liquid has a composition close to that of the immediately adjacent bulk liquid. We consider highly significant the disappearance of the poly-crystalline olivine rims within MZ*, and their replacement by the paired association of Si-rich and Fe-rich intergrowths. We suggest that the appearance of abundant paired intergrowths marks the point at which the bulk liquid itself intersected the miscibility gap: when this occurs the initial mush porosity will be filled with varying proportions of exsolved liquid droplets that crystallize to form the paired non-reactive microstructures. This early onset of immiscibility in the bulk magma was also suggested by Jakobsen *et al.* (2006) and Veksler *et al.* (2007, 2008). Critically, suggestions of a later onset (within UZ) (McBirney & Nakamura, 1974; McBirney, 1975; Naslund, 1984; McBirney, 1989, 2002, 2008; Stewart & DePaolo, 1990; Jakobsen *et al.*, 2005) were based on studies of the Layered Series.

The late-stage MBS microstructures that remain to be discussed are the stepped grain boundaries and the Type 2 symplectites. The Type 2 symplectites bear a superficial resemblance to the textures ascribed to hydrous partial melting by Koepke *et al.* (2005*a*, 2005*b*): they replace olivine and they may contain amphibole. However, the hydrous partial melting reaction involves consumption of plagioclase and clinopyroxene as well as olivine, so we might expect symplectites forming by this reaction to be common on olivine–clinopyroxene grain boundaries. This is not the case; Type 2 symplectites are attached to olivine and consume plagioclase but not clinopyroxene. A further difficulty with assigning Type 2 symplectites to hydrous partial melting is that their plagioclase compositions are closer to those of Type 1 symplectites than to the plagioclase produced during hydrous partial melting (Table 1 and Supplementary Dataset 1). Additionally, if they were hydrous partial melting symplectites one might expect their distribution to reflect the distribution of high H_2O concentrations. Their concentration in the MBS is

certainly consistent with a reaction triggered by the influx of externally derived H_2O, but they are absent from the upper reaches of the intrusion where the greatest hydrothermal input is documented (Taylor & Forrester, 1979). They are also absent in the most fractionated parts of the intrusion where high concentrations of cognate H_2O would be expected. Instead, Type 2 symplectites are only present in the MBS in the structurally lower parts of the intrusion. We propose that all replacive symplectites are related, and formed by reaction with a significant volume of melt during the last stages of solidification of the Skaergaard intrusion; we will return to these below.

The stepped grain boundaries in the Skaergaard intrusion are different from those described by Roelofse *et al.* (2009) from the Bushveld intrusion, which involve a Ca-poor pyroxene host containing resorbed Ca-rich exsolution lamellae. Roelofse *et al.* (2009) suggested that they formed by percolation of new, hotter liquid into almost solidified cumulates. However, the stepped grain boundaries at Skaergaard cannot have formed by this mechanism, because of their distribution within the intrusion, the opposite mineralogical change, and because Skaergaard received no new magma influx after its emplacement. The nature of the reaction causing the Skaergaard stepped boundaries is enigmatic, although it clearly occurred in the super-solidus and involved addition of Fe and Ca, and removal of Al, Si and Na. Additionally, the clear transitional nature of the stepped grain boundaries, fish-hook pyroxene and symplectites (Figs 2g, 4d, 4f and 5d) suggests that they are all linked (discussed below). The distribution of stepped grain boundaries in Skaergaard does not correlate with modal mineralogy, in contrast to that of the oxy-symplectites and poly-crystalline rims. We therefore cannot attribute stepped grain boundary formation to the addition of Ca released by the growth of poly-crystalline olivine rims. The concentration of stepped grain boundaries in the centre of all traverses through the MBS, regardless of the stratigraphic position of the traverse, suggests that the availability of the reactive liquid was not tied to the liquidus assemblage or modal mineralogy. Instead, it was probably controlled by external factors such as cooling rate and mush thickness. Although the stepped grain boundaries clearly are an important component of the late-stage microstructures in both Skaergaard and Bushveld, we can offer few constraints on their formation or relationship with the other late-stage microstructures: they clearly merit further investigation.

Layered Series

The sequence of late-stage microstructures in the Layered Series differs from that in the MBS in several important respects. These differences are most marked in the central part of the Layered Series: late-stage microstructures in those parts of the Layered Series nearest the intrusion walls approach a similar distribution to that observed in the MBS.

As with the sequence of microstructures observed in the MBS, olivine grains are partially replaced by oxy-symplectites and orthopyroxene in the lower Layered Series (consistent with the presence of a single interstitial liquid evolving towards higher oxygen fugacity) and poly-crystalline rims arrive at the base of LZc. However, a notable feature of the Layered Series from mid-LZb upwards is the presence of fish-hook pyroxenes and oxide-rooted mafic symplectites replacing plagioclase primocrysts—these features formed by open-system reactions that resulted in the addition of Fe and Ca, and the removal of silica and alkalis. The mafic symplectites are closely related to the development of poly-crystalline olivine rims such that, in several cases, a single oxide grain develops a symplectite where in contact with plagioclase and a poly-crystalline olivine rim where in contact with clinopyroxene (Figs 5c, e, f and 9b). Although in both LS and MBS the presence of poly-crystalline olivine rims points to decreasing fO_2 in the interstitial liquid, the reactive liquid in the Layered Series must also allow growth of the more Fe-rich mineral compositions found in the reactive symplectites.

The arrival of the paired association of granophyre and ilmenite-rich intergrowths occurs much later in the Layered Series stratigraphy compared with the MBS, particularly in the centre of the intrusion where they do not make an appearance until UZb. At the margins of the Layered Series reactive symplectites are comparatively rare; they, and the poly-crystalline rims, disappear within MZ to be replaced by the paired conjugate intergrowths. The transition between reactive microstructures and paired conjugate intergrowths therefore cuts across stratigraphy within the Layered Series, and cannot be related to changes in liquidus assemblage or mineral composition. Furthermore, the liquidus phases present in both the MBS and the Layered Series are identical, with the same order of appearance and (broadly) similar chemical compositions (Hoover, 1989), so the differences we observe cannot be due to variations in the primocryst assemblage. Because the differences in microstructures are also observed along strike within the Layered Series itself, we can discount as a controlling factor the deposition of non-cotectic proportions of cumulus grains and thus differences in the modal composition of the mush. The remaining factors for controlling the amount, composition and temporal evolution of the interstitial liquid are time-dependent mass-transport processes (i.e. compaction and compositional convection) and the effects of liquid immiscibility.

MASS TRANSPORT IN A SOLIDIFYING MUSH ZONE

Compositional convection in a rigid mush

Gravitational forces acting within a rigid (non-compacting) mush can drive compositional convection of the interstitial liquid. We would expect to see different consequences in vertically oriented layers (i.e. a mush zone growing away from a vertical wall in which gravitationally driven fluid flow will move along layers) compared with horizontally oriented layers (i.e. floor cumulates, in which fluid flow will move across layers), with the greatest geochemical effect observed in the latter.

The thickness of the crystal mush is of critical importance for the onset of convective instabilities, with convection only possible in basaltic mushes exceeding ~200 m (Tait & Jaupart, 1992). This thickness constraint does not pose a problem for convection in a wall mush but any fluid flow will be largely vertical (e.g. Bedard *et al.*, 1992) and thus may have less geochemical consequence here. Assessing the importance of convection within the floor mush is more problematic, as there are widely differing views on the thickness of the mush in mafic intrusions. Arguments based on effective drainage of dense rejected liquids on a sloping chamber floor point towards a thickness of <1 m (Morse, 1988). Models involving compaction result in calculated mush thicknesses of the order of hundreds of metres (Sparks *et al.*, 1985; Tharp *et al.*, 1998), although metre-scale anti-correlations between rock density and the fraction of trapped liquid have been cited as evidence for a thin compacting mush (Tegner *et al.*, 2009). Direct evidence for mush thickness comes from inferences about its mechanical behaviour from considerations of metre-scale disruption of layering caused by fallen blocks (Irvine *et al.*, 1998), although this tells us only that the topmost few metres were relatively weakly consolidated. Holness *et al.* (2007*b*) demonstrated that the changes in dihedral angle (interpreted as a record of time-integrated thermal history) associated with liquidus phase additions do not penetrate more than a few metres into the underlying cumulates in the centre of the floor, again pointing to a thin mush zone.

Given the balance of evidence we favour a model of the chamber floor based on a relatively thin mush zone, and conclude that wholesale compositional convection within the mush itself (involving the fluid as a whole, regardless of whether it was single- or two-phase) is unlikely to have controlled the development of late-stage microstructures. However, it is possible that there was local movement of liquid within the mush, particularly if the chamber floor was sloping. If the liquid is two-phase, gravitational forces within a rigid horizontal mush can separate the conjugate liquids if they have different densities. This could also occur within a vertical sequence (such as the MBS): for most of its vertical extent liquid flowing into a packet of vertical mush will replace that flowing in, but geochemical signatures might be detected in rocks near the intrusion floor (where there is no liquid flowing into the base to replenish that leaving the top) and at its top (i.e. within the MBS near the intrusion roof, where there is no liquid flowing downwards into the top of the layer to replenish that leaving), provided the cooling rate is sufficiently slow.

COMPACTION

The underlying equations for compaction formulated by McKenzie (1984) are consistent with very effective melt extraction from the mantle, but their application to basaltic systems suggests that efficient compaction only occurs when the thickness of the fluid-bearing layer exceeds several hundreds of metres (e.g. Sparks *et al.*, 1985). Evidence for compaction in the Skaergaard intrusion is provided by the anti-correlation between the apparent trapped liquid and bulk-rock density (Tegner *et al.*, 2009), and by the presence of bent plagioclase grains with deformation twins above the lower parts of LZb (where the fraction of trapped liquid starts to decrease; Tegner *et al.*, 2009). However, the direct (but perhaps not conclusive) evidence for a thin mush provided by the fallen blocks (Irvine *et al.*, 1998) and dihedral angles (Holness *et al.*, 2007*b*) suggests that this reduction in apparent trapped liquid was achieved without the thick mush zone advocated by Sparks *et al.* (1985).

We suggest instead that a significant component of the reduction in porosity inferred from bulk geochemistry may have been achieved by increasing the efficiency of packing of (non-deforming) grains in a high-porosity environment close to the magma–mush interface. In the context of a crystallizing intrusion with a convecting bulk liquid above a crystal mush zone, possible mechanisms to increase packing densities and expel interstitial liquid include grain alignment and rearrangement in magmatic currents (see Irvine *et al.*, 1998), and slumping (e.g. Holness & Winpenny, 2009). This is implied by the results of Tegner *et al.* (2009), who suggested that expulsion of interstitial liquid primarily occurred in the upper few metres of the mush zone. Further reduction in apparent trapped liquid could be achieved by localized compositional convection at the magma–mush interface (see Morse, 1988).

Comparison of wall and floor rocks in Skaergaard

The MBS, with its high P_2O_5 content (Hoover, 1989) and orthocumulus nature, formed from a highly porous mushy

layer with a relatively high cooling and solidification rate. It is unlikely to have compacted much. The Layered Series rocks from the centre of the intrusion formed in a thin, slowly cooled, mushy zone (Holness *et al.*, 2007*b*), with a few volume per cent trapped liquid (Tegner *et al.*, 2009); expulsion of residual interstitial liquid was effective. In contrast, the edges of the Layered Series have relatively large volumes of trapped liquid (Tegner *et al.*, 2009); expulsion of residual interstitial liquid was relatively insignificant.

The spatial variation of the extent of expulsion of residual interstitial liquid, as inferred from bulk-rock geochemistry (Fig. 3e), correlates very closely with the spatial variation of the late-stage microstructures—regions with low amounts of trapped liquid (e.g. in the centre of the LS) contain replacive microstructures indicative of a strongly reactive, low-temperature, Fe-rich, Si-poor liquid and the paired, non-reactive, conjugate intergrowths develop late in the stratigraphy, whereas regions of high amounts of trapped liquid (the MBS) develop a sequence of late-stage microstructures consistent with local reaction driven solely by changes in fO_2 and an early appearance of paired, non-reactive, conjugate intergrowths (Fig. 3). The margins of the LS show intermediate behaviour.

The observed association of late-stage microstructures with regions containing low volumes of interstitial liquid can be due to two processes. First, the relative movement of two liquids during compaction, or differential loss of a buoyant immiscible liquid in a rigid mush, could be a primary control on the reactivity of late-stage liquids—both could result in the preferential loss of Si-rich liquid and the retention of a reactive Fe-rich liquid. Conversely, the observed correlation could be primarily caused by the cooling rate: the rapidly cooled marginal rocks cannot lose much interstitial liquid, leaving the two conjugate liquids in the interstitial spaces insufficient time to separate, whereas more slowly cooled rocks in the centre of the intrusion floor have time for immiscible liquids to coarsen and to separate more effectively, leaving behind a reactive Fe-rich residue.

REACTION OWING TO RELATIVE MOVEMENT OF IMMISCIBLE LIQUIDS

Phase equilibria constraints

Many petrologists have argued against a significant petrogenetic role for silicate liquid immiscibility (e.g. Bowen, 1928) on the basis that relative movement (fractionation) of immiscible liquids should have little, if any, effect on the compositions of the crystallization products (although see Philpotts, 1981). However, although both conjugate liquids must be in equilibrium with the crystals, in non-invariant systems with extensive solid solution or peritectic reactions (e.g. Skaergaard, in which the variance of the system was almost certainly ≥ 1), the chemical effects of liquid–liquid fractionation can be profound. During the accumulation of LZc and MZ, crystal growth was mostly sustained by the volumetrically dominant Fe-rich liquid. The role of the Si-rich liquid was limited to buffering the bulk content of silica and alkalis in the magma, and supplying the albite component of plagioclase. However, loss of equilibrium between the two liquids, for example through partial loss of the Si-rich component from the interstices in the mush zone, would have an immediate effect on the mineral compositions: the observed plagioclase evolution towards more anorthitic and Fe-rich compositions (Fig. 13) is consistent with the removal of the Si-rich liquid and crystallization in a system dominated by the Fe-rich melt (see Humphreys, 2011). Partial removal of Si-rich liquid from the mush may have been also responsible for the change in the direction of the olivine–pigeonite peritectic reaction, because of its effect on the silica activity of the residual interstitial liquid (Morse *et al.*, 1980), resulting in the ubiquitous presence of olivine in symplectitic intergrowths, and possibly also the resorption of Ca-poor pyroxene at pyroxene–plagioclase grain boundaries.

A recent review of experimental data on the relative stability of olivine and low-Ca pyroxene in multiply saturated basaltic systems (Veksler, 2009) showed that both minerals are stable in a broad range of liquid compositions. This is possible because alkalis on one hand, and Fe-oxides together with TiO_2 and P_2O_5 on the other, exert strong and opposite effects on the activity coefficient of silica, the key factor of the olivine–pyroxene reaction. The changes in compositions of mutually saturated liquids are illustrated in Fig. 19. In the alkali- and iron-free system CMAS (CaO–MgO–Al_2O_3–SiO_2) the assemblage forsterite + diopside + orthoenstatite + anorthite + liquid ($fo + di + en + an + l$) represents an isobaric invariant equilibrium stable at 1 bar and 1240°C (Longhi, 1987). The liquid (point labeled 'CMAS' in Fig. 19) is slightly quartz-normative and plots close to the diopside–anorthite eutectic. Addition of Na_2O (forming the system CMASN) transforms the phase assemblage into a univariant equilibrium $fo + di + en + plag + l$ (Soulard *et al.*, 1992) with the plagioclase solid solution and liquid compositions varying along a curve directed towards the Ab corner (Fig. 19) and increasing contents of normative Qz. This path of liquid evolution is a model of the Bowen trend of silica and alkali enrichment. The projection in Fig. 19 also shows that the cotectic proportion of plagioclase increases with decreasing An/Ab along the $fo + di + en + plag + l$ univariant curve even faster than along the $di + plag$ cotectic.

In contrast, addition of FeO to CMAS (the system CMASF) shifts the compositions of multiply saturated

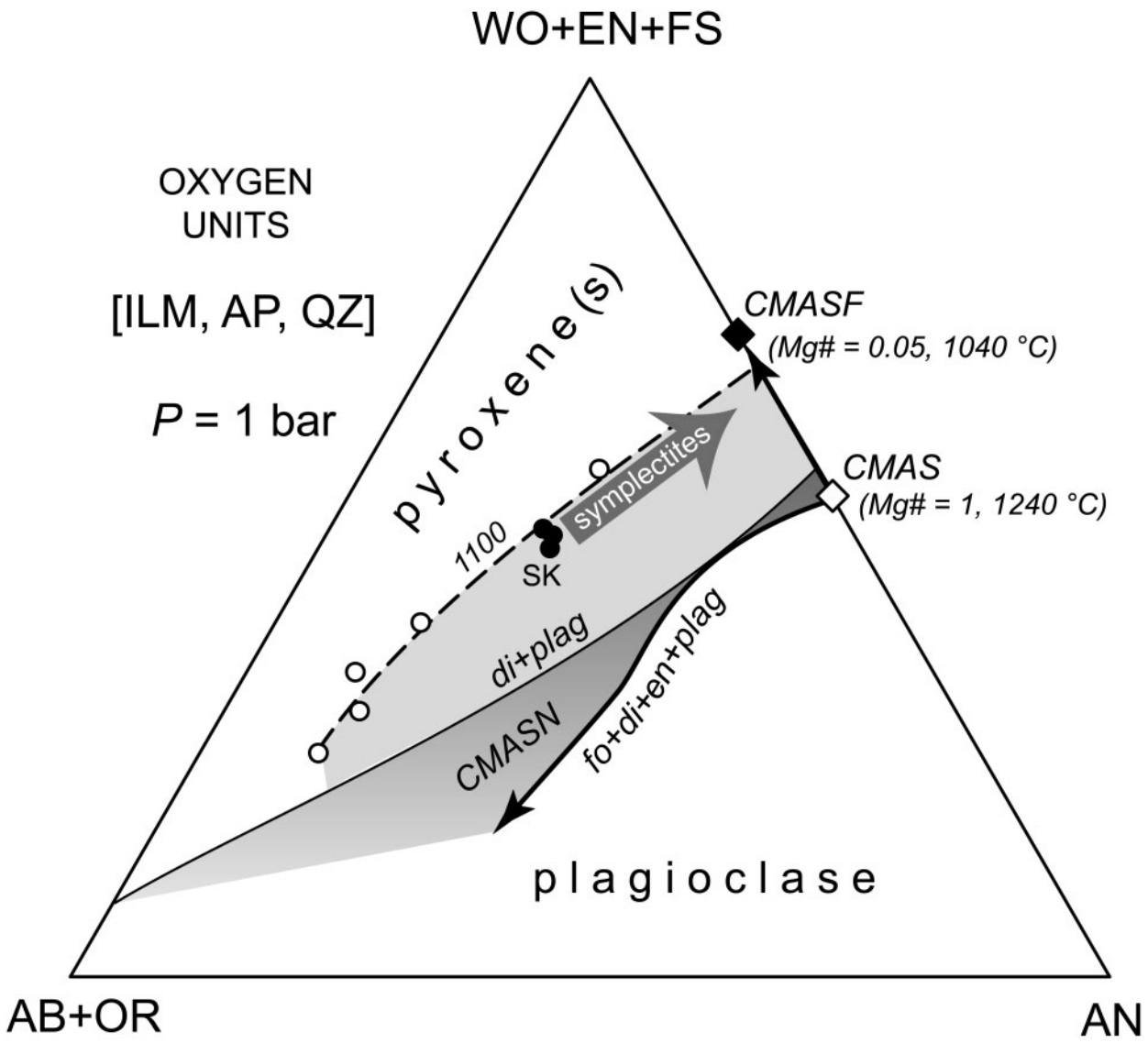

Fig. 19. A pseudo-ternary projection that combines three pyroxene norms $CaSiO_3$ (Wo), $MgSiO_3$ (En) and $FeSiO_3$ (Fs) in one corner, and three plagioclase components $NaAlSi_3O_8$ (Ab), $KAlSi_3O_8$ (Or) and $CaAl_2Si_2O_8$ (An) in the other two corners. In the absence of the Or and Fs components, and by fixing molar Wo/En = 1, the diagram is reduced to the well-known diopside–albite–anorthite ternary featuring a single diopside–plagioclase cotectic (the *di–plag* curve). Other curves, lines and points, with the exception of the cotectic, lie on the quartz-normative side off the projection plane [see Veksler (2009) for a detailed description of the projection method]. Open diamond, CMAS invariant liquid (Longhi, 1987); filled diamond, Fe-rich, silica-saturated liquid (Nielsen *et al.*, 1988); open circles, liquids along the 1100°C isotherm (Shi, 1993); filled circles, Skaergaard liquid compositions (Thy *et al.*, 2006). The position of the fo + di + en + plag + liquid univariant curve (labelled as fo + di + en + plag) of the CMASN system is according to Soulard *et al.* (1992). (See text for further discussion.)

liquids towards higher pyroxene norms. Liquid in equilibrium with olivine, pyroxene, anorthite, ilmenite and tridymite at 1040°C (point 'CMASF' in Fig. 19) has an extreme composition with a SiO_2 content at 44·6 wt % and $FeO_{(tot)}$ at 30 wt % (Nielsen *et al.*, 1988). Thus, multiply saturated liquids in the system CMASF evolve along a perfect Fenner trend of extreme Fe enrichment.

Silica activity in basaltic liquids can be buffered at constant pressure, temperature and fO_2 at the level where olivine and low-Ca pyroxene are both stable if the Mg-number and An/Ab are changed simultaneously and in opposite directions. The compositions of such multiply saturated liquids vary broadly, as demonstrated in Fig. 19 by a series of liquids along the 1100°C isotherm equilibrated with olivine, low- and high-Ca pyroxenes, and plagioclase (Shi, 1993). Skaergaard experimental liquids (three points labelled 'SK' in Fig. 19) equilibrated with the same mineral assemblage plus ilmenite and magnetite at

1089°C (Thy *et al.*, 2006) plot very close to the 1100°C isotherm. The evolution of the liquid in the mush, as implied by the mineralogy and geochemistry of replacive symplectites, is shown by the grey arrow: it follows a trend towards FeO enrichment with alkali depletion. Fe enrichment (decreasing Mg-number at a constant temperature) can be explained by partial resorption of cumulus Fe–Ti oxides; however, net losses of alkalis from symplectitic plagioclase and the inter-cumulus liquid cannot be explained by mineral–melt reactions. Therefore, we propose that the local depletion of the mush system in alkalis was due to the movement of Si-rich immiscible liquid in the gravity field.

Geochemical constraints

There is neither grain-scale evidence for Si–alkali metasomatism nor accumulation of granophyric material in the regions of the intrusion where replacive symplectites are particularly abundant. This might suggest that the Si-rich liquid of the conjugate pair has not accumulated within the crystal mush but has been lost to the bulk liquid. More information on the fate of the Si-rich liquid may potentially be gained from examination of trace element compositional data.

Loss of interstitial liquid will affect the bulk-rock concentrations of elements that were incompatible at the time of liquid expulsion (Meurer & Boudreau, 1998). Tegner *et al.* (2009) presented bulk-rock P, Rb and U concentrations for a 'reference profile' composed of average gabbros through the Skaergaard Layered Series; the concentrations of these three elements are broadly linearly correlated. A linear correlation implies that any loss of interstitial liquid must have occurred before any of the three elements became compatible; that is, before the crystallization of interstitial apatite (P, U), biotite (Rb), K-feldspar (Rb) and zircon (U).

P, U and Rb will be partitioned between the Fe-rich and Si-rich conjugate liquids, with the Fe-rich liquid containing more P and U, but less K and Rb than the corresponding Si-rich liquid (Hess & Rutherford, 1975; Watson 1976; Ryerson & Hess, 1978; Shearer *et al.*, 2001; Veksler *et al.*, 2007). Differential loss of the Si-rich component before the crystallization of biotite or K-feldspar should therefore result in faster reduction of Rb compared with P and U. The correlation between P, U and Rb presented by Tegner *et al.* (2009) is consistent with little differential loss of the Si-component from the mush. However, there is considerable scatter in the relative proportions of the trace elements (Tegner *et al.*, 2009) and, given the uncertainties about effective distribution coefficients for conjugate immiscible liquids, it is not possible to constrain the extent of any differential loss. However, regardless of the proportions of Si-rich liquid lost from the mush (which will have an impact on the liquid line of descent of the bulk magma) we suggest that relative movement of the two immiscible liquids primarily within the mush itself will result in reactive symplectite growth.

Both immiscible liquids must be in chemical equilibrium with plagioclase, olivine, pyroxenes and Fe–Ti oxides, though they may have different partition coefficients and may crystallize different modal proportions of the minerals. However, the compositions of those phases may evolve along divergent paths in spatially separated liquids that are not in equilibrium with each other. In particular, the plagioclase in equilibrium with an Fe-rich liquid should become more anorthitic, and olivine more fayalitic, than that in equilibrium with a Si-rich liquid or with unseparated liquid mixtures. Removal of some or all of the Si-rich conjugate liquid will therefore result in reactions between the remaining Fe-rich liquid and the surrounding primocrysts, and mineral zoning. This is consistent with our observations: plagioclase in replacive symplectites is Fe-rich and up to 50 mol % more anorthitic than adjacent plagioclase primocrysts (Fig. 13), requiring the removal of alkalis and addition of Fe; the abundance of olivine-dominated symplectites in MZ gabbros (despite the general absence of olivine primocrysts) is consistent with a reactive liquid that has a Si- and alkali-poor and Fe-rich bulk composition.

The Fe content and X_{An} of plagioclase increase with fO_2 (Phinney, 1992; Tegner, 1997; Wilke & Behrens, 1999; Sugawara, 2001). However, this effect is very small at oxygen fugacities near FMQ (Phinney, 1992). Fe partitioning into plagioclase also depends on anorthite content because of the greater availability of Ca^{2+} and Al^{3+} sites for substitution of Fe^{2+} and Fe^{3+} respectively (Bindeman *et al.*, 1998; Bedard, 2006). However, the FeO content of plagioclase in symplectites (up to 1·4 wt % FeO) is too great to be explained by the relatively small difference in X_{An} between the symplectitic and primocryst plagioclase. Even in the most primitive plagioclase primocrysts from HZ, which have compositions up to An_{70}, FeO contents typically do not exceed ~0·5–0·6 wt % (Humphreys, 2009). We therefore conclude that the liquid triggering symplectite growth was enriched in Fe. The reduction in Fe content with growth along symplectitic lamellae is accompanied by a decrease in X_{An} (Fig. 14); that is, the symplectite minerals evolve towards the composition of the adjacent plagioclase primocryst as they replace it.

The average Mg-number of replacive symplectite olivine, orthopyroxene and clinopyroxene is approximately the same as that of adjacent primocrysts (Figs 15, 17 and 18), but the concentrations of incompatible elements (MnO, TiO_2, Na_2O and Al_2O_3) are lower (Figs 15, 17 and 18, and Supplementary Datasets 2–4). These compositions are consistent with the outermost margins of pyroxene oikocrysts (Claeson *et al.*, 2007; Humphreys, 2009) and therefore suggest an evolved, ilmenite fractionating, late-stage liquid. Although it seems likely that the

major-element compositions have been affected by diffusion to some extent, Ti and Al diffusion in pyroxene is very slow (e.g. Anovitz, 1991), so the trend towards more evolved compositions of symplectitic olivine and pyroxene along the growth direction is probably relatively unmodified: the similarity of Mg-number is probably linked to the availability of these components in the liquid.

These observations are consistent with the reactive microstructures forming in response to separation of the conjugate liquids: the interstitial liquid near the base of the mush would be dominated by dense Fe-rich liquid rich in Mg, Ca and P as well as Fe, and depleted in Si, Al and Na (Hess & Rutherford, 1974; Watson, 1976; Veksler *et al.*, 2006, 2007). This low-volume residual liquid would react with adjacent primocrysts to form olivine, Fe–Ti oxides, Ca-rich clinopyroxene and Ca- and Al-rich plagioclase (e.g. Loferski & Arculus, 1993; Veksler *et al.*, 2007). The liquid in the upper reaches of the mush is probably hotter (by perhaps a few degrees) and the width of the liquid miscibility gap is smaller, compared with that at the base of the mush (although see Boorman *et al.*, 2004). Some of the Si-rich liquid expelled from the base will therefore dissolve as it moves upwards, but there should be little evidence of reaction between this anomalously Si-rich melt and the crystals actively growing within the mush, because the volume proportion of added liquid is small.

We would anticipate that this redistribution of liquid would generate some differences in incompatible element ratios (see Tegner *et al.*, 2009). We suggest that the apparent linear correlations of incompatible elements observed by Tegner *et al.* (2009) result primarily from their analysis of 'average gabbro' samples, and that redistribution of liquid may have the potential to generate modal layering. For example, following the formation of a relatively impermeable horizon within the mush, a relatively Fe-rich layer will crystallize near the base of the mush whereas a comparatively more felsic layer will form underneath the permeability barrier. The intermediate zone between the two would have relatively normal interstitial liquid compositions and results in 'average gabbro' and thus 'normal' incompatible element ratios. We might therefore expect to see changes in incompatible element ratios between mafic–felsic modal layer pairs. This prediction is consistent with the observations of Vincent & Phillips (1954), who reported higher ulvöspinel contents (i.e. more Ti and/or more reducing conditions) in the oxide-rich parts of the Skaergaard gabbros.

We have suggested that the poly-crystalline olivine rims result from decreasing fO_2 in the interstitial liquid. Although the fO_2 of each of the immiscible liquids is unknown, we can obtain some insight into their relative oxidation states from the minerals that crystallize from the liquids both in the interstitial pockets and in the melt inclusions reported by Jakobsen *et al.* (2005). The Fe-rich liquid typically crystallizes ilmenite ($Fe^{2+}TiO_3$), pyroxene or olivine (mainly Fe^{2+}), biotite ($K(Mg, Fe^{2+})_3[AlSi_3O_{10}](OH,F)_2$), and minor magnetite ($Fe^{3+}Fe^{2+}_2O_4$) as well as apatite and plagioclase; the Si-rich pockets typically contain quartz, feldspar, and minor magnetite ($Fe^{3+}Fe^{2+}_2O_4$) but no ilmenite. We therefore infer that the Fe-rich liquid has a higher FeO/Fe_2O_3 than the silicic liquid. Therefore, interaction of primocrysts with the Fe-rich liquid should result in strong compositional changes to more Ca-rich, Fe-rich compositions, as well as the formation of poly-crystalline olivine rims as a result of decreasing fO_2. This close spatial association of replacive symplectites and poly-crystalline olivine rims is exactly what is observed in LZc and MZ.

In contrast, the earlier arrival in the stratigraphy of fish-hook pyroxenes and stepped grain boundaries suggests that these other microstructures resulted from relatively insignificant liquid phase separation. The Type 2 symplectites probably also represent an early stage of this process. They occur in the most primitive rocks where the interstitial liquid would have intersected the miscibility gap very late in the solidification. Only small amounts of Na were lost from the base of the mush. The presence of Type 2 symplectites in the basal MBS probably reflects the absence of Si-rich liquid flowing up from below, thus preventing continual replenishment and maintenance of the original bulk liquid composition. The presence of stepped grain boundaries at all stratigraphic levels of the MBS indicates at least some liquid phase separation within the central parts of the wall mush. Their confinement to the central parts of the MBS points to a fine balance between cooling rate and the time necessary for separation of the emulsion.

IMMISCIBLE LIQUIDS IN THE SKAERGAARD MUSH ZONE

The topology and spatial distribution of a pair of conjugate immiscible liquids depends on their wetting properties, their volume fractions and the energy of the interface separating the two liquids. In fractionating liquids analogous to the Skaergaard bulk magma, the miscibility gap is intersected on the Fe-rich side, with the Si-rich liquid initially forming the minor, dispersed phase (Veksler, 2009). Little is known about wetting properties for silicate melts on phases of geological interest, although it is probable that melts preferentially wet surfaces with similar compositions (Philpotts, 1979). The Fe-rich liquid may preferentially wet apatite (Jakobsen *et al.*, 2005), olivine and pyroxene (Philpotts, 1979) consistent with the general confinement of the Skaergaard ilmenite-rich intergrowths to regions rich in oxides, pyroxene and olivine (Figs 10f and 11). Granophyric pockets occur almost exclusively within

plagioclase-bounded pockets (Fig. 10), consistent with the Si-rich conjugate liquid preferentially wetting plagioclase. The concentration of replacive symplectites around Fe–Ti oxide primocrysts can also be explained as a consequence of the preferential wetting of this phase by an Fe-rich liquid.

The energy of the interface between the two liquids is low (Veksler *et al.*, 2010). This means that there is little driving force acting to coarsen droplets of the dispersed phase and, for any given volume fraction of the dispersed phase, the droplet size will increase only slowly with time. Droplet coarsening will occur primarily by coalescence, so in general will correlate with the volume fraction of the dispersed phase. At the onset of immiscibility, the interstitial spaces will therefore be filled with a low-viscosity, high-density, wetting Fe-rich liquid containing relatively rigid, small, droplets of viscous, lower density, Si-rich liquid. The bulk composition of the liquid becomes more silicic with continued fractionation, so the volumetric importance of the Si-rich component and droplet size increase, both within the mush and with stratigraphic height. This may be accelerated by a proportion of the Si-rich liquid being returned to the main magma through the mush, and contribute to the evolution of the liquid line of descent.

The loss of the reactive microstructures and the appearance of paired intergrowths across the stratigraphy in MZ and UZa are most probably linked to the gradual increase in the volumetric proportion of the Si-rich droplets. Increasing fractionation of the bulk magma increases the volume fraction of Si-rich droplets or globules in the liquid emulsion at the moment of incorporation into the mush. The efficiency of movement of the Si-rich droplets within the mush will decrease as the globules become too big to pass through pore throats (Chung & Mungall, 2009). At some point there will be no efficient relative movement in the mush zone: this point is reached later in strongly compacting parts compared with the weakly compacting ones because the pressure driving porous flow can force droplets through pores by deforming them (Chung & Mungall, 2009). Efficient relative movement may also be easier to achieve in the slowest cooling parts of the intrusion, although slower cooling would also promote droplet coarsening. Either of these effects, acting alone or in tandem, will result in the observed variations in stratigraphic height of the disappearance of the reactive symplectites and their replacement by the paired association of granophyre and ilmenite-rich intergrowths.

THE UPPER BORDER ZONE

Examination of a limited collection of samples from the UBS suggests that it contains no reactive microstructures, but contains an anomalously high proportion of granophyric material compared with equivalent horizons in the LS, as suggested by its commonly quartz-normative compositions (e.g. Nielsen, 2004; Nielsen *et al.*, 2009). The generally more felsic bulk composition of the UBS has been variously attributed to (1) the instability of Fe-rich interstitial liquids and crystals that may have descended into the main magma reservoir (Brandeis & Jaupart, 1987) and (2) addition of felsic components (McBirney, 1996*a*), missing from the Layered Series because of compositional convection (Morse, 2008*b*) or rise of low-density Si-rich immiscible liquids (Veksler *et al.*, 2007, 2008, 2010).

According to our model, the absence of replacive symplectites in the UBS points to the absence of relative movement of the two conjugate immiscible liquids. This is likely to have been primarily the result of limited liquid phase separation in an essentially rigid crystal matrix. Si-rich droplets rising through the UBS under the influence of buoyancy forces will encounter rapidly decreasing porosity and permeability as they enter more crystalline parts of the mush. The amount of liquid phase separation will therefore be limited compared with the Layered Series. An alternative explanation is that, because of addition of felsic components the UBS interstitial liquid may have approached the miscibility gap with a dominant silicic component, so that when unmixing started it was characterized by the nucleation of Fe-rich droplets within a highly viscous silicic liquid, thus prohibiting liquid–liquid phase separation.

CONCLUSIONS

The texture, chemistry and spatial distribution of late-stage microstructures developed during the last stages of solidification of the Skaergaard intrusion can be used to track silicate liquid immiscibility in the interstitial liquid of the crystal mush. In the upper parts of the stratigraphy, paired granophyre- and ilmenite-rich, planar-sided intergrowths reflect *in situ* crystallization of Fe-rich and Si-rich immiscible silicate liquids. We suggest that the first appearance of these non-reactive microstructures in MZ* (in the more rapidly cooled MBS) represents the onset of immiscibility in the bulk Skaergaard magma at MZ times. In the lowermost parts of the stratigraphy, oxy-symplectites form as a result of localized increases in fO_2 of the interstitial liquid following oxide crystallization. The reverse reaction leads to the formation of olivine rims higher in the stratigraphy, indicating later decreases in liquid fO_2. In the LS, olivine rims are abundant within LZc and MZ, and are closely associated with the formation of replacive symplectites involving An-rich plagioclase and Fe-rich olivine.

The microstructures display systematic spatial variations, with those in the vertical walls consistent with localized reaction with late-stage liquids, predominantly via redox reactions, and those in the more slowly cooled, and/or more strongly compacted, cumulates of the chamber floor containing microstructures indicative of a strongly

reactive Fe-rich interstitial liquid. We interpret its reactivity to be due to the partial removal of exsolved Si-rich droplets, causing the remaining liquid to react with the primocrysts near the base of the mush. Bulk-rock element data are consistent with little or no preferential loss of the Si-rich liquid from the mush.

ACKNOWLEDGEMENTS

We are grateful to Dieter Rhede, Chris Hayward and Chiara Petrone for assistance with electron microprobe analysis. We are particularly indebted to Morris Beattie of Galahad Gold for his help and co-operation, including provision of logistical support in the field. We are grateful to Alan Boudreau, Grant Cawthorn and Tony Philpotts for generous reviews that helped clarify our arguments.

FUNDING

G.R.S. acknowledges the receipt of a NERC CASE studentship that was partially supported by Galahad Gold plc. Analytical work was partially supported by NERC grant NE/F020325/1. M.C.S.H. was supported by a Junior Research Fellowship from Trinity College, Cambridge and by NERC grant NE/F020325/1. I.V.V. has been supported by the DFG grant FR 557/23-1. Access to drill cores housed in the Geological Museum (Copenhagen) was made possible by grants from The Danish Council for Independent Research, Natural Sciences (FNU) to T.F.D. N.

SUPPLEMENTARY DATA

Supplementary data for this paper are available at *Journal of Petrology* online.

REFERENCES

Ambler, E. P. & Ashley, P. M. (1997). Vermicular orthopyroxene–magnetite symplectites from the Wateranga layered mafic intrusion, Queensland, Australia. *Lithos* **10**, 163–172.

Andersen, D. J., Lindsley, D. H. & Davidson, P. M. (1993). QUILF: A Pascal program to assess equilibria among Fe–Mg–Mn–Ti oxides, pyroxenes, olivine, and quartz. *Computers and Geosciences* **19**, 1333–1350.

Anovitz, L. M. (1991). Al zoning in pyroxene and plagioclase: Window on late prograde to early retrograde P–T paths in granulite terranes. *American Mineralogist* **76**, 1328–1343.

Ashworth, J. R. & Chambers, A. D. (2000). Symplectic reaction in olivine and the controls of intergrowth spacing in symplectites. *Journal of Petrology* **41**, 285–304.

Barton, M. & van Gaans, C. (1988). Formation of orthopyroxene–Fe–Ti oxide symplectites in Precambridge intrusives, Rogaland, southwestern Norway. *American Mineralogist* **73**, 1046–1059.

Barton, M., Sheets, J. M., Lee, W. E. & van Gaans, C. (1991). Occurrence of low-Ca pyroxene and the role of deformation in the formation of pyroxene–Fe–Ti-oxide symplectites. *Contributions to Mineraology and Petrology* **108**, 181–195.

Batiza, R. & Vanko, D. A. (1985). Petrologic evolution of large failed rifts in the Eastern Pacific: Petrology of volcanic and plutonic rocks from the Mathematician Ridge area and the Guadalupe Trough. *Journal of Petrology* **26**, 564–602.

Bedard, J. H. (2006). Trace element partitioning in plagioclase feldspar. *Geochimica et Cosmochimica Acta* **70**, 3717–3742.

Bedard, J. H., Kerr, R. C. & Hallworth, M. A. (1992). Porous sidewall and sloping floor crystallization experiments using a reactive mush: Implications for the self-channelization of residual melts in cumulates. *Earth and Planetary Science Letters* **111**, 319–329.

Bindeman, I. N., Davis, A. M. & Drake, M. J. (1998). Ion microprobe study of plagiocase–basalt partition experiments at natrual concentration levels of trace elements. *Geochimica et Cosmochimica Acta* **62**, 1175–1193.

Bird, D. K., Brooks, C. K., Gannicott, R. A. & Turner, P. A. (1991). A gold-bearing horizon in the Skaergaard intrusion, East Greenland. *Economic Geology* **86**, 1083–1092.

Bollingberg, K. (1995). Textural and chemical evolution of the Fe–Ti oxide minerals during the late- and post-magmatic cooling of the Skærgaard intrusion, East Greenland. PhD thesis, University of Copenhagen.

Boorman, S., Boudreau, A. & Kruger, F. J. (2004). The Lower Zone–Critical Zone transition of the Bushveld Complex: A quantitative textural study. *Journal of Petrology* **45**, 1209–1235.

Bowen, N. L. (1928). *The Evolution of the Igneous Rocks*. Princeton, NJ: Princeton University Press.

Bown, M. G. & Gay, P. (1960). An X-ray study of exsolution phenomena in the Skaergaard pyroxenes. *Mineralogical Magazine* **32**, 379–388.

Brandeis, G. & Jaupart, C. (1987). The kinetics of nucleation and crystal growth and scaling laws for magmatic crystallisation. *Contributions to Mineralogy and Petrology* **96**, 24–34.

Brooks, C. K. & Nielsen, T. F. D. (1978). Early stages in the differentiation of the Skaergaard magma as revealed by a closely related suite of dyke rocks. *Lithos* **11**, 1–14.

Brooks, C. K. & Nielsen, T. F. D. (1982). The East Greenland continental margin: A transition between oceanic and continental magmatism. *Journal of the Geological Society, London* **139**, 265–275.

Brown, G. M. (1957). Pyroxenes from the early and middle stages and fractionation of the Skaergaard Intrusion, East Greenland. *Mineralogical Magazine* **31**, 511–543.

Brown, G. M. & Peckett, A. (1977). Fluorapatites from the Skaergaard Intrusion, East Greenland. *Mineralogical Magazine* **41**, 227–232.

Carstens, H. (1957). Investigations of titaniferous iron ore deposits. Part I. Gabbros and associated titaniferous iron ore in the west-Norwegian gneisses. *Kongelige Norske Videnskabers Selskab Skrifter* **1957-3**, 1–67.

Champness, P. E. & Copley, P. A. (1976). The transformation of pigeonite to orthopyroxene. In: Wenk, H.-R. (ed.) *Electron Microscopy in Mineralogy*. Berlin: Springer, pp. 228–233.

Chung, H. Y. & Mungall, J. E. (2009). Physical constraints on the migration of immiscible fluids through partially molten silicates, with special reference to magmatic sulfide ores. *Earth and Planetary Science Letters* **286**, 14–22.

Claeson, D. T., Meurer, W. P., Hogmalm, K. J. & Larson, S. A. (2007). Using LA-ICPMS mapping and sector zonation to understand growth and trace-element partitioning in sector-zoned clinopyroxene oikocrysts from the Norra Ulvo gabbro, Sweden. *Journal of Petrology* **48**, 711–728.

Copley, P. A. & Champness, P. E. (1975). The transformation of pigeonite to orthopyroxene. In: Venables, J. A. (ed.) *Developments in Electron Microscopy and Analysis*. London: Academic Press, pp. 475–476.

Copley, P. A., Champness, P. E. & Lorimer, G. W. (1974). Electron petrography of exsolution textures in an iron-rich clinopyroxene. *Journal of Petrology* **15**, 41–57.

De Haas, G. J. L., Nijland, T. G., Valbracht, P. J., Maijer, C., Verschure, R. & Andersen, T. (2002). Magmatic versus metamorphic origin of olivine–plagioclase coronas. *Contributions to Mineralogy and Petrology* **143**, 537–550.

Douglas, J. A. V. (1961). A further petrological and chemical investigation of the Upper Part of the Skaergaard Intrusion, East Greenland. PhD thesis, University of Oxford.

Fenner, C. N. (1929). The crystallisation of basalts. *American Journal of Science* **18**, 225–253.

Goode, A. D. T. (1974). Oxidation of natural olivines. *Nature* **248**, 500–501.

Haselton, J. D. & Nash, W. P. (1975). Ilmenite–orthopyroxene intergrowths from the Moon and the Skaergaard Intrusion. *Earth and Planetary Science Letters* **26**, 287–291.

Hess, P. C. & Rutherford, M. J. (1974). Element fractionation between immiscible melts. *Abstracts of the Lunar and Planetary Science Conference* **5**, 328–330.

Hirschmann, M. M. (1992). Origin of transgressive granophyre from the layered series of the Skaergaard intrusion, East Greenland. *Journal of Volcanology and Geothermal Research* **52**, 185–207.

Holness, M. B. (2005). Spatial constraints on magma chamber replenishment events from textural observations of cumulates: the Rum Layered Intrusion, Scotland. *Journal of Petrology* **46**, 1585–1601.

Holness, M. B. (2007). Textural immaturity of cumulates as an indicator of magma chamber processes: infiltration and crystal accumulation in the Rum Layered Suite. *Journal of the Geological Society, London* **164**, 529–539.

Holness, M. B. & Winpenny, B. (2009). The Unit 12 allivalite, Eastern Layered Intrusion, Isle of Rum: a textural and geochemical study of an open-system magma chamber. *Geological Magazine* **146**, 437–450.

Holness, M. B., Anderson, A. T., Martin, V. M., Maclennan, J., Passmore, E. & Schwindinger, K. (2007*a*). Textures in partially solidified crystalline nodules: A window into the pore structure of slowly cooled mafic intrusions. *Journal of Petrology* **48**, 791–800.

Holness, M. B., Tegner, C., Nielsen, T. F. N., Stripp, G. R. & Morse, S. A. (2007*b*). A textural record of solidification and cooling in the Skaergaard intrusion, East Greenland. *Journal of Petrology* **48**, 2359–2377.

Hoover, J. D. (1989). Petrology of the Marginal Border Series of the Skaergaard intrusion. *Journal of Petrology* **30**, 399–439.

Humphreys, M. C. S. (2009). Chemical evolution of intercumulus liquid, as recorded in plagioclase overgrowth rims from the Skaergaard Intrusion. *Journal of Petrology* **50**, 127–145.

Humphreys, M. C. S. (2011). Silicate liquid immiscibility within the crystal mush: Evidence from Ti in plagioclase from the Skaergaard Intrusion. *Journal of Petrology* (in press).

Hunter, R. H. & Sparks, R. S. J. (1987). The differentiation of the Skaergaard intrusion. *Contributions to Mineralogy and Petrology* **95**, 451–461.

Hunter, R. H. & Sparks, R. S. J. (1990). The differentiation of the Skaergaard intrusion. Reply to McBirney, A. R., and Naslund, H. R. *Contributions to Mineralogy and Petrology* **104**, 248–254.

Irvine, T. N., Andersen, J. C. Ø. & Brooks, C. K. (1998). Included blocks (and blocks within blocks) in the Skaergaard intrusion: geological relations and the origins of rhythmic modally graded layers. *Geological Society of America Bulletin* **110**, 1398–1447.

Jakobsen, J. K., Veksler, I. V., Tegner, C. & Brooks, C. K. (2005). Immiscible iron- and silica-rich melts in basalt petrogenesis documented in the Skaergaard intrusion. *Geology* **33**, 885–888.

Jakobsen, J. K., Veksler, I. V., Tegner, C., Lesher, C. E., Thy, P. & Brooks, C. K. (2006). Evidence for early liquid immiscibility in the Skaergaard intrusion, East Greenland. *Goldschmidt Conference Abstracts 2006*, A288.

Jang, D. J., Naslund, H. R. & McBirney, A. R. (2001). The differentiation trend of the Skaergaard intrusion and the timing of magnetite crystallisation: Fe enrichment revisited. *Earth and Planetary Science Letters* **189**, 189–196.

Johnston, D. A. & Stout, J. H. (1984). Development of orthopyroxene–Fe/Mg ferrite symplectites by continuous olivine oxidation. *Contributions to Mineralogy and Petrology* **88**, 196–202.

Koepke, J., Feig, S. T. & Snow, J. (2005*a*). Late-stage magmatic evolution of oceanic gabbros as a result of hydrous partial melting: Evidence from the ODP Leg 153 drilling at the Mid-Atlantic Ridge. *Geochemistry, Geophysics, Geosystems* **6**, 1–27.

Koepke, J., Feig, S. T. & Snow, J. (2005*b*). Hydrous partial melting in the lower oceanic crust. *Terra Nova* **17**, 286–291.

Koepke, J., Berndt, J., Feig, S. T. & Holtz, F. (2007). The formation of SiO_2-rich melts within the deep oceanic crust by hydrous partial melting of gabbros. *Contributions to Mineralogy and Petrology* **153**, 67–84.

Larsen, L. M., Watt, W. S. & Watt, M. (1989). Geology and petrology of the Lower Tertiary plateau basalts of the Scoresby Sund region, East Greenland. *Bulletin of Grønlands Geologiske Undersøgelse* **157**, 164.

Larsen, R. B. & Brooks, C. K. (1994). Origin and evolution of gabbroic pegmatites in the Skaergaard intrusion, East Greenland. *Journal of Petrology* **35**, 1651–1679.

Larsen, R. B. & Tegner, C. (2006). Pressure conditions for the solidification of the Skaergaard intrusion: eruption of East Green land flood basalts in less than 300,000 years. *Lithos* **92**, 181–197.

Lindsley, D. H., Brown, G. M. & Muir, I. D. (1969). Conditions of ferrowollastonite–ferrohedenbergite inversion in the Skaergaard intrusion, East Greenland. *Mineralogical Society of America, Special Paper* 2, 193–201.

Loferski, P. J. & Arculus, R. J. (1993). Multiphase inclusions in plagioclase from anorthosites in the Stillwater Complex, Montana: implications for the origin of anorthosites. *Contributions to Mineralogy and Petrology* **114**, 63–78.

Longhi, J. (1987). Liquidus equilibria and solid solution in the system $CaAl_2Si_2O_8$–Mg_2SiO_4–$CaSiO_3$–SiO_2 at low pressure. *American Journal of Science* **287**, 265–331.

Maaløe, S. (1978). The origin of rhythmic layering. *Mineralogical Magazine* **42**, 337–345.

Manning, C. E. & Bird, D. K. (1986). Hydrothermal clinopyroxenes of the Skaergaard intrusion. *Contributions to Mineralogy and Petrology* **92**, 437–447.

McBirney, A. R. (1975). Differentiation of the Skaergaard intrusion. *Nature* **253**, 691–694.

McBirney, A. R. (1989). The Skaergaard Layered Series, I: Structure and average compositions. *Journal of Petrology* **30**, 363–397.

McBirney, A. R. (1996*a*). The Skaergaard intrusion. In: Cawthorn, R. G. (eds) *Layered Intrusions*. Amsterdam: Elsevier, pp. 147–180.

McBirney, A. R. (1996*b*). Geological map of the Skaergaard intrusion, East Greenland, 1:20,000. Department of Geology, University of Oregon, Eugene.

McBirney, A. R. (2002). The Skaergaard Layered Series. Part VI. Excluded trace elements. *Journal of Petrology* **43**, 535–556.

McBirney, A. R. (2008). Comments on: Liquid immiscibility and the evolution of basaltic magma. *Journal of Petrology* **49**, 2169–2170.

McBirney, A. R. & Nakamura, Y. (1974). Immiscibility in late-stage magmas of the Skaergaard intrusion. *Carnegie Institution of Washington Yearbook* **73**, 348–352.

McBirney, A. R. & Nasland, H. R. (1990). The differentiation of the Skaergaard intrusion. A discussion of R. H. Hunter and R. S. J. Sparks. *Contributions to Mineralogy and Petrology* **104**, 235–240.

McBirney, A. R. & Sonnenthal, E. R. (1990). Metasomatic replacement in the Skaergaard intrusion, East Greenland: preliminary observations. *Chemical Geology* **88**, 245–260.

McKenzie, D. (1984). The generation and compaction of partially molten rock. *Journal of Petrology* **25**, 713–765.

Meurer, W. P. & Boudreau, A. E. (1998). Compaction of igneous cumulates. Part I. Whole-rock compositions as an indicator of the trapped liquid proportions in the Stillwater complex, Montana. *Journal of Geology* **106**, 281–292.

Morse, S. A. (1988). Motion of crystals, solute and heat in layered intrusions. *Canadian Mineralogist* **26**, 209–224.

Morse, S. A. (1990). A discussion of Hunter and Sparks (*Contributions to Mineralogy and Petrology*, 95, 451–461). *Contributions to Mineralogy and Petrology* 104, 240–251.

Morse, S. A. (2008*a*). Towards a thermal model for the Skaergaard liquidus. *American Mineralogist* **93**, 248–251.

Morse, S. A. (2008*b*). Compositional convection trumps silicate liquid immiscibility in layered intrusions: A discussion of 'Liquid immiscibility and the evolution of basaltic magma' by Veksler *et al.*, *Journal of Petrology*, **48**, 2187–2210. *Journal of Petrology* **49**, 2157–2168.

Morse, S. A. & Nolan, K. M. (1984). Origin of strongly reversed rims on plagioclase in cumulates. *Earth and Planetary Science Letters* **68**, 485–498.

Morse, S. A., Lindsley, D. H. & William, R. J. (1980). Concerning intensive parameters in the Skaergaard Intrusion. *American Journal of Science* **280**, 159–170.

Moseley, D. (1984). Symplectic exsolution in olivine. *American Mineralogist* **69**, 139–153.

Muir, I. D., Tilley, C. E. & Scoon, J. H. (1957). Contribution to the petrology of Hawaiian basalts. I. The picritic basalts of Kilauea. *American Journal of Science* **255**, 241–253.

Naslund, H. R. (1984). Petrology of the Upper Border Series of the Skaergaard intrusion. *Journal of Petrology* **25**, 185–212.

Nielsen, R. L., Davidson, P. M. & Grove, T. L. (1988). Pyroxene–melt equilibria: an updated model. *Contributions to Mineralogy and Petrology* **100**, 361–373.

Nielsen, T. F. D. (2004). The shape and volume of the Skaergaard Intrusion, East Greenland: Implications for mass balance and bulk composition. *Journal of Petrology* **45**, 507–530.

Nielsen, T. F. D., Olsen, S. D. & Stensgaard, B. M. (2009). Developing a 3-D model for the Skaergaard intrusion in East Greenland: Constraints on structure, mineralisation and petrogenetic models. *Geological Survey of Denmark and Greenland Bulletin* **17**, 61–64.

Philpotts, A. R. (1979). Silicate liquid immiscibility in tholeiitic basalts. *Journal of Petrology* **20**, 99–118.

Philpotts, A. R. (1981). A model for the generation of massif-type anorthosites. *Canadian Mineralogist* **19**, 233–253.

Philpotts, A. R. (2008). Comments on: Liquid immiscibility and the evolution of basaltic magma. *Journal of Petrology* **49**, 2171–2175.

Philpotts, A. R. & Doyle, C. D. (1983). Effect of magma oxidation state on the extent of silicate liquid immiscibility in a tholeiitic basalt. *American Journal of Science* **283**, 967–986.

Phinney, W. C. (1992). Partition coefficients for iron between plagioclase and basalt as a function of oxygen fugacity—implications for Archean and lunar anorthosites. *Geochimica et Cosmochimica Acta* **56**, 1885–1895.

Pouchou, J. L. & Pichoir, F. (1985). 'PAP' (φ–ρ–Z) procedure for improved quantitative microanalysis. In: Armstrong, J. T. (ed.) *Microbeam Analysis*. San Francisco, CA: San Francisco Press, pp. 104–106.

Roelofse, F., Ashwal, L. D., Pineda-Vargas, C. A. & Przybylowicz, W. J. (2009). Enigmatic textures developed along plagioclase–augite grain boundaries at the base of the Main Zone, Northern Limb, Bushveld Complex—evidence for late stage melt infiltration into a nearly solidified crystal mush. *South African Journal of Geology* **112**, 39–46.

Ryerson, F. J. & Hess, P. C. (1978). Implications of liquid–liquid distribution coefficients to mineral–liquid partitioning. *Geochimica et Cosmochimica Acta* **42**, 921–932.

Seyler, M., Lorand, J. P., Dick, H. J. B. & Drouin, M. (2007). Pervasive melt percolation reactions in ultra-depleted refractory harzburgites at the Mid-Atlantic Ridge, 15°20′N: ODP Hole 1274A. *Contributions to Mineralogy and Petrology* **153**, 303–319.

Shaw, C. S. J. (1999). Dissolution of orthopyroxene in basanitic magma between 0·4 and 2 GPa: further implications for the origin of Si-rich alkaline glass inclusions in mantle xenoliths. *Contributions to Mineralogy and Petrology* **135**, 114–132.

Shearer, C. K., Papike, J. J. & Spilde, M. N. (2001). Trace element partitioning between immiscible lunar melts: an example from naturally occurring lunar melt inclusions. *American Mineralogist* **86**, 238–246.

Shi, P. (1993). Low-pressure phase relationships in the system Na_2O–CaO–FeO–MgO–Al_2O_3–SiO_2 at 1100°C, with implications for the differentiation of basaltic magmas. *Journal of Petrology* **34**, 743–762.

Soulard, H., Provost, A. & Boivin, P. (1992). CaO–MgO–Al_2O_3–SiO_2–Na_2O (CMASN) at 1 bar from low to high Na_2O contents: Topology of an analogue for alkaline basic rocks. *Chemical Geology* **96**, 459–477.

Sparks, R. S. J., Huppert, H. E., Kerr, R. C., McKenzie, D. P. & Tait, S. R. (1985). Postcumulus processes in layered intrusions. *Geological Magazine* **122**, 555–568.

Stewart, B. W. & DePaulo, D. J. (1990). Isotopic studies of processes of mafic magma chambers: II. The Skaergaard intrusion, East Greenland. *Contributions to Mineralogy and Petrology* **104**, 125–141.

Stormer, J. C. (1983). The effects of recalculation on estimates of temperature and oxygen fugacity from analyses of multicomponent iron titanium oxides. *American Mineralogist* **68**, 586–594.

Stripp, G., Holness, M. & Veklser, I. (2006). Enigmatic late-stage textures in mafic cumulates: Skaergaard Intrusion, East Greenland. *EOS Transactions of the American Geophysical Union* **87**(52), Fall Meeting Supplement, Abstract V51B-1672.

Sugawara, T. (2001). Ferric iron partitioning between plagioclase and silicate liquid: thermodynamics and petrological applications. *Contributions to Mineralogy and Petrology* **141**, 659–686.

Tait, S. & Jaupart, C. (1992). Compositional convection in a reactive crystalline mush and melt differentiation. *Journal of Geophysical Research* **97**, 6735–6756.

Taylor, H. P. & Forester, R. W. (1979). An oxygen and hydrogen isotope study of the Skaergaard intrusion and its country rocks: a description of a 55 M.Y. old fossil hydrothermal system. *Journal of Petrology* **20**, 355–419.

Tegner, C. (1997). Iron in plagioclase as a monitor of the differentiation of the Skaergaard intrusion. *Contributions to Mineralogy and Petrology* **128**, 45–51.

Tegner, C. & Cawthorn, R. G. (2010). Iron in plagioclase in the Bushveld and Skaergaard intrusions: implications for iron contents in evolving basic magmas. *Contributions to Mineralogy and Petrology* **159**, 719–730.

Tegner, C., Thy, P., Holness, M. B., Jakobsen, J. K. & Lesher, C. E. (2009). Differentiation and compaction in the Skaergaard intrusion. *Journal of Petrology* **50**, 813–840.

Tharp, T. M., Loucks, R. R. & Sack, R. O. (1998). Modeling compaction of olivine cumulates in the Muskox intrusion. *American Journal of Science* **298**, 758–790.

Thy, P., Lesher, C. E., Nielsen, T. F. D. & Brooks, C. K. (2006). Experimental constraints on the Skaergaard liquid line of descent. *Lithos* **92**, 154–180.

Thy, P., Lesher, C. E. & Tegner, C. (2009). The Skaergaard liquid line of descent revisited. *Contributions to Mineralogy and Petrology* **157**, 735–747.

Toplis, M. J. & Carroll, M. R. (1995). An experimental study of the influence of oxygen fugacity on Fe–Ti oxide stability, phase relations, and mineral–melt equilibria in ferro-basaltic systems. *Journal of Petrology* **36**, 1137–1170.

Toplis, M. J. & Carroll, M. R. (1996). Differentiation of ferro-basaltic magmas under conditions open and closed to oxygen: Implications for the Skaergaard Intrusion and other natural systems. *Journal of Petrology* **37**, 837–858.

Turner, S. P. & Stüwe, K. (1992). Low-pressure corona textures between olivine and plagioclase in un-metamorphosed gabbros from Black Hill, South Australia. *Mineralogical Magazine* **56**, 503–509.

Veksler, I. V. (2009). Extreme iron enrichment and liquid immiscibility in mafic intrusions: experimental evidence revisited. *Lithos* **111**, 72–82.

Veksler, I. V., Dorfman, A., Danyushevsky, L., Jakobsen, J. & Dingwell, D. (2006). Immiscible silicate liquid partition coefficients: Implications for crystal–melt element partitioning and basalt petrogenesis. *Contributions to Mineralogy and Petrology* **152**, 685–702.

Veksler, I. V., Dorfman, A., Borisov, A. A., Wirth, R. & Dingwell, D. (2007). Liquid immiscibility and the evolution of basaltic magma. *Journal of Petrology* **48**, 2187–2210.

Veksler, I. V., Dorfman, A., Borisov, A. A., Wirth, R. & Dingwell, D. (2008). Liquid immiscibility and evolution of basaltic magma: Reply to S. A. Morse, A. R. McBirney and A. R. Philpotts. *Journal of Petrology* **49**, 2177–2186.

Veksler, I. V., Kähn, J., Franz, G. & Dingwell, D. B. (2010). Interfacial tension between immiscible liquids in the system K_2O–FeO–Fe_2O_3–Al_2O_3–SiO_2 and implications for the kinetics of silicate melt unmixing. *American Mineralogist* **95**, 1679–1685.

Vincent, E. A. & Phillips, R. (1954). Iron–titanium oxide minerals in layered gabbros of the Skaergaard intrusion, East Greenland: Part I. Chemistry and ore-microscopy. *Geochimica et Cosmochimica Acta* **6**, 1–4.

Wager, L. R. & Brown, G. M. (1968). *Layered Igneous Rocks*. Edinburgh: Oliver & Boyd.

Wager, L. R. & Deer, W. A. (1939). Geological investigations in East Greenland. Pt III. The petrology of the Skaergaard intrusion. Kangerdlugssuaq, East Greenland. *Meddeleser om Grønland* **105**, 1–352.

Wager, L. R., Brown, G. M. & Wadsworth, W. J. (1960). Types of igneous cumulates. *Journal of Petrology* **1**, 73–85.

Watson, E. B. (1976). Two-liquid partition coefficients. Experimental data and geochemical implications. *Contributions to Mineralogy and Petrology* **56**, 119–134.

Watson, E. B. & Harrison, T. M. (2005). Zircon thermometer reveals minimum melt conditions on earliest Earth. *Science* **308**, 841–844.

Wilke, M. & Behrens, H. (1999). The dependence of the partitioning of iron and europium between plagioclase and hydrous tonalitic melt on oxygen fugacity. *Contributions to Mineralogy and Petrology* **137**, 102–114.